THESIS FOR THE DEGREE OF DOCTOR OF PHILOSOPHY

Non-Covalent Surface Engineering of 2D Black Phosphorus and MXene: Redox-Active and Multi-cationic Oxidation Stabilisers

A side-by-side analysis and evaluation of Viologen-based stabilisers for 2D materials, and the design of new functional systems

ISHAN SARKAR

Department of Chemistry and Chemical Engineering

CHALMERS UNIVERSITY OF TECHNOLOGY

Gothenburg, Sweden 2026

Non-Covalent Surface Engineering of Black Phosphorus and $Ti_3C_2T_x$ MXene: Redox-Active and Multi-cationic Oxidation Inhibitors
ISHAN SARKAR
ISBN **978-91-8103-511-7**

Acknowledgements, dedications, and similar personal statements in this thesis, reflect the author's own views.

© ISHAN SARKAR, 2026.

Doktorsavhandlingar vid Chalmers tekniska högskola
Ny serie nr **5968**
ISSN 0346-718X
https://doi.org/10.63959/chalmers.dt/5968

Department of Chemistry and Chemical Engineering
Chalmers University of Technology
SE-412 96 Gothenburg
Sweden
Telephone + 46 (0)31-772 1000

Cover:
Inspired by the metaphor of shelter in a storm, the cover depicts protective molecular coatings preserving two-dimensional materials against the persistent effects of environmental degradation.

Printed by Chalmers Digitaltryck
Gothenburg, Sweden 2026

Non-Covalent Surface Engineering of Black Phosphorus and $Ti_3C_2T_x$ MXene: Redox-Active and Multi-cationic Oxidation Inhibitors

Ishan Sarkar

Department of Chemistry and Chemical Engineering
Chalmers University of Technology

Abstract

Black phosphorus nanosheets (BPNSs) and $Ti_3C_2T_x$ MXene possess electronic and electrochemical properties of considerable technological interest, yet both oxidise readily under ambient conditions, which restricts their processing and use. Non-covalent functionalisation offers a route to suppress this degradation without disrupting the lattice, but most reports establish that a treated material degrades more slowly and leave underlying interactions unexplained. This thesis examines how the structure of a molecular modifier determines the mechanism and effectiveness of protection on each material.

A series of viologen-based molecules and oligomers was assessed on both materials using X-ray photoelectron spectroscopy, UV-Visible spectroscopy, vibrational spectroscopy and electron microscopy. Methyl viologen protected BPNSs, whereas an oligomer carrying the same viologen unit as a pendant group on an oligo-styrene backbone did not. The same oligomer, however, was effective on MXene. These results indicate that the same cationic group can perform differently depending on how it is presented, and that BPNS and MXene respond to different molecular features. Density functional theory calculations from our collaborators were used to rationalise these differences and to guide further designs. Significant protection was observed on both materials over 6 days period, though the molecular features associated with it differed, e.g., small, electron-accepting cationic molecules for BPNSs, and multivalent, cationic structures for MXene, suggesting distinct modes of interactions.

From these findings, design guidelines were derived for each material, and new systems were proposed: pyrene-4,5,9,10-tetraone-based acceptors, and metal-organic frameworks based on viologen-derived zwitterionic molecules (QINAgens), intended to retain protective function while supporting electrochemical energy storage applications. Experimental work on these systems is under way. The thesis concludes that ambient stabilisation is best approached by identifying the degradation pathway of each material before selecting the molecular design.

Keywords: Black phosphorus; $Ti_3C_2T_x$ MXene; non-covalent functionalisation; ambient stability; oxidative degradation; viologen; pyrene-4,5,9,10-tetraone; molecular design; metal-organic framework; energy storage

Acknowledgements

First and foremost, I would like to thank my supervisor, **Xiaoyan Zhang**, for his guidance, support, and trust throughout my doctoral studies. Your scientific insight, encouragement, and dedication have played a central role in shaping both this work and my development as a researcher. Thank you for continuously challenging me to think critically, for providing valuable perspective whenever difficulties arose, and for creating an environment in which I could grow independently while knowing that support was always available.

I am also deeply grateful to **Lars Öhrström** for stepping in as my supervisor during Xiaoyan's absence. Your guidance, support, and willingness to help at critical moments have been greatly appreciated. Thank you for ensuring continuity and for generously sharing your time, knowledge, and experience.

A special thank you goes to **Jerker Mårtensson**. Throughout these years, you have been the person I could always turn to whenever a scientific problem, practical obstacle, or unexpected challenge appeared. Countless discussions in your office, whether related to chemistry, research, or simply finding a different perspective on a problem, have been invaluable. Your ability to dissect complex issues and provide thoughtful advice has helped me more times than I can count.

I would also like to thank **Martin Rahm**, my co-supervisor, and **Maria Abrahamsson**, my examiner. Both of you have been incredibly supportive throughout my doctoral studies. Thank you for your guidance, encouragement, organisational support, and for always taking the time to discuss chemistry-related questions and uncertainties. Your willingness to share your expertise and provide reassurance during challenging periods has been greatly appreciated.

To the professors, colleagues, and friends on Floor 9, thank you for creating such a welcoming, supportive, and intellectually stimulating environment. Floor 9 has been my second home for the past four and a half years. The scientific discussions, spontaneous brainstorming sessions, coffee breaks, shared frustrations, celebrations, and moments of laughter have made this journey far more enjoyable than I could have imagined. Although it is impossible to mention everyone individually, I am sincerely grateful to all of you for your kindness, encouragement, and willingness to help whenever needed.

To my friends, thank you for the companionship, humour, and perspective that helped me navigate the highs and lows of doctoral studies. Whether through scientific discussions, shared meals, or simply providing a welcome distraction from research, your friendship has made these years far richer and more memorable.

To my parents, words cannot adequately express my gratitude. Thank you for your unconditional love, encouragement, and sacrifices throughout my life. From a young age, you supported every ambition, curiosity, and dream I pursued, no matter how unrealistic it may have seemed at the time. Your unwavering faith in me has been a constant source of confidence and strength, and I would not be where I am today without your support.

Most importantly, I would like to thank my partner. Throughout this PhD, you have been my greatest source of support, patience, and encouragement. Thank you for standing beside me through both the successes and the setbacks, for listening to countless conversations

about experiments, papers, and deadlines, and for reminding me to keep perspective whenever research became overwhelming. Your belief in me never wavered, even during moments when my own confidence did. This journey would have been immeasurably more difficult without your love and support, and I am deeply grateful to have shared it with you.

Finally, I would like to thank everyone who has contributed to this work and to my growth over the past four and a half years. This thesis may carry my name, but it reflects the support, knowledge, kindness, and encouragement of many people. To all of you, thank you for helping me reach this milestone.

List of publication

I. **Boosting 2D Black Phosphorus Ambient Stability: Noncovalent Functionalization using Viologen Molecules.** Ishan Sarkar, Cong Guo, Cheng Peng, Yu Wang, Yafei Li, Xiaoyan Zhang*, *Small*, **2026**, 22, 2410300.

II. **Viologen-Based Branched Oligomer Functionalization of Two-Dimensional Black Phosphorus: Interfacial Interactions and Ambient Stability.** Ishan Sarkar, Xiaoyan Zhang*, *Manuscript in preparation*.

III. **Engineering a Viologen-Based Branched Oligomer for Effective Ambient Stabilization of $Ti_3C_2T_x$ MXene.** Ishan Sarkar, Mangmang Shi, Xiaoyan Zhang*, *Manuscript in preparation* (*Close to submission)*.

IV. **A green synthesis strategy based on a neutral zwitterionic carboxylate linker giving a Zr_6 MOF with the elusive reo topology.** Ishan Sarkar†, William E. Reinholdsson†, Alek Parkin, Chandra K. Patlolla, Mangmang Shi, Ocean Cheung, Xiaoyan Zhang*, and Lars Öhrström*, *Submitted to IUCrJ*. (†Equal contribution)

V. **An Extended π-Conjugated Cationic Pyrene-4,5,9,10-Tetraone Derivative with Enhanced Redox Behaviour through Molecular Engineering.** Ishan Sarkar, Xiaoyan Zhang*, *Manuscript in Preparation.*

Contribution Report

Paper I: Principal contributor to the study, responsible for the synthesis, purification, and characterisation of the molecular systems; preparation of black phosphorus nanosheets; development of hybrid formation strategies; characterisation of the resulting hybrids; data analysis; and manuscript preparation. Collaborators performed XPS measurements and DFT calculations.

Paper II: Principal contributor to the study, responsible for the synthesis, purification, and characterisation of the molecular and oligomeric systems; preparation of black phosphorus nanosheets; development of hybrid formation strategies; characterisation of the resulting hybrids; data analysis; and manuscript preparation.

Paper III: Principal contributor to the study, responsible for the synthesis, purification, and characterisation of the molecular and oligomeric systems; preparation of $Ti_3C_2T_x$ MXene nanosheets; development of hybrid formation strategies; all characterisation of the resulting hybrids; data analysis; and manuscript preparation. Collaborators carried out the theoretical calculations and the first set of XPS experiments.

Paper IV: Made substantial contributions to the design, synthesis, purification and characterisation of the linker system used for MOF construction. Conducted characterisation of both the linker and framework materials, including XPS and SEM analyses, participated in data interpretation, and contributed to manuscript preparation. The work was carried out in close collaboration with co-authors responsible for framework synthesis and crystallographic characterisations.

Paper V: Designed and synthesised the molecular systems investigated in the study, including their purification, structural characterization and manuscript drafting.

Table of Contents

1. Introduction 1
   1.1 Graphene and 2D materials 1
   1.2 Black phosphorus (BP) 2
   1.3 MXenes 3
   1.4 Non-covalent functionalisation 5
   1.5 Synthesis and characterisation techniques 6
   1.6 Scope of the thesis 6
2. Functionalisation of Black Phosphorus for Improved Ambient Stability 9
   2.1 The problem 9
   2.2 Working hypothesis and molecular designs 10
   2.3 Results and discussions 13
      2.3.1 Physicochemical interaction studies 13
      2.3.2 Characterisation studies for the composite systems 16
      2.3.3 Morphological studies for the composite systems 18
      2.3.4 Ambient stability studies for the composite systems 21
   2.4 Understanding the results 25
   2.5 DFT insights 26
   2.6 Beyond the initial set 29
3. Functionalisation of MXenes for Improved Ambient Stability 31
   3.1 The problem 31
   3.2 Working hypothesis and introduction to our MXenes 31
   3.3 Results and discussions 33
      3.3.1 Physicochemical studies 33
      3.3.2 Morphological studies of the composites 34
      3.3.3 Characterisation of the Composites 38
      3.3.4 Ambient stability studies of the composites 41
   3.4 Understanding the results 45
   3.5 DFT insights 46
   3.6 Coalescing behaviour of the oligomer-15 48
4. Mechanism of the Interactions 51
   4.1 Types of interactions 51
   4.2 What controls binding 51
   4.3 BPNSs vs MXenes 52
   4.4 General trends 53
5. From Protection to Practical Function through Molecular Design 55
   5.1 Key takeaways 55
   5.2 Design guidelines 55
   5.3 Designing molecular systems for energy-storage application 56
      5.3.1 Pyrene-4,5,9,10-tetrone based molecular systems 57
      5.3.2 QINAgen-based framework systems (QDINA-linker) 63
6. Summary and Outlook 67
   6.1 Conclusion 67
   6.2 Future work 67

Bibliography 69

Appendix: Experimental Section 73

Abbreviations

2D – Two-dimensional
ATR-FTIR – Attenuated Total Reflectance Fourier Transform Infrared Spectroscopy
BP – Black Phosphorus
BPNS – Black Phosphorus Nanosheet
BPNSs – Black Phosphorus Nanosheets
DFT – Density Functional Theory
FFT – Fast Fourier Transform
FET – Field Effect Transistor
FTIR – Fourier Transform Infrared Spectroscopy
GGA – Generalised Gradient Approximation
GPC – Gel Permeation Chromatography
HF – Hydrofluoric Acid
HOMO – Highest Occupied Molecular Orbital
HR-TEM – High-Resolution Transmission Electron Microscopy
IMRAD – Introduction, Methods, Results and Discussion
LUMO – Lowest Unoccupied Molecular Orbital
MAX – Layered transition-metal carbide/nitride precursor phase (M = transition metal, A = A-group element, X = carbon and/or nitrogen)
MOF – Metal-Organic Framework
MXene – Two-dimensional transition-metal carbide/nitride material derived from MAX phases
PAW – Projector Augmented Wave
PBE – Perdew-Burke-Ernzerhof functional
PDI – Polydispersity Index
QDINA – Quaternary Di-Isonicotinic Acid
QINAgen – Quaternary Iso-Nicotinic Acid-based linker system
SEM – Scanning Electron Microscopy
SP – Surface Plasmon
STM – Scanning Tunnelling Microscopy
TEM – Transmission Electron Microscopy
TFA – Trifluoroacetic Acid
TMD – Transition Metal Dichalcogenide
UV-Vis – Ultraviolet-Visible Spectroscopy
VASP – Vienna Ab Initio Simulation Package
XPS – X-ray Photoelectron Spectroscopy
D-A – Donor-Acceptor
Fe-HCF – Iron Hexacyanoferrate
M_n, M_w, M_z – Polymer molecular weight descriptors
PyT – Pyrene-4,5,9,10-tetraone
TLC – Thin Layer Chromatography
PTLC – Preparative Thin Layer Chromatography
NMR – Nuclear Magnetic Resonance
SEC – Size Exclusion Chromatography

1. Introduction

Materials science has traditionally centred on bulk materials, where atoms arranged in three dimensions act together to produce a material's properties. This focus led to major breakthroughs, from structural engineering to microelectronics. But bulk systems allow only limited control at the atomic level, where new and surprising behaviours often appear. As researchers sought greater efficiency, precision, and tunability, they began turning to lower-dimensional systems. Then the question becomes, how far can we push the idea and achieve atomic level properties with bulk scalability? A concept had existed long back in ancient Greek[1] and Hindu[2] philosophy about atom which comes from dividing material repeatedly to arrive at a certain point where it'll no longer be divisible anymore. In 2004, Geim and Novoselov from the University of Manchester used very sophisticated tool – called scotch tape,[3] to peel apart a piece of graphite with the intension of keeping on peeling from the same tape over and over again as a so-called Friday evening experiment.[4] This resulted in them reaching a point where the material had quite long length and width (around 10 µm scale), but the thickness was of only one atom (0.34 nm). This material was later called graphene and the high aspect ratio (length/thickness: 3×10^5 for the previous example) is now considered to be one of the defining characteristics of 2D materials.[5]

1.1 Graphene and 2D materials

Even though the graphene originates from its 3D precursor graphite, the properties of it vastly diverge from that of the graphite. Graphene was found to be a stable, atomically thin (**Figure 1.1**), zero band-gap semimetal that allowed an unusually strong electric-field response and very high carrier mobility at room temperature.[3, 6] That single discovery opened an entire research area built around one simple question: what happens to a material's properties when you strip it down to a single atomic layer?

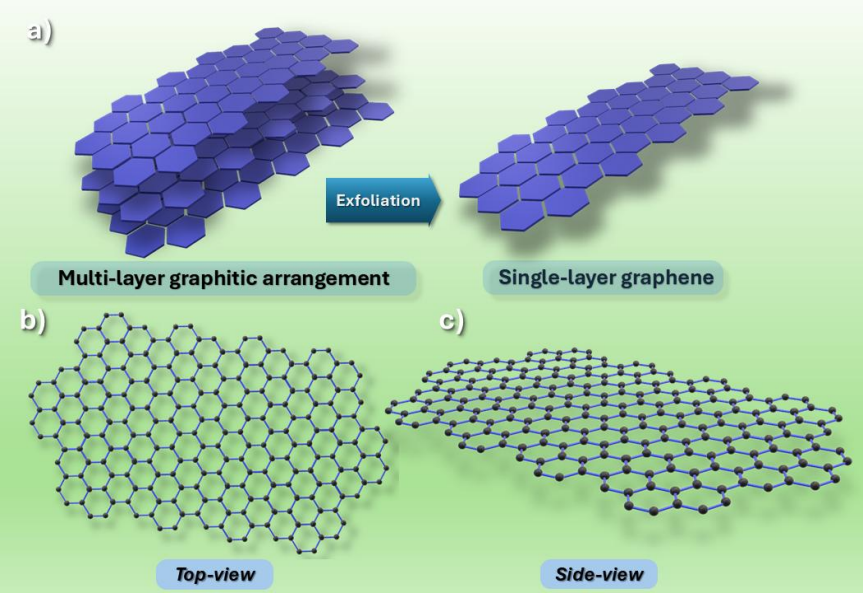

Figure 1.1 *Visual representation of (a) multi-layer graphitic arrangement (precursor) and single-layer graphene, (b) graphene showing its hexagonal array of sp^2 carbon atoms on its top view and (c) on its side view.*

When one of the dimensions of the material is reduced to the atomic layers, every atom becomes a part of the two surfaces just like in case of graphene. This dictates how electrons move in the material, how it reacts with light, and how chemically reactive the material is. Graphene turned out to have a major limitation for electronics especially in semiconductor industry as having no band gap makes transistors made from it unable to be switched off completely. Researchers had already been working on properties of different layered materials, e.g., the single layer of

MoS_2 was exfoliated in 1986,[7] but the theoretical studies predicting genuine bandgap came even before in 1973.[8] What is even more baffling is that MoS_2 was known human race since ancient civilisations.[9] When transistors were made from MoS_2, they showed high on/off switching ratios, something that graphene never managed to offer.[10] The exfoliation of graphene by as simple as a scotch-tape[3] meant that there probably exists more ways to a broad library of layered materials, barely explored due to complicated exfoliation methods, with various different elements, wide-ranging structures, tuneable according to needs with diverse electronic, optical and chemical properties. Black phosphorus and MXenes, the two materials covered in this work, are both members of that broader set.

1.2 Black phosphorus (BP)

Even though the research on the two-dimensional (2D) materials is a 21st century phenomenon, the discovery of black phosphorus dates back to 1914 when Bridgman obtained this peculiar allotrope of phosphorus. He prepared this specific form of phosphorus from already wide known white phosphorus at a pressure of 1.2 GPa and a temperature as high as 200 °C.[11] The report says:

> *"The second modification, black phosphorus, is obtained irreversibly from white phosphorus at 12,000 kg. and 200°. A number of its physical constants have been determined; particularly striking are its high density, 2.691, and fair electrical conductivity."*

In the later part of the 20th century, silicon as a bulk material took over the technological advancement due to its semiconducting properties. This overshadowed every other material and black phosphorus as a bulk material failed to gain research interest and as a result was forgotten.[12] However in the 80s, BP was described to have layered structure that could be peeled off as thin mica-like sheets,[13] was characterised both theoretically[14, 15] and empirically[13] and it was already known to be semiconducting. This led to delamination of the bulk black phosphorus in the 2D material era, and several studies were conducted consequently revealing its band structures in more details,[16] defects,[17] intercalation,[18] layer dependencies, characterisation methods[19, 20] and applications in energy storage, opto-electronics,[16, 21-26] sensing[27] etc.

When BP is reduced down to a monolayer or few layers, it gets its own name: phosphorene, a direct analogy to graphene. The bulk phosphorus has been studied both theoretically and practically for its lattice and electronic structures. Back in early 80s, in the calculations performed by Hideo Asahina et al. BP was recognised as having puckered layers (very similar to chair form of cyclohexane, **Figure 1.2**) packed in an orthorhombic lattice and each phosphorus atom in the monolayer was found to be bonded covalently to 3 other phosphorus atoms with almost identical bonds, one of which is 2.224 Å and the other two being 2.244 Å.[14, 15] Asahina et al. went on further to calculate the electronic structures of BP and they reported

> *"We find that the minimum gap is **direct** and appears at the point Z, namely at the Brillouin zone edge in the (001) direction… The energy gap depends on the parameter α of the exchange-correlation potential. In the present calculation, we used α = 0.8 so that the energy gap is equal to **0.3** eV."*[14]

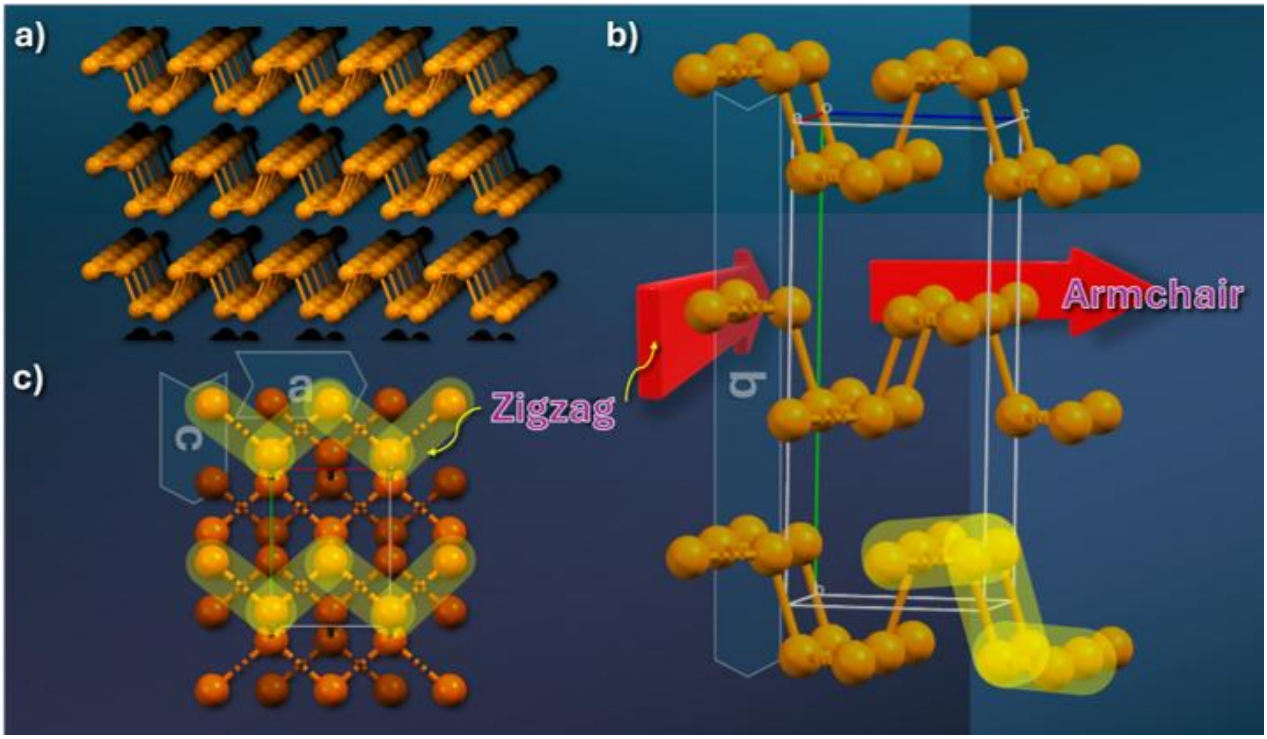

Figure 1.2 *BPNS crystal structure showing (a) 2D nanosheets stacked in bulk BP and the illustration of the zigzag and armchair directions in the crystal lattice from the side view (b) and the top view (c, the ridges are propagating towards the 'a' direction).*[28]

The optical absorption of ~0.33 eV and the semiconducting behaviour in both bulk and in 2D layer was reported even further back in 1953[29] and was confirmed by other studies.[30] Most likely because of technological inadequacy at that time it's 2D aspect failed to gain technological interest, but picked up pace during 2014 with a plethora of articles during that period. Xia et al.[31] reported absorption peaks at 2700 cm^{-1}, Liang et al.[32] reported the direct band gap to become 2.05 eV in single layers through scanning tunnelling microscopic (STM) characterisation techniques. These reports established phosphorenes or BP nanosheets (BPNSs, as we are going to call it) as significantly lower band-gap semiconductor falling in between zero band gap graphene[6] and the larger bandgap transition metal dichalcogenides (TMDs e.g., MoS_2, $MoSe_2$, $MoTe_2$, WS_2, WSe_2 etc.) (1.5 – 2.5 eV) enabling strong wave-matter interactions in mid-infrared, near-infrared and visible-frequency regions.[33, 34]

Despite these interesting properties and the wide range of potential applications, the practical use of BPNSs has remained limited. The main reason is that BPNSs is unstable under ambient conditions and degrades quickly when exposed to oxygen, water and light, which causes its properties to deteriorate. This instability is the biggest obstacle to the real-world use of BPNSs and will be discussed in detail in Chapter 2.

1.3 MXenes

MXenes are a much younger addition to the 2D materials family, firstly reported in 2011 by researcher from Drexel University.[35] Their approach towards achieving 2D sheet was more scalable compared to the scotch tape-peeling method. They started with a layered ceramic with a general composition of Ti_3AlC_2, commonly known as the MAX phase (M = metal, A =

Aluminium, X = skeletal non-metal e.g. C, N), and selectively etched out the aluminium layer using hydrofluoric acid as the Al—F and Ti—F bonds have very high bond dissociation energies, hence, are very stable, especially more than Ti—Al—Ti bonds.[36] This etching method allowed researchers to have a whole range of nanosheets having a thickness of few atoms ($Ti_3C_2T_x$ in the first reported case, T = Surface terminations e.g. —F, —OH, **Figure 1.3**) termed MXenes (M = metal, X = skeletal non-metal e.g. C, N) with scalable exfoliation suitable for potential applications.[37]

MXenes are also reported to be metallic as it doesn't have any bandgap, and its free electrons carry charge in a way very similar to conventional metals. Halim et al. fabricated thin Ti_3C_2 films and traced their change in resistivity with varying temperature, and found that the conductivity of those films was metallic in nature and sustains until as low as 100 K.[38] Theoretical calculations has been studied extensively across a wide range of MXene materials, and it is well established now that the metallic behaviour is primarily driven by metal-d electrons (3d for Sc, V, Ti, etc.),[39-44] the same partially filled orbitals responsible for the characteristic conductivity of transition-metal ceramics. It was also shown that the conduction is highly anisotropic, i.e., the electrons move through the basal plane more easily than along the 2D plane, due to the strong in-plane M—C (M = Sc, V, Ti, etc.) bonds facilitating fast electron transport and weak interlayer coupling.

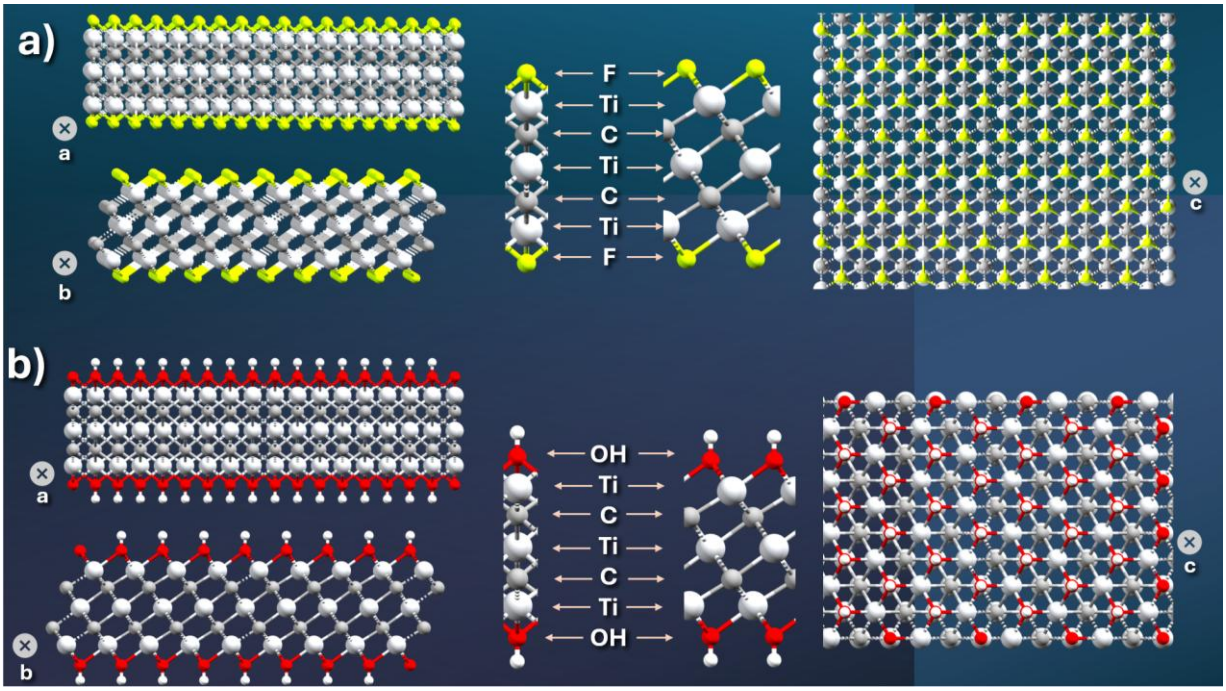

Figure 1.3 *MXene crystal structure showing (a) $Ti_3C_2F_2$ MXene shown from different crystal axes with the alignment of different atoms in the cross-section of the sheet and the same for (b) $Ti_3C_2(OH)_2$ MXene.*[45]

The unusually high density of free charge carriers, unlike most other 2D materials opens an entirely new door: plasmonics. The first direct evidence of intense surface plasmon excitations were detected at energies as low as mid-infrared region and the tunability can be achieved by the adjusting the functional groups.[46] This behaviour was found to be thickness dependent[47] and after a temperature of 500 °C desorption of the F-atoms multiplies the metal-like free electron density of $Ti_3C_2T_x$ flakes, resulting in a monotonic blue-shift in the SP energy of all modes.[48]

All these properties make MXene very useful as functional components in electronics[39-44, 49-52], catalysis[53, 54] and energy storage.[55-58] However, their practical use is also limited by poor stability under ambient and aqueous conditions, where oxidation leads to loss of conductivity and other useful properties (more on chapter 3). In addition, the mixed, synthesis-dependent surface terminations cause variable properties and device performance, making controlled surface modification essential for reliable applications. This has driven growing interest in functionalisation strategies that can both protect and tune the MXene surface.

1.4 Non-covalent functionalisation

Non-covalent functionalisation is the modification of a material's surface by molecules that are held in place by intermolecular forces rather than by new chemical bonds. The forces involved include van der Waals interactions, hydrogen bonding, electrostatic attraction, charge-transfer (donor-acceptor) interactions, and cation-π and lone pair-π interactions. Which of these dominates depends on the surface chemistry of the host material and on the structure of the adsorbed molecule. π-π interaction is mainly relevant between adsorbed aromatic molecules, where it can drive ordered assembly on the surface. In all cases, the host lattice remains largely intact.

Hydrophobic interactions are commonly misjudged as a kind of van der Waals force and occur between water and substances which have very low polarity and low water-solubility. Its thermodynamic basis is commonly expressed through the Gibbs free energy,

$$\Delta G = \Delta H - T\Delta S$$

where aggregation becomes favourable when $\Delta G < 0$. The reduction in hydrophobe-water interfacial area upon association leads to a favourable increase in solvent entropy ($\Delta S > 0$), causing the $-T\Delta S$ contribution to lower the overall free energy of the system. As a result, hydrophobic association is generally considered to be driven primarily by entropic gains within the solvent.

The main reason to prefer non-covalent over covalent methods is that the intrinsic properties of the material could be largely preserved. The electronic and electrochemical behaviour of 2D materials depends on the integrity of the lattice. Covalent modification changes local bonding, can introduce defects, and can disturb charge transport.[59] This is a serious drawback when the goal is to improve ambient stability without losing the properties that make the material useful. Non-covalent coatings can shield reactive sites and limit access of water and oxygen while leaving the lattice unchanged. They also use mild conditions, usually near room temperature, and are often reversible, so the coating can be adjusted or potentially be removed.

These same features make non-covalent interactions difficult to control. Each interaction is weak, typically in the range of 1 to 50 kJ mol^{-1}, whereas covalent bonds are typically 150 to 500 kJ mol^{-1}. Strongly charge-assisted interactions can be stronger, but they are still generally weaker than covalent bonds. The interactions also depend on the environment, since solvent, pH, ionic strength, and temperature can all shift the binding equilibrium. They are often transient, because molecules continuously adsorb and desorb. Stable protection therefore depends on many weak interactions acting together, and on molecular design that makes binding strong and selective enough to last under ambient conditions.

1.5 Synthesis and characterisation techniques

Designing a non-covalent functionalisation system is not so straightforward, and the outcome is hard to predict. The molecular structure directly controls the strength, selectivity, and orientation of binding on the surface. The size of the conjugated core, the type and position of anchoring groups, and the length and flexibility of side chains determine whether a molecule lies flat, tilts, or forms an ordered layer. Small changes in molecular structure or synthesis conditions can therefore cause large changes in surface coverage, packing, stability, and performance. In these systems, the interaction itself is what is being designed. It is not enough to show that a treated material is more stable or performs better, the interaction between the individual components must also be shown to exist and be characterised.

This is difficult because non-covalent interactions cannot be observed easily.[60] Their spectroscopic signatures are usually subtle, appearing as small peak shifts, intensity changes, or broadening rather than new distinct features. Characterisation therefore relies on several techniques, each giving indirect evidence, which must be combined into one consistent picture. X-ray photoelectron spectroscopy (XPS) probes surface chemistry. It shows changes in elemental composition with additional information on possible oxidation states of each element, and binding-energy shifts that can indicate charge transfer. It also identifies oxidised species, such as P–O bonds in BP, which appear at higher binding energy than the P–P doublet, or Ti–O bonds in $Ti_3C_2T_x$. Raman spectroscopy reports on structural changes. For BP, changes in the three characteristic modes (A^1_g, B_{2g}, A^2_g) can reflect strain, doping, or degradation. For $Ti_3C_2T_x$, the appearance of anatase TiO_2 modes signals oxidation. Scanning and transmission electron microscopy (SEM/TEM) show morphology, including flake integrity, the uniformity of molecular coatings, and the formation of oxide particles. Electrochemical measurements link these observations to functional outcomes, such as capacitance, charge-transfer resistance, and retention of performance over time. No single technique can prove that a non-covalent interaction causes improved stability, so the evidence is convincing only when the results from several techniques match.

1.6 Scope of the thesis

Many studies report improved ambient stability or performance of functionalised 2D materials but do not explain why. Often, they only show that a treated sample degrades more slowly, without identifying the interaction involved, the binding mode of the molecule, or how its structure provides protection. This leaves a lack of systematic understanding, and design principles are hard to transfer from one molecule or material to another.

Closing this gap requires a clear link between molecular design, interaction mechanism, and material behaviour. This thesis explores that link by combining controlled variation of molecular structure with spectroscopic characterisations, microscopic characterisations, and theoretical calculations. The aim is to establish how specific molecular features determine the nature of surface interactions, and how that interaction governs stability and performance. In this way, the work moves from empirical reports of improvement toward a mechanistic basis for the rational design of non-covalent functionalisation.

The scope of this thesis is broad, as the work on BPNSs, the work on MXene and the design of new redox-active molecules are very distinct. Each of them has their separate research questions and cannot be brought under a single research question. For this reason, the

conventional IMRAD structure (Introduction, Methods, Results and Discussion), which is built around one question and one hypothesis, was not followed. Separating methods, results and discussion into different sections would have detached each result from the method behind it, so each chapter presents its own methods, results and discussions. We dedicate chapters 2 and 3 to the works on BPNSs and MXene, respectively. Afterwards, Chapter 4 discusses the general trends within the two 2D materials discussed before and chapter 5 proposes the newer designs for protection and practical functions, followed by summary and outlook in chapter 6.

2. Functionalisation of Black Phosphorus for Improved Ambient Stability

2.1 The problem

The main problem that has been in the way of the applicability for BPNSs (despite BP being comparatively more thermodynamically stable allotrope of phosphorus[61]) has been its innate ability to react with ambient oxygen since phosphorus—oxygen bond is strong with a large bond dissociation energy (ΔHf_{298} = 596.6 kJ/mol).[62] Ample studies have been conducted on theoretical grounds backed up by empirical evidence to figure out the steps involved for the degradation alongside the parameters necessary. On an attempt to report the complete characterisation of few-layer flakes, Castellanos-Gomes et al.[19] documented *"Aging of black phosphorus flakes"*, where they discuss condensation and adsorption of moisture onto the aged flakes, well characterised by optical microscopy, Raman spectroscopy and DFT calculation.

While water was being the prime suspect for this "aging process", reports have been published by Ziletti et al.,[63] where they accused oxygen to be the main culprit (**Figure 2.1**). According to the theoretical calculations performed by them, the average binding energy of triplet oxygen was found to be negative, or in other words, chemisorption of oxygen onto phosphorene was inherently exothermic (energetically favoured). They also mentioned that in the perturbed band picture of the oxidised phosphorene, valence band included p_z orbitals of oxygen and *p* orbitals of phosphorus atoms, whereas the acceptor state consisted of p_x and p_y orbitals of oxygen and *p* orbitals from phosphorus atoms most likely due to formation of the oxygen bridges between two phosphorus atoms (both diagonal and horizontal). Moreover, the oxidation results in long P—P bonds, inflating layer thickness by 36% which not only promoted further propagation in the neighbouring defect sites but also broke the crystal apart by employing larger stress in presence of high interstitial oxygen concentration, resulting in high molecular phosphorus oxides (later identified experimentally to be P_2O_5 by Edmonds et al.[64]).

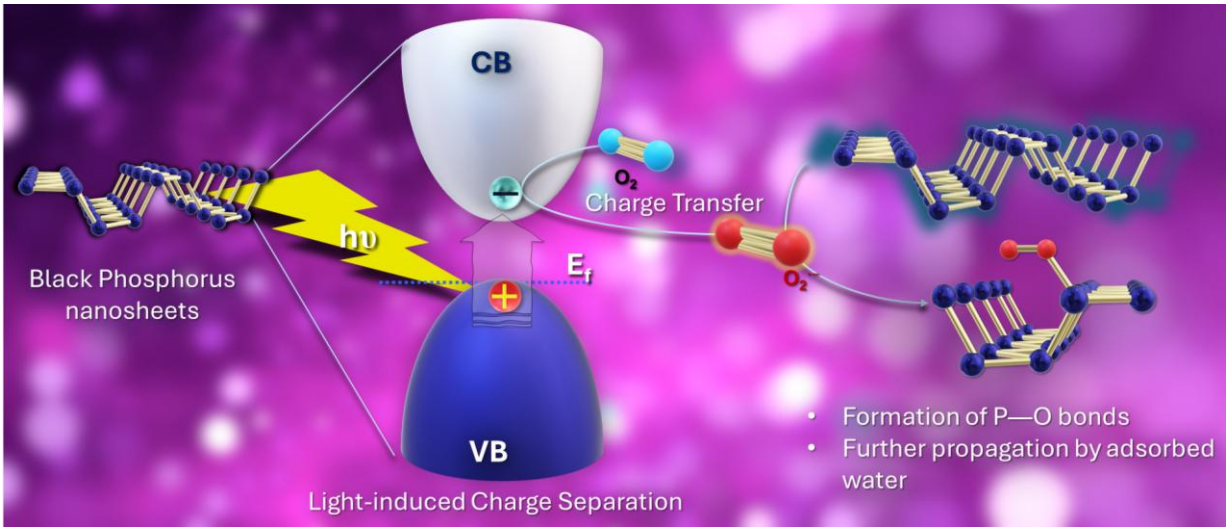

Figure 2.1 *Schematic representation of the aging process of BPNSs.*

Further measurements on FET devices (backed up by DFT calculations) from Huang et al.[65] indicated that water caused only minor changes to the device performance since it physisorbed onto the pristine multi-layered BPNS and didn't form covalent bonds by itself. However, the dissociative adsorption of oxygen perturbed the band environment, altering the charge transport properties.

By 2016, researchers have settled on the fact that oxygen was the initiator, and physisorbed water is the propagator in the aging process along with all the possible intermediates. They had found why and how, but one question remained: "What causes it?"

Ab initio calculations and molecular dynamics simulations by Zhou et al.[66] provided with more insights to the question. They proposed that the degradation occurred in 3 distinct and important steps: firstly, oxygen radicle anion ($O_2^{\bullet-}$) generation through charge transfer from BPNSs to O_2 (**Figure 2.1**), followed by dissociation of the molecular anion of oxygen onto the nanosheet surface forming P–O bonds (dangling O–P=O and P–O–P bridges) and finally rupturing of the top layer by hydrogen-bonded water molecules. Later, Abellán et al.[67] showed empirically that the stability of BPNSs is not only solvent dependent, but depends also relies on the thickness of the nanosheets and the presence of light.

Altogether, three factors which were particularly important for the oxidation of few-layered BP were the presence of light, oxygen and adsorption of water. However, the bulk BP was inherently immune to the aging process since the inner layers were protected by the coatings of the oxidised phosphorus from the top layer.

2.2 Working hypothesis and molecular designs

Since the BPNSs are composed of phosphorus atoms and they have lone pairs, the nanosheet surface should be electron dense. Also, the end groups and surface groups should be different kinds of phosphate groups generated throughout the preparation steps, which makes the overall nanosheet slightly negatively charged. Hence, we postulated that BPNSs can be functionalised non-covalently with organic molecules if the molecules were electron deficient, either caused by functional groups or by cationic charges mainly dissipated onto a π-conjugated system (**Scheme 2.1**). Furthermore, we hypothesised that the introduction of hydrophobic groups or backbones (**15**, **Scheme 2.1**) as well as higher electron deficiency of the molecular systems could inhibit interaction of oxygen with the nanosheet as well as decrease both physisorption and chemisorption of water onto the flake surface.

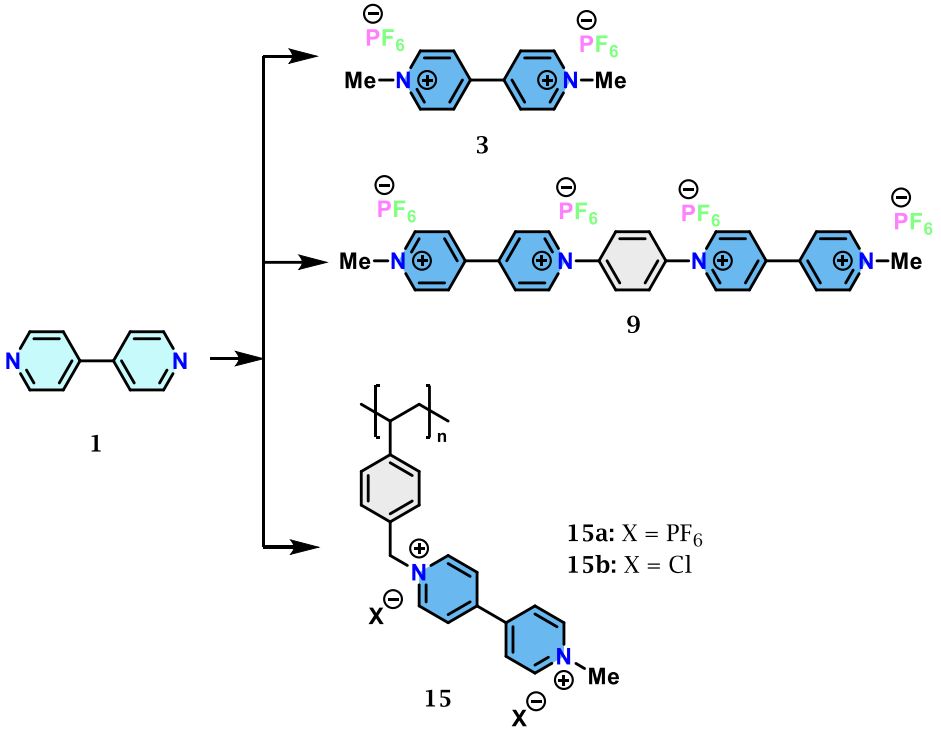

Scheme 2.1 *Design of the viologen derivative with 4,4'-bipyridine (**1**) as the precursor molecule.*

The initial designs were based on nitrogen-containing compounds as nitrogen can carry stable positive charges on in both sp^2 and sp^3 hybridised configuration and is comparatively easier to create positive charges unlike most other non-metals. Initially, considerable interests were directed towards the designs where the charge created could exist delocalised over a π-conjugated system, for which viologens were excellent choice.

The main purpose of this chapter is to discuss ways to functionalise BPNSs non-covalently to minimise oxidation. Since water rapidly helps in propagation, excluding water became pivotal in the design of all the experiments. For the lion's share of this chapter including the exfoliation of the nanosheets, dry acetonitrile was explored as a solvent system. Commercially available methyl viologen (N,N'-dimethyl-4,4'-bipyridinium chloride) with 2 cationic charges was explored initially and its counter ions were changed to hexafluorophosphate (**Scheme 2.1**, compound **3**) to render them soluble in low-polarity solvents e.g., dry acetonitrile, acetone. But would it be enough? Would a greater number of positive charges, dispersed over longer π-system and hydrophobicity help even more in improving protection efficiency?

To have answers to those questions, few more viologen derivatives were designed. One molecule was with 4 cationic charges delocalised over 5 rings (**Scheme 2.2**, compound **9**) and the other one was an oligomer (**Scheme 2.3**, oligomer **15**) with an oligo-styrene backbone and bipyridinium motifs as pendant groups.

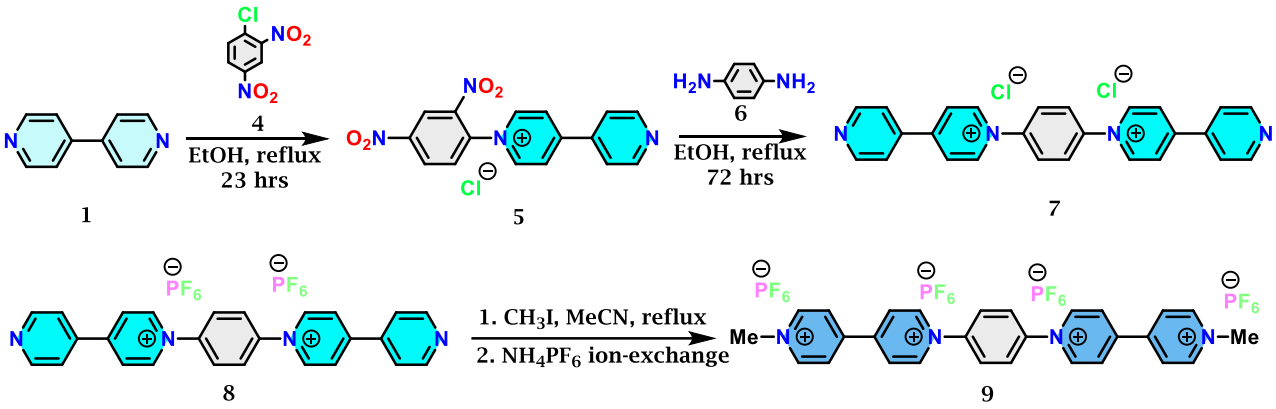

Scheme 2.2 *Synthetic route for compound* ***9****: Preparation of the Zincke salt (compound* ***1*** *→* ***5****), followed by Zincke reaction (compound* ***5*** *→* ***7****) followed by methylation (compound* ***8*** *→* ***9****). Compound* ***8*** *was transformed from* ***7*** *by ion-exchange for purification purpose.*

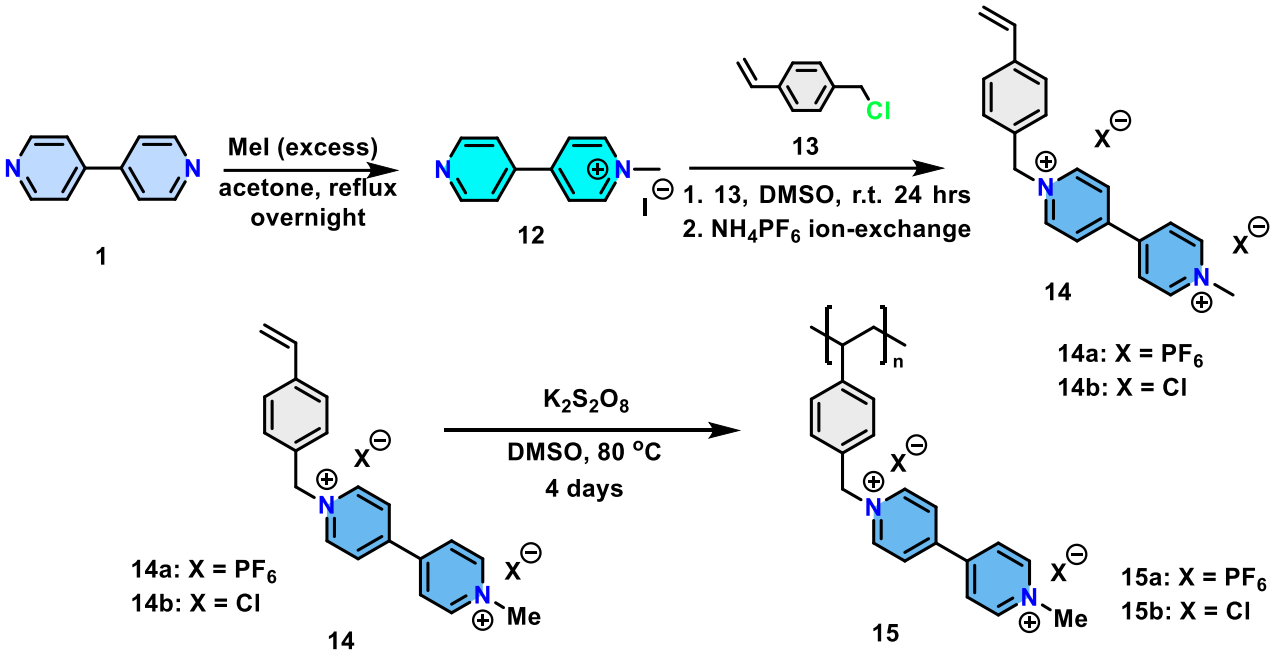

Scheme 2.3 *Synthetic pathway for the viologen-based oligomer* ***15*** *with an oligo-styrene backbone. (For the conversion of* ***1*** *to* ***12****, more than 1 equivalent of methyl iodide has been used, however, due to the extremely low solubility of* ***12*** *in acetone, the mono-substituted substituted product precipitates automatically and the reaction is terminated before further substitution).*

Both the compound **9** (**Scheme 2.2**) and oligomer **15** (**Scheme 2.3**) were synthesised from 4,4'-bipyridine. Zincke reaction[68] was employed to synthesise compound **9**. The Zincke salt was prepared from 2,4-dinitrochlorobenze (**4**) and later reacted it with *p*-phenylenediamine (**6**) under reflux conditions in ethanol. The reaction usually takes long time (3-4 days) with moderate yields compared to usual small molecule syntheses since the intermediates formed in this reaction involves ring opening (the charged ring in the Zincke salt) and re-cyclization of the ring. The ring closing on itself is entropically favourable. High dilution usually helps the most but comes at the cost of longer reaction times (approx. 3-5 days).

To facilitate subsequent evaluation of the experimental results, the use of the same solvent throughout was established to run our experiments and controls under nearly identical conditions. The cases where inhomogeneity issues dominated, mechanical grinding was employed to ensure that the composite samples were homogeneous. We are going to look at side-by-side comparisons in details in further discussions in this chapter.

2.3 Results and discussions

As we have seen already in chapter 1 before, the inter layer interaction in BP is very weak and could be broken by supplying mechanical energy. Our method for preparing BPNSs starts with grinding the bulk-BP crystals to get smaller particles followed by sonication in dry acetonitrile. The supernatant, thus generated, contains few layer BPNSs. Acetonitrile is chemically stable, aprotic, low boiling (hence easy to remove), has low toxicity and provides good exfoliation. Therefore, we also designed the composite formation strategies and characterisation methods to be performed in acetonitrile. For this reason, the chlorides or the mixed counterions were exchanged for hexafluorophosphate as they were very soluble in acetonitrile but not at all in water. Only exceptions were the Zeta-potential studies where we used the chloride derivatives and performed the study in degassed water medium. The choice was motivated by ability of acetonitrile to dissolve the cell wall and additionally the oligomer-**15a** being insoluble in acetonitrile.

The following discussion begins with the physicochemical studies exploring the interaction behaviours. Afterwards, the characterisations of the composites are discussed along with their morphologies and their ambient protection efficiency. Then the theoretical calculations from *our collaborators* were discussed and finally we end on molecular designs beyond our initial set.

2.3.1 Physicochemical interaction studies

The absorption spectra of compounds **3**, **9** (in acetonitrile) and oligomer-**15b** (in water) were measured and the λ_{max} for each of them appeared at 257 nm, 287 nm and 258 nm respectively. For compound **3** (**Figure 2.2**) and **15b** (**Figure 2.3**), the absorption consisted of only one peak, whereas compound **9** had one strong peak along with two very weak shoulder peaks (~250 nm and ~400 nm).

Upon addition of the compounds **3** and **9** to a fixed amount of BPNS dispersion in acetonitrile, red shift in molecular absorptions were observed. New λ_{max} for these two mixtures were found to be at 259 nm and 291 nm (**Figure 2.2**). For the oligomer-**15b**, no significant shifts in the peak absorbance were observed, however, something very interesting came up around the typical absorption of BPNS at ~500 nm. The absorption of the BPNS dispersion was observed to be decreasing upon addition of the oligomer, and around a mass fraction of 0.056, the decrease was noticed to converge (**Figure 2.3a**). Similar trend was also seen for the titrimetric studies with compound **3**, where the nanosheet absorption is seen to converge along with a permanent bathochromic shift in the peak absorbance after a mass fraction of 0.038 (10 µg of compound **3**) was reached. Interestingly, just 1 µg addition of the compound **9** was sufficient to converge the BPNS absorption and further addition didn't result any such hypochromic changes. Among all the three cases, compound **3** and oligomer **15** (both **15b** and **15a** derivatives; the latter was performed in acetonitrile but resulted in unpredictable aggregates) showed fast precipitation but for the compound **9**, there was no precipitation whatsoever.

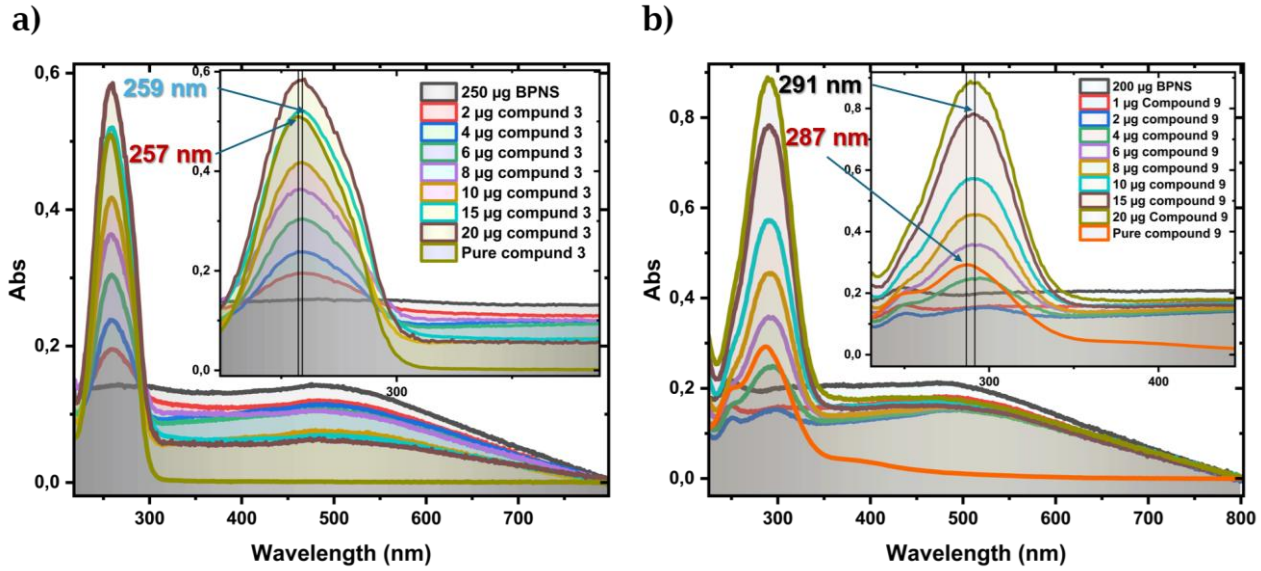

Figure 2.2 *Titrimetric studies indicate the interaction with BPNSs and (a) compound **3** and (b) compound **9** as observed through UV-Vis absorption measurements. In case of compound **3**, we observed significant lowering of the scattering compared to compound **9**.*

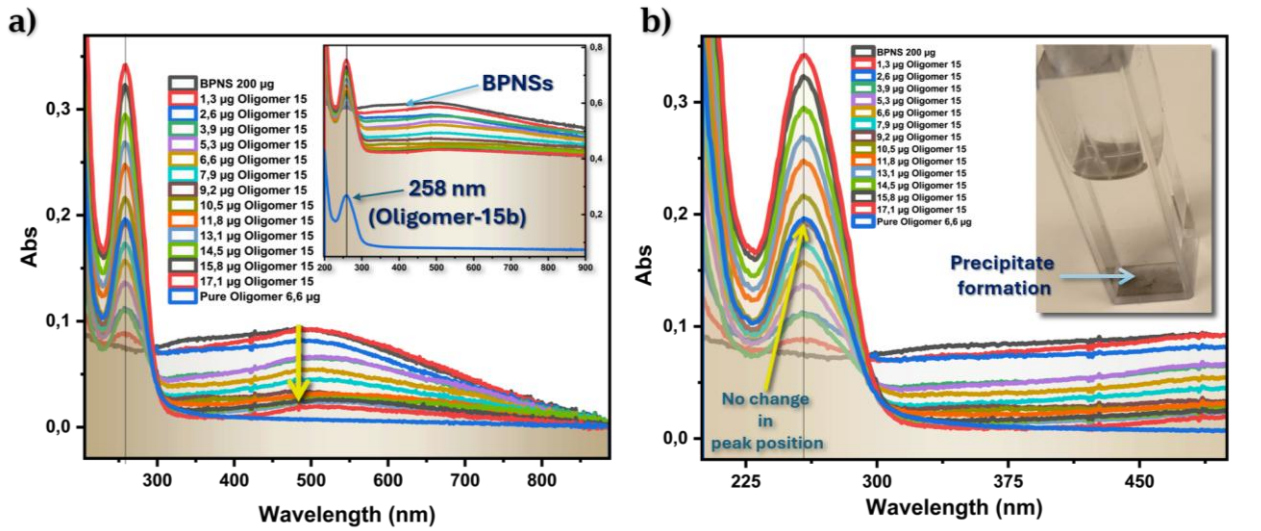

Figure 2.3 *Titrimetric studies indicate the interaction between the oligomer **15b** and BPNSs in water, as observed through UV-Vis absorption measurements, (a) the scattering lowered upon gradual addition of **15b** to the BPNS dispersion after zeroing (inset: original spectra without zeroing), (b) peak absorbances of the **15b**-BPNS composites with no shift in peak positions as compared with the pure **15b** (inset: precipitation was observed at the bottom of the cuvette).*

We were interested in understanding the surface phenomena and interactions between the molecules and the BPNSs. However, directly characterising these interactions experimentally is challenging because the two species differ considerably in both structure and size. As a result, obtaining direct evidence of their interactions can be difficult. We therefore examined changes in surface charge as an indirect measure of interfacial processes. In this context, Zeta potential measurements provide a useful estimate of charges near the slipping plane of the nanosheets and can reveal changes around the nanosheets arising from molecular interactions.

The way Zeta potential works is by applying an electric field to a sample and using a laser to detect the speed of particle movement via Doppler shift. This movement speed (electrophoretic mobility) is then converted mathematically through various approximations into a millivolt (mV) value which represents the electrokinetic potential. Hence, ideally the molecules shouldn't show any Zeta potential until and unless there is some sort of assembly occurring. BPNSs can form stable dispersions in water, are charged as we discussed before and able to scatter light. Suspended BPNSs showed a Zeta potential of −33 mV. All three viologen derivatives were checked for Zeta potential and only the oligomer **15-Cl$_x$** showed a positive value, while the other molecules (since they were dissolved; no particles) didn't show any Zeta potential.

$$mass\ fraction\ =\ W_{material}/W_{material\ +\ BPNS}$$

During the titration, we started off with the pure BPNSs and increased the mass fraction of the viologen derivatives. For the compound **3** (**Figure 2.4a**) and oligomer **15** (**Figure 2.5**), the Zeta potential started increasing and eventually went above −20 mV. Dispersions with Zeta potentials approximately within 0 mV and ±20 mV are often considered susceptible to aggregation because electrostatic repulsion may be insufficient to prevent particle-particle interactions (such as van der Waals forces). This essentially suggests that the composite dispersions were getting increasingly unstable, i.e., precipitations were becoming more likely event. However, with careful consistent considerations, charge neutralisation point was achieved by further increasement of the mass fractions where the Zeta potential value was very close to zero. This charge neutralisation occurred at a mass fraction of 0.84 for compound **3**.

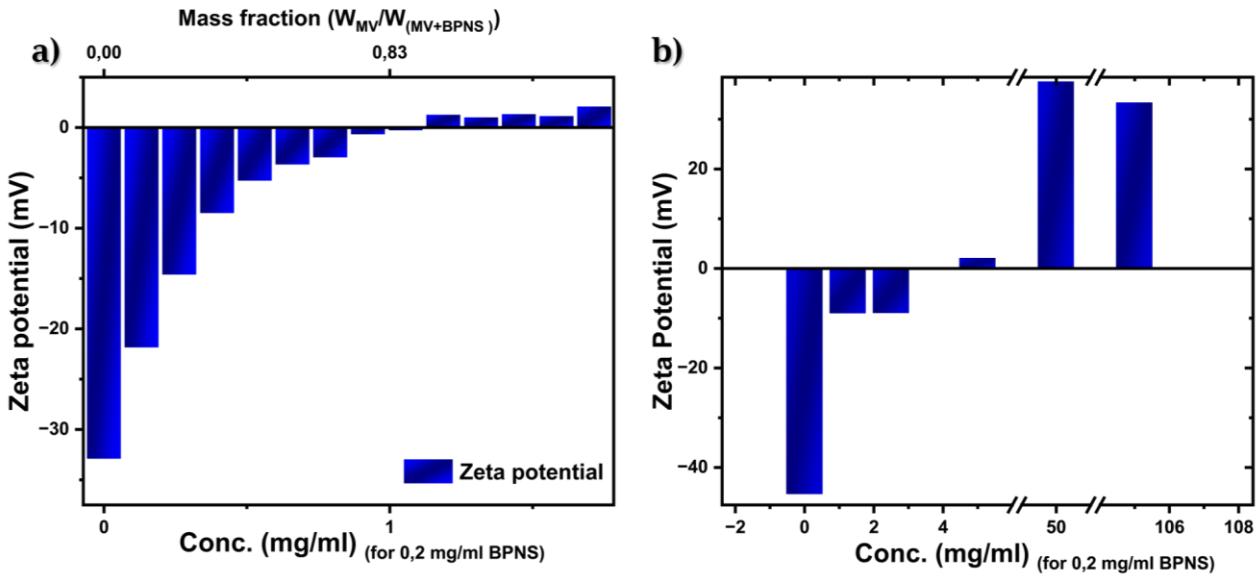

Figure 2.4 *Titrimetric studies of the composite formation observed through Zeta potential measurements, (a) with compound **3** and (b) compound **9**. Compound **9** didn't show any clear trend and has been very abrupt in terms of changes in Zeta potential compared to compound **3**.*

Furthermore, with an increase of mass fraction for compound **3** the Zeta potential value did not increase beyond +3 mV. However, for the corresponding experiments with compound **9** no such trend was observed (**Figure 2.4b**), instead the values showed abrupt, unexplainable changes.

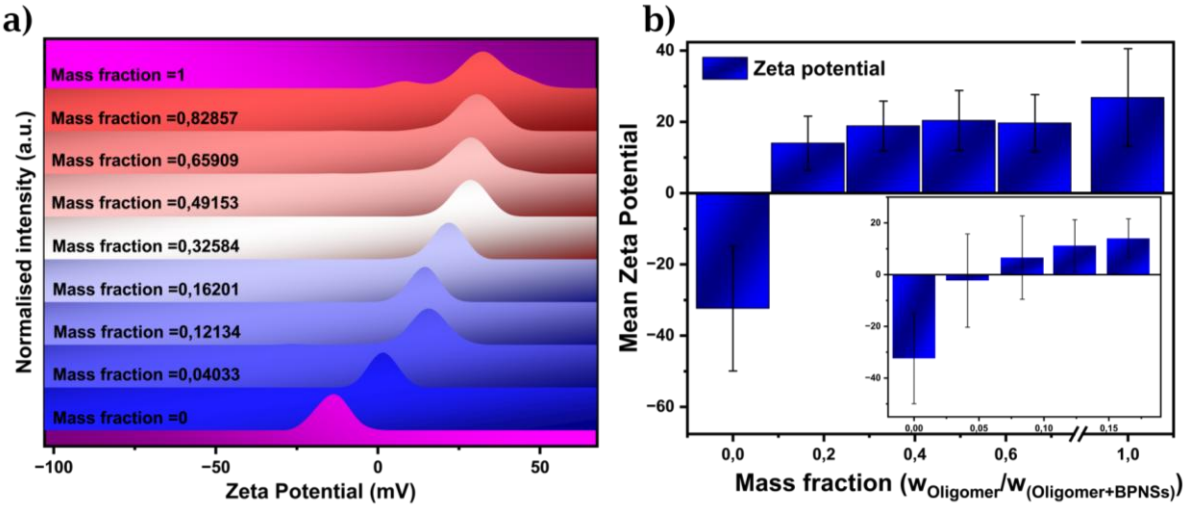

Figure 2.5 *Zeta potential titration for the* ***15b****-BPNS composite systems, (a) Zeta potential values of the composite plotted against the normalised intensity with the increment in oligomeric mass fractions, (b) mean Zeta potential increment with the increase in oligomeric mass fractions (neutralisation-point was achieved between the oligomeric mass fraction of 0.04 and 0.08 (inset)).*

As we saw in the synthesis scheme before, the oligomer is positively charged with negatively charged chlorides serving as counter anions. Since small molecules and ions do not show Zeta potential, the positive value of +30.9 mV can only be attributed to the positively charged oligomer. Pure BPNS dispersions on the other hand showed a Zeta potential of –13.9 mV. Same as before, with the increasement of mass fraction for the oligomer-**15b**, the mean Zeta potential of the pure BPNSs was observed to be shifted towards less negative value (normalised intensity distribution provided in **Figure 2.5a**) and the charge neutralisation point was observed at a mass fraction between 0.04 and 0.08. The mean Zeta potential was further observed to increase with increment in mass fraction and finally converge towards the Zeta potential value of the pure oligomer.

2.3.2 Characterisation studies for the composite systems

For compound **3**, the sample was prepared by simple mixing of the components in solution, followed by collection of the resulting precipitate. In contrast, for compound **9**, an excess of the compound was dispersed in a common solvent and the solvent subsequently removed by evaporation to obtain a mixture. This approach was chosen to improve the homogeneity of the components within the sample. For oligomer **15a**, however, a grinding step in a well-dispersing solvent was introduced before solvent evaporation. This was done to reduce the likelihood of phase separation, thereby improving sample homogeneity despite precipitation during preparation.

The composites prepared from the methods discussed above were compared against the pure BPNSs and the pure molecules through ATR-FTIR and Raman spectroscopy. The vibrational fingerprints from the molecules were observed at 1647 (C=N assym. Str.), 1574 (C=C ring str.), 1512 (N–CH_3 str.), 1450 (C–N str.) and 818 cm^{-1} (F–P–F str.) for compound **3** whereas 1639 (C=N assym. Str.), 1501 (C=C ring str.), 1446 (N–CH_3 str.), 1342 (C–N str., aromatic) and at 818 cm^{-1} (P–F anitsymm. str.) for compound **9** (**Figure 2.6**). Interestingly, the peaks at 1512 and 1450 cm^{-1} for compound **3** and 1501 and 1446 cm^{-1} for compound **9** looked like doublets which most likely originated from the coupled rings in the linear

molecular systems. The broad peak around 1018 cm^{-1} (P–O str.)[69] for pure BPNSs (**Figure 2.6a, b**) is an indication of minimal oxidation of the BPNS samples.

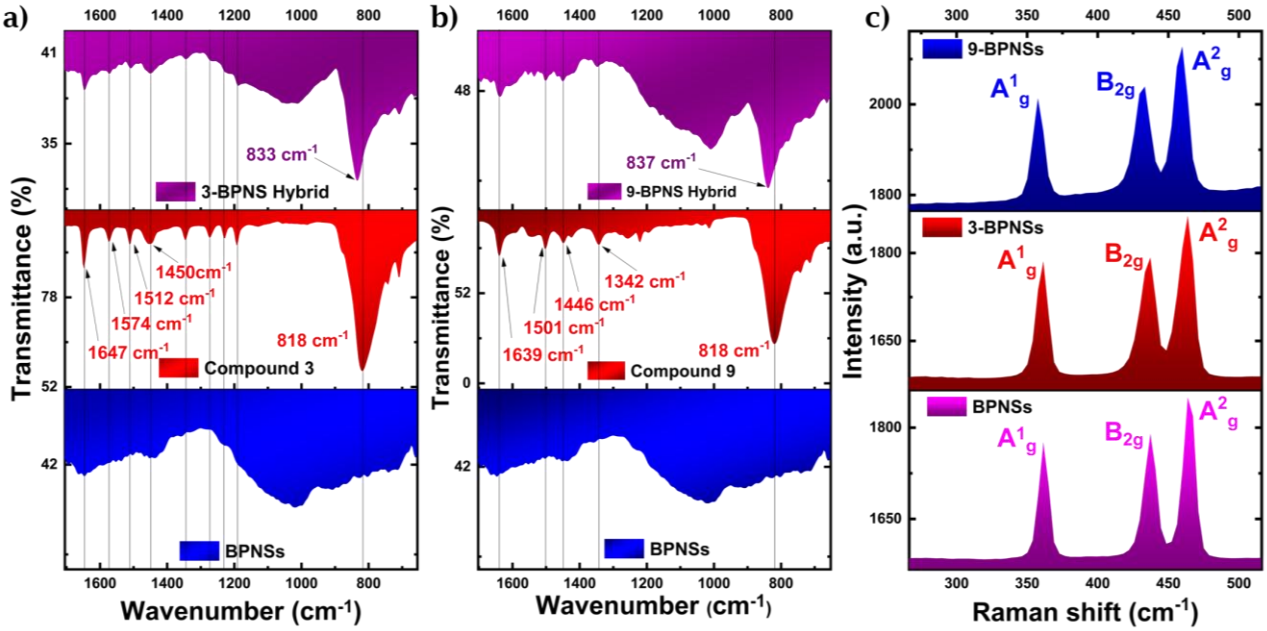

Figure 2.6 *Vibrational studies showing the presence of molecular and nanosheet features in the hybrid materials. ATR-FTIR comparing (a) BPNS and compound **3** with **3**-BPNS hybrid and (b) BPNS and compound **9** with **9**-BPNS hybrid. In (c) we can see the characteristic Raman modes of the BPNSs still intact in both **3**-BPNS and **9**-BPNS.*

ATR-FTIR is not a very sensitive characterisation technique in itself to investigate small changes in peak positions and is very dependent on the resolution used. For the pure BPNSs and the composites, ensuring good quality data meant sacrificing minor resolution. Although, no significant peak shift of the molecular signals could be observed, the presence of the molecular signals implied the presence of molecules in the composites. This was especially true for **3**-BPNS since this sample was purely from precipitation unlike **9**-BPNS, where excess compound **9** was added to ensure the presence of the molecule. Despite the resolution loss, a blue shift for the F–P–F stretching frequency was observed for both the composites (**Figure 2.6a, b**) which could come from the restriction for the specific stretching mode in the solid-state composite.

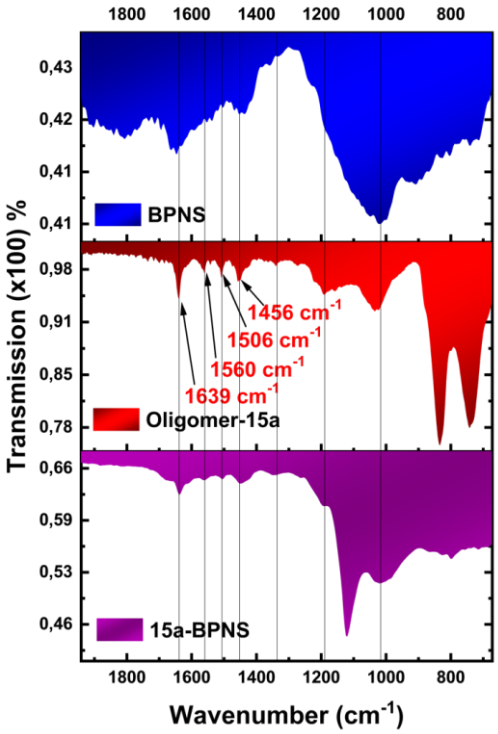

Figure 2.7 *ATR-FTIR comparing BPNS and oligomer-**15a** with **15a**-BPNS hybrid.*

The same composites were also investigated through Raman spectroscopy and for the BPNSs, 3 sharp peaks were observed at 362, 437 and 468 cm^{-1}. These corresponds to the out-of-plane symmetric phonon mode A^1_g and the in-plane bending mode B_{2g} and A^2_g, respectively

(**Figure 2.6c**).[70] The average Raman spectra of the composites were also recorded by averaging over 20 spectra for each of them, and the A^1_g to A^2_g ratio were found out to be 0.719, 0.716 and 0.693 for the pure BPNSs, **3**-BPNS and **9**-BPNS composites, respectively. The A^2g mode has been reported in literature to reduce with increase in oxidation and $A^1_g/A^2_g > 0.2$ is a characteristic of low oxidation levels.[71] This indicates minimal oxidation throughout the composite preparation steps.

Going further into the **15a**-BPNS composites, the vibrational modes of the oligomer-**15a** were examined at 1639 (C=N assym. str.), 1560-1506 (C–C ring str., aromatic), 1456 (C–H bend, alkane) and 1342 (C–N str., aromatic) cm^{-1}. The distinct P–F (740 & 833 cm^{-1}) bands of the oligomer could not be observed in the composite. Instead, a new band appeared approximately at 1118 cm^{-1} which may be associated with the aggregation of the oligomer around the nanosheets (**Figure 2.7**).

2.3.3 Morphological studies for the composite systems

The morphological studies were conducted to investigate the hybrids in detail and were compared against the bare nanosheets and pure compounds. The crystallinity of the viologen derivatives could be seen in as solid block-like features for both **3** and **9**, with some bonus rod-like structures in **3** (**Figure 2.8b, c**). Thin-flake like features are characteristics for the BPNSs and can be observed in abundance in case of the composites (both **3**-BPNS and **9**-BPNS, **Figure 2.8e, f**). However, occasionally large solid forms were observed scattered throughout the samples, and comparatively more in **9**-BPNS. This might have resulted from the higher addition of molecule-**9** during the composite formation, as this system proved difficult to precipitate. The presence of the flake features in the composites indicated that the overall morphology stayed more or less the same.

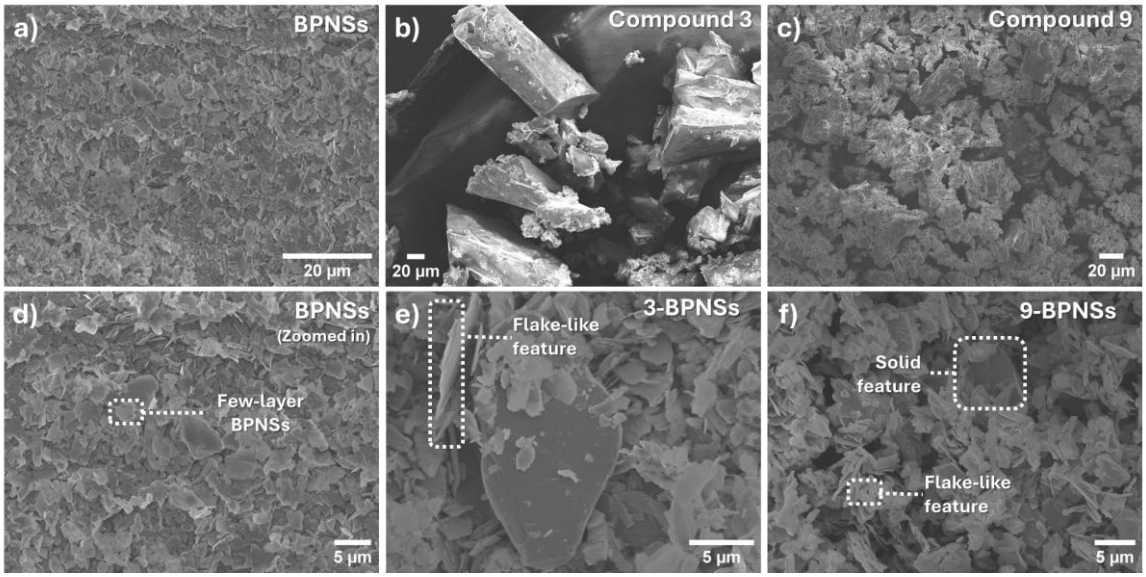

Figure 2.8 *SEM images showing the morphology of (a) BPNSs, (b) compound **3**, (c) compound **9**, (d) BPNSs (zoomed in), (e) the **3**-BPNS hybrid and (f) **9**-BPNS hybrid.*

The preparation of the samples for oligomer-BPNS composite was very challenging because of the rapid aggregation of the components and the need to obtain samples with a high degree of homogeneity. To minimise sample inhomogeneity and oxidation, BPNS and oligomer **15a** (1:1, wt. ratio) were mixed using grinding method in dry DMSO under

constant nitrogen flow. The dry samples for the SEM studies were obtained by evaporating the DMSO under high vacuum. The morphology of the composite samples contained amorphous oligomeric depositions (**Figure 2.9d-f**) onto the nanosheet surfaces which were observed to be completely absent in the bare nanosheet surfaces. This indicates the formation of composite materials with the flake-like features of the nanosheets being retained.

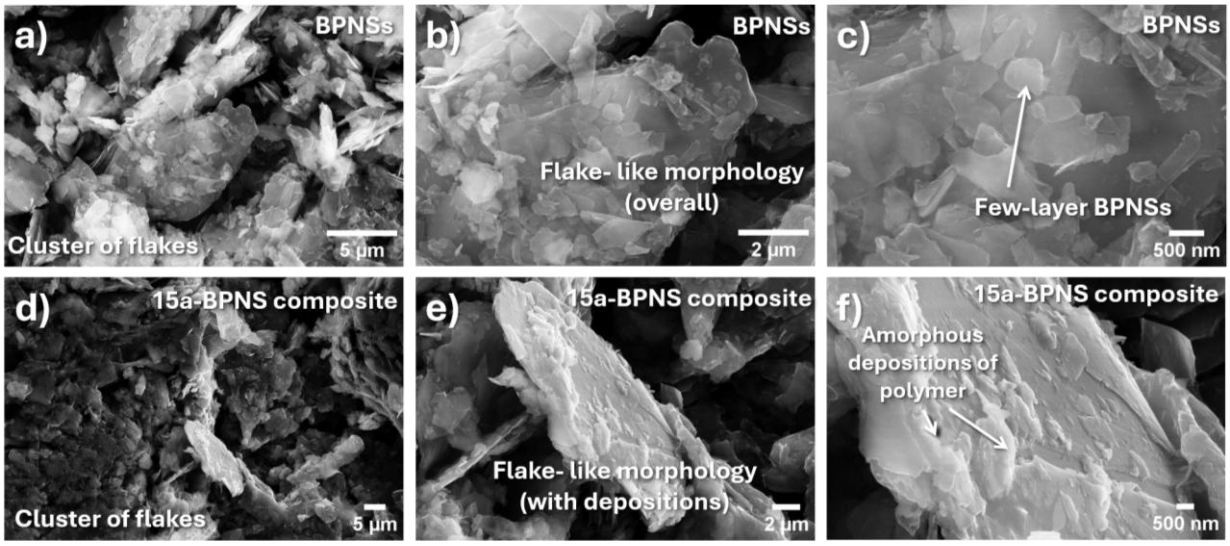

Figure 2.9 *SEM images of (d-f) the* ***15a****-BPNS composite compared against (a-c) BPNSs. Flake-like features are central to all however the amorphous depositions could only be seen in* ***15a****-BPNS composites (e, f).*

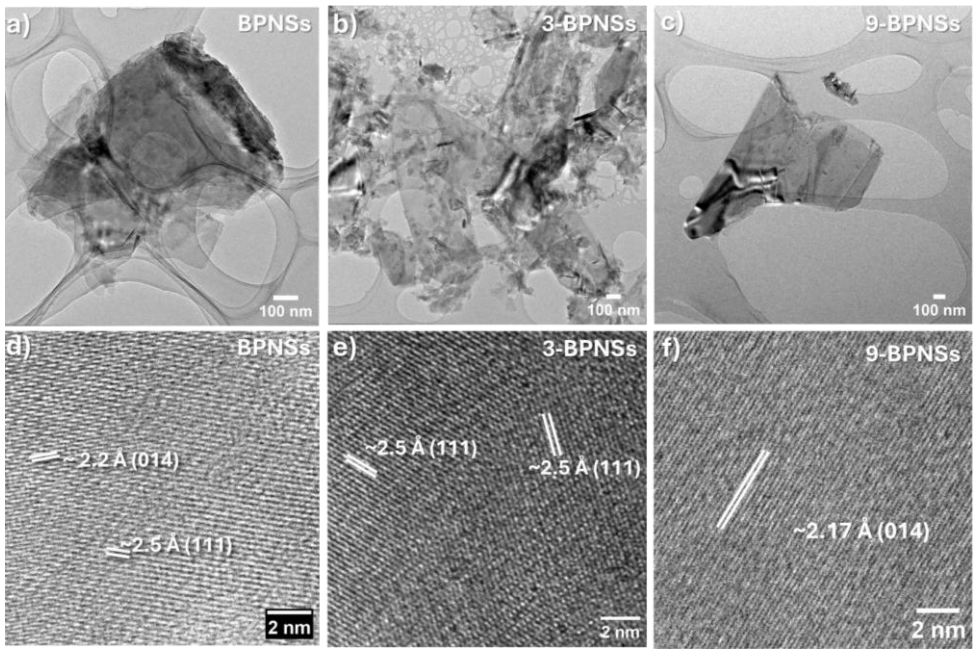

Figure 2.10 *TEM and HR-TEM images of (a, d) BPNSs, (b, e)* ***3****-BPNS hybrid and (c, f)* ***9****-BPNS hybrid.*

Transition electron microscopy (TEM) and high resolution-TEM (HR-TEM) measurements were performed on the samples for a further look at the morphology, specifically on the lattice parameters of the nanosheets. Lattice fringes with d-spacings of about 2.5 Å and 2.2 Å for the (111)[72] plane and (014)[73] plane, respectively are clear indicators of the bare

nanosheets and were observed in the HR-TEM images (**Figure 2.10d**). The (111) plane of the BPNSs in **3**-BPNS composite, having a d-spacing of 2.5 Å, implies unchanged crystallinity of BPNSs in the composite (**Figure 2.10e**). The (014) plane was observed in the case of the **9**-BPNS composite with a d-spacing of 2.2 Å (**Figure 2.10f**). Interestingly, the aggregated nature of the **3**-BPNS composite was observed in the TEM images as agglomerated clusters (**Figure 2.10b**). The **9**-BPNS composite did not show such morphology (**Figure 2.10c**), instead smooth and planar flakes of BPNSs can be seen onto the carbon-grid. This essentially means that the molecules of compound **9** due to its likely weak binding nature with the nanosheets had slower aggregation kinetics and hence, stayed in the solution phase. While the dissolved compound **9** passed through the carbon-grids, the bare nanosheets were left behind onto carbon grid.

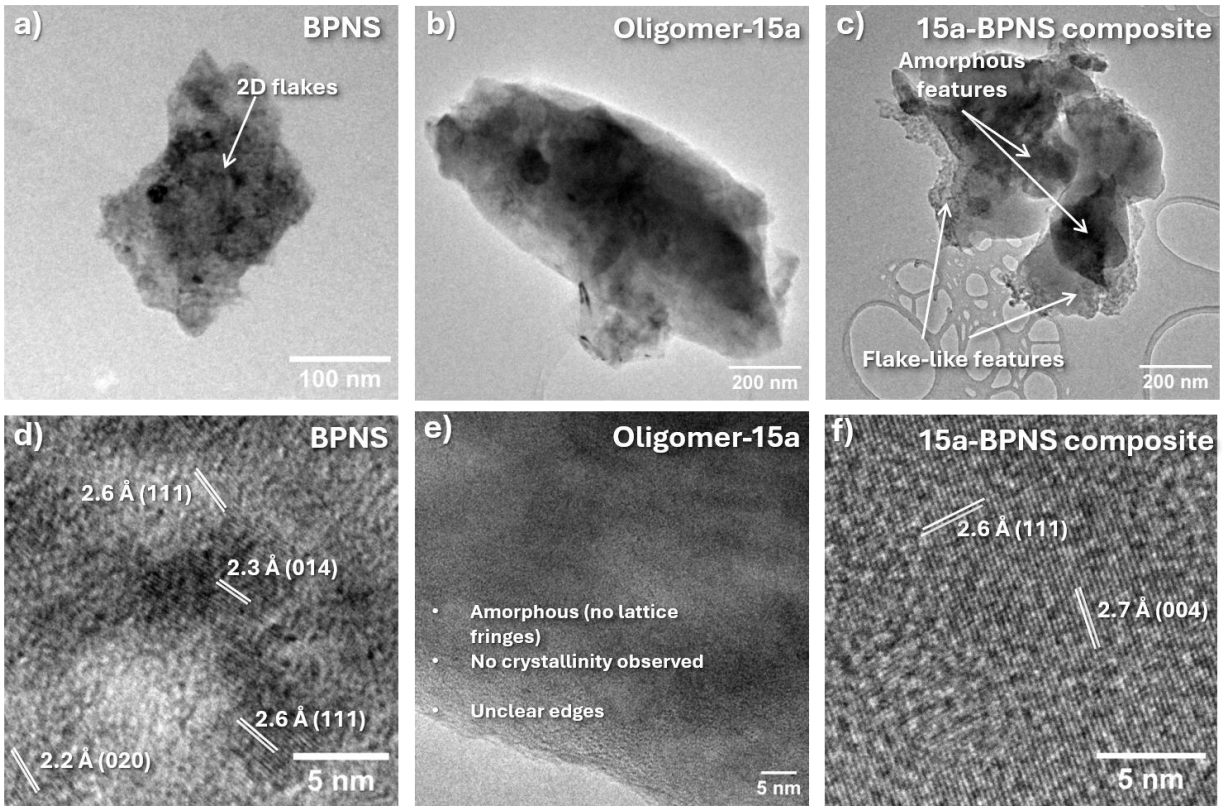

Figure 2.11 *TEM (a-c) and HR-TEM (d-f) images of (a, d) BPNSs, (b, e) oligomer-**15a** and (c, f) **15a**-BPNS composites. The lattice fringes have been assigned using the crystallographic data provided by Hultgren et al.[74]*

The **15a**-BPNS composites were investigated and compared with the bare nanosheets and pure oligomer-**15a**. The pure oligomer-**15a** exhibited neither lattice fringes nor well-defined edges. In addition, its apparent edge boundary changed with variations in the focal plane (**Figure 2.11b, e**) pointing towards its amorphous character. Similar amorphous regions were observed in the composite (**Figure 2.11c**), where they appeared in association with the BPNS flakes, suggesting aggregation of the oligomer on the nanosheet surfaces. Nevertheless, the characteristic lattice fringes of BPNSs were retained in the composite and remained comparable to those of the bare nanosheets (**Figure 2.11f**). Notably, the flake-like morphology of the nanosheets remained clearly visible in the composite, indicating that the oligomer formed only partial coverage rather than a continuous coating.

2.3.4 Ambient stability studies for the composite systems

The ambient stability of the composites was investigated using X-ray photoelectron spectroscopy (XPS). The physicochemical and morphological studies suggested that there are indeed interactions between some of the molecules and BP nanosheets. I wanted look into whether the functionalisation is effective enough to protect the nanosheets from the ambient degradation. Control experiments were performed by preserving the bare BPNSs and both the composites under inert nitrogen environment for 6 days. Another group of the same samples was exposed to ambient conditions for the same time interval, and the experiment was repeated several times to ensure reproducibility.

Electrons possess both orbital angular momentum (l) and intrinsic spin (s), and the interaction between these are known as spin-orbit coupling. This is the factor responsible for the peak splitting in XPS spectra. Intuitively, this can be understood by considering the electron's frame of reference, in which the nucleus appears to orbit around the electron and generates an effective magnetic field. Electrons due to their own spin have a magnetic field that can align either in the same or in the opposite direction with the magnetic field generated by their orbital angular momentum. The configuration with alignment in the same direction is a high energy configuration and hence, has lower binding energy compared to the opposite alignment. This coupling terms is expressed as j ($j = l \pm s$) and for 2p orbitals ($l = 1, s = 1/2$) of phosphorus, the two configurations are expressed as $2p_{3/2}$ ($j = 3/2$) and $2p_{1/2}$ ($j = 1/2$).[75]

To get a good understanding of the chemical nature of the P-atoms in the BPNSs, we cannot directly look at its valence shell. The valence shell consisting of 3s and 3p orbitals is loosely bound (low binding energy) and results in broad valence band spectrum. Although the core electrons in 2p orbital do not participate in the valence band, they still feel the electrostatic environment created by all the other electrons including the valence shell electrons. For example, if the phosphorus gets oxidised, the electronegative oxygen atom in the resulting P–O bond will pull the valence electron cloud away from phosphorus. This will result in stronger effective nuclear charge with less shielding from the electrons, resulting in a higher binding energy.

Freshly prepared nanosheets do not have pentavalent phosphorus species, only trivalent phosphorus is predominantly found. The $2p_{3/2}$ and $2p_{1/2}$ belong to all the trivalent species. However, when a sample of BPNSs was exposed to ambient conditions, the $2p_{3/2}$ and $2p_{1/2}$ with higher binding energies appeared which were attributed to the different P–O bonds (~163% increase over 6 days, **Figure 2.12a, b**). The peak positions could be found in **Table 2.1** below.

The P–O content (phosphorus oxygen index: *POI*) is calculated as the peak area from the deconvoluted spectra and is representative of the pentavalent phosphorus species. The overall oxidation extent was estimated by calculating *POI*-increasement given by,

$$Oxidation\ extent = \left[\left(\frac{POI_{ambient}}{POI_{protected}} - 1\right) \times 100\right]\%$$

The oxidation extent was averaged over multiple experiment to give average P–O content increasement.

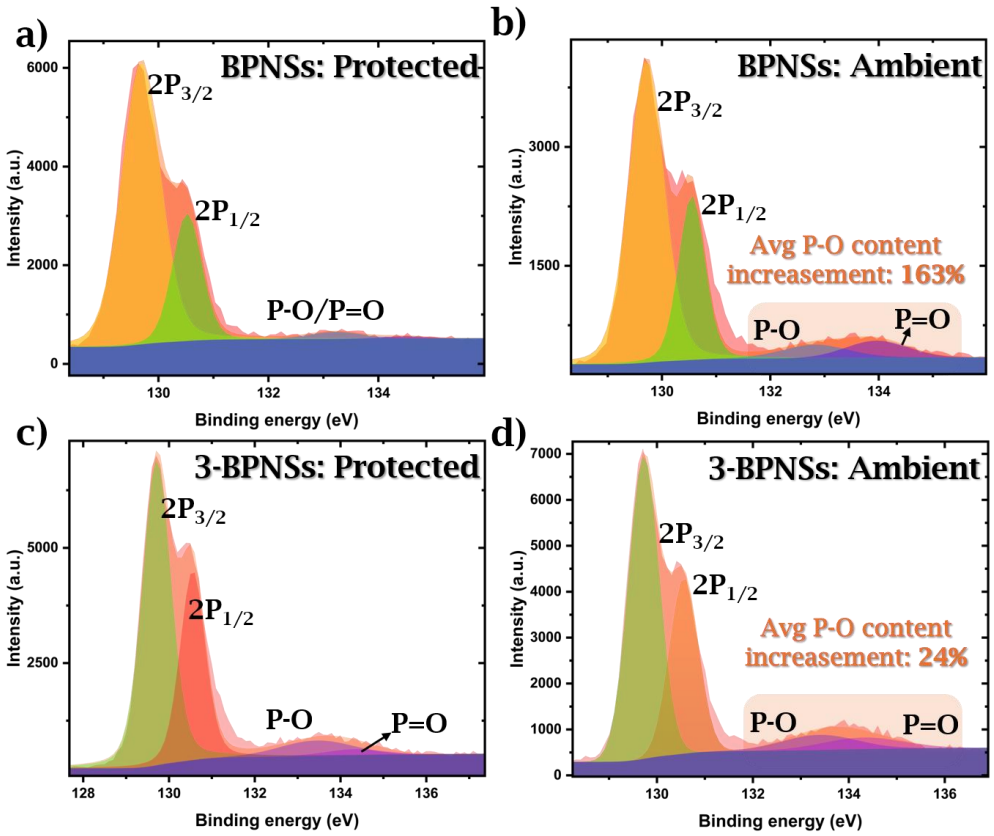

Figure 2.12 *P2p XPS spectra of (a, b) BPNS under protected and ambient conditions. (c, d)* ***3****-BPNS composites under protected and ambient conditions.*

Here we must keep in mind that when the hybrids were prepared, oxidation happening during the process could not be avoided. However, if we compare the oxidation of the **3**-BPNS hybrid exposed to the same ambient condition as the pure nanosheets to the same hybrid kept in the protected conditions the extent turns out to be increased by just about 24% (**Figure 2.12c, d**).

Table 2.1 *P2p binding energies of BPNSs and* ***3****-BPNS in XPS measurements.*

Binding Energy	**BPNS$^{(P)}$ (eV)**	**BPNS$^{(A)}$ (eV)**	**3-BPNS$^{(P)}$ (eV)**	**3-BPNS$^{(A)}$ (eV)**
$P2p_{3/2}$ $P2p_{1/2}$	129.69 130.53	129.71 130.55	129.62 130.46	129.73 130.57
P–O P=O	133.23 134.47	132.83 133.97	133.35 134.24	133.39 134.30

$^{(P)}$ Protected, $^{(A)}$ Ambient

We do not see the flake features of the nanosheets having any visible altercations when we look into the morphological studies which raises a question while reading this chapter, “Are the molecules really present?”. And this is very a valid question because all we see is that there is no difference in the oxidation extent in the **3**-BPNS hybrid. This is where N1s spectra come in, the presence of nitrogen indicate the presence of the nitrogen containing molecules which were not observed in the pure nanosheets.

But I mentioned that I used acetonitrile for all experiments, what if the N1s is coming from the acetonitrile instead? In N1s spectra we cannot see the acetonitrile usually observed at 397.7 eV.[76] Instead, I observed something very peculiar for the viologen type molecules, the charged nitrogen (N^+) and so called radical cation ($N^{\cdot+}$) at 400.7 eV and 399 eV for the protected composite and at 401.8 eV and 399.8 eV (**Figure 2.13**) for the composite in ambient condition.

The so called radical cation ($N^{\cdot+}$) is not an inherent component of the viologen structure, but has been reported to form through a reduction process induced by X-ray irradiation during XPS measurements.[77] Sampanthar et al. reported that their polymers (closely resembling our oligomer-**15a**) underwent a colour change from faint yellow to blue within the XPS chamber, which was attributed to the formation of radical cations.[78] Consistent with this observation, Wei *et al.* demonstrated that the radical cation signal persisted in methyl viologen (methyl viologen was being used as a charge carrier) while it was in its fully discharged state during operation in an aqueous battery.[79]

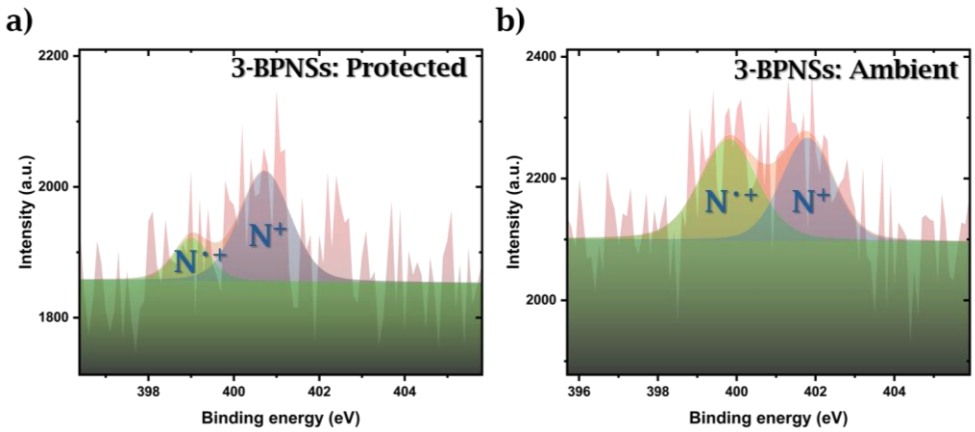

Figure 2.13 *N1s XPS spectra of **3**-BPNSs in (a) protected and (b) ambient conditions.*

However, in the case of the **9**-BPNS composite, an additional peak in the P2p spectra (**Figure 2.14**, **Table 2.2**) can be observed at 136.57 eV for the protected sample and at 136.18 eV for the sample stored under the ambient condition, which can be assigned to the P–F peak. This peak originates from the PF_6^- anion present in molecule **9** during the composite formation and I could not trace this peak in the **3**-BPNS composite as requirement of **3** for the composite preparation was much lower.

Table 2.2 *P2p binding energies of the **9**-BPNS composite in XPS measurements.*

Binding Energy	**9-BPNS_1$^{(P)}$ (eV)**	**9-BPNS_2$^{(P)}$ (eV)**	**9-BPNS_1$^{(A)}$ (eV)**	**9-BPNS_2$^{(A)}$ (eV)**
$P2p_{3/2}$	129.63	129.04	129.84	129.74
$P2p_{1/2}$	130.47	129.88	130.68	130.58
P–O	133.38	133.31	133.38	133.33
P=O	134.28	134.28	134.28	134.23
P-F	**136.57**	**136.18**	**136.73**	**136.92**

$^{(P)}$ Protected, $^{(A)}$ Ambient

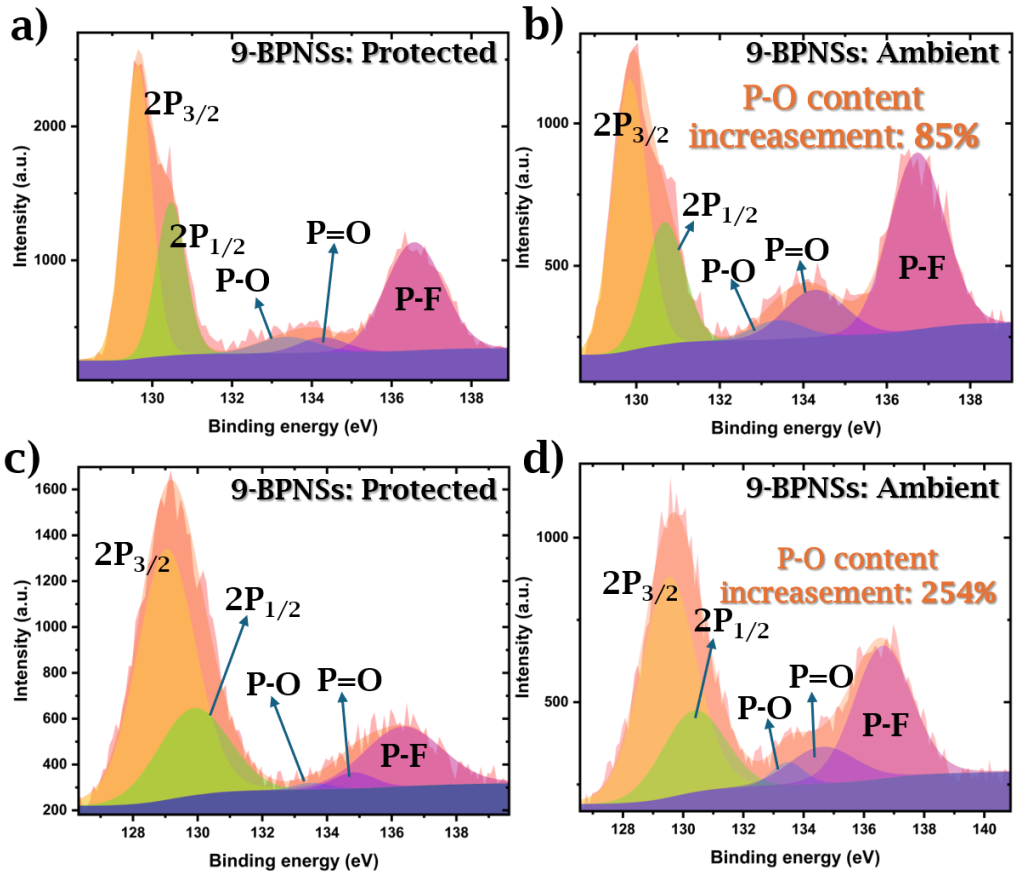

Figure 2.14 *P2p XPS spectra of the* ***9****-BPNS hybrid under (a, c) protected and (b, d) ambient conditions. The increase in the P-O/P=O content was compared under similar experimental conditions.*

15a-BPNS composite was very intriguing in many aspects. In the XPS results we occasionally observed the P–F signals in the P2p spectra (**Figure 2.15a, b**). The results were not convincing at all as a general trend was never established, rather a large variation even within the same sample. Multiple repetitions still could not conclude if the was helpful for the increasing the protection efficiency. And it will make sense if we look at it from the inhomogeneity perspective where the exposed part of the nanosheets might still be getting oxidised. The table below list the binding energies recorded for the composite compared to the pure nanosheets.

Table 2.3 *P2p binding energies of BPNSs and* ***15a****-BPNS in XPS measurements.*

Binding Energy	**BPNS$^{(P)}$ (eV)**	**BPNS$^{(A)}$ (eV)**	**15a-BPNS$^{(P)}$ (eV)**	**15a-BPNS$^{(A)}$ (eV)**
$P2p_{3/2}$ $P2p_{1/2}$	129.79 130.63	129.29 130.13	129.82 130.66	129.50 130.34
P–O P=O	133.51 134.03	132.98 134.26	133.43 134.44	133.38 134.26

$^{(P)}$ Protected, $^{(A)}$ Ambient

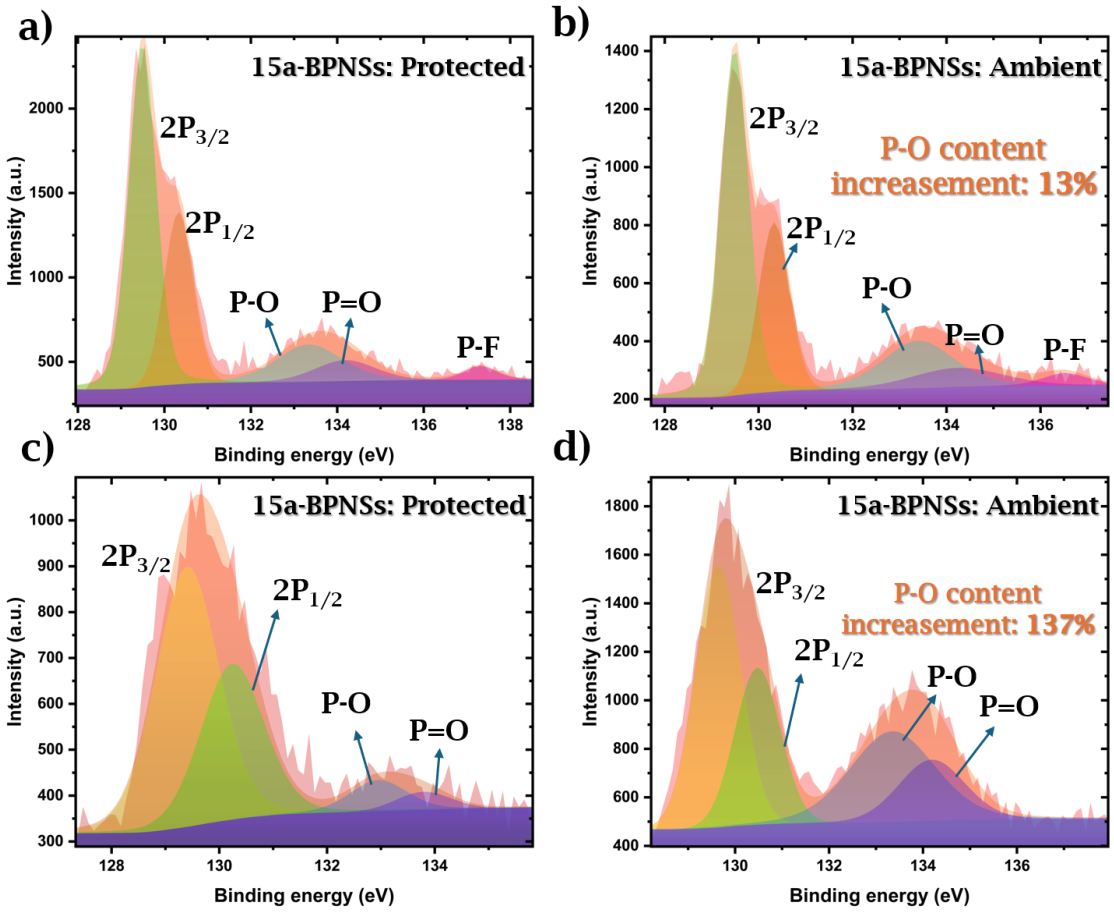

Figure 2.15 *P2p XPS spectra comparing P-O content for* ***15a****-BPNS composites kept in (a, c) protected conditions and (b, d) ambient conditions. Both the instances were performed in similar conditions, however, low oxidation for the composite could be observed from (a) to (b) and high oxidation could be observed from (c) to (d).*

2.4 Understanding the results

We have performed the ambient stability studies through XPS multiple times and checked the reproducibility of the systems to judge the consistency of protection efficiency. From all the evidence so far, the **3**-BPNS hybrid system was the only one to show signs of protecting BPNSs against the ambient degradation. **15a**-BPNS composites showed some degree of protection in some instances, but this behaviour was not observed consistently across the sample set (some samples were more oxidised than the bare nanosheets, experiment no. 3 and 5 in **Figure 2.16b**) and most likely dependant on the composite formation process. This means that the composite formation might be leading the passivation of the surface and there is not enough driving force present to direct the individual components to favourable binding. The TEM studies also point towards that direction. Aggregation was observed for **3**-BPNS but not for **15a-BPNS** due to the structural constraints. For the latter more exposed parts of the nanosheets were observed.

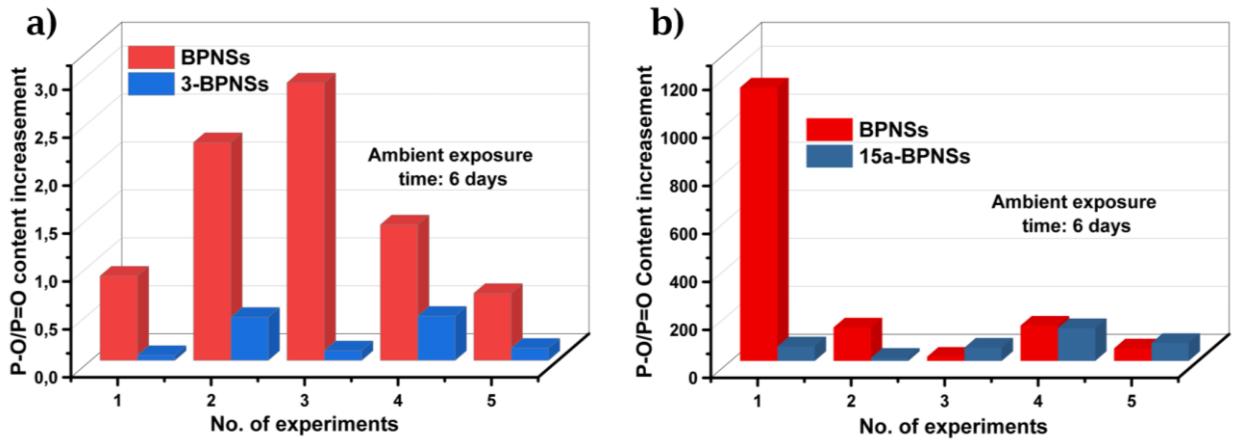

Figure 2.16 *A comparison of the extent of oxidation between (a) BPNSs and the* ***3****-BPNS and (b)* ***15a-BPNS*** *composites in various measurements over 6 days of ambient exposure.*

UV–vis and Zeta-potential measurements provided evidence of interaction, with changes in the UV–vis spectra indicating electronic interactions and changes in zeta potential suggesting electrostatic interactions. **3**-BPNS system showed signs of both types of interactions, **9**-BPNS behaved abnormally in Zeta potential titrations despite the peak shifts in the UV-Vis experiments, and **15b-BPNS** showed no clear indication in UV-Vis-based titrations, but Zeta potential titrations showed clear signs of interactions for **15b**-BPNS composites. A plausible interpretation is that the oligomer-**15** is interacting with BPNS more in an electrostatic manner and might be aggregating wherever there are more negatively charged surface groups (phosphates for BPNSs) onto the nanosheets.

2.5 DFT insights

The properties of the viologen derivatives (**3** and **9**) and their behaviour upon interacting with BPNS were investigated theoretically by our collaborators from *Nanjing Normal University, China* with the help of density functional theory (DFT) calculations. All first-principles calculations were implemented using the Vienna ab initio simulation package (VASP). The Perdew, Burke, and Ernzerhof (PBE) functional of generalized gradient approximation (GGA) served to approximate exchange-correlation functions and the projector-augmented wave (PAW) method was used to represent the core-valence electron interactions.[80]

The frontier molecular orbitals of **3** and **9** were calculated first. The highest occupied molecular orbitals (HOMO) were found to be −2.65 eV and −2.63 eV, and the lowest unoccupied molecular orbitals (LUMO) were found to be −0.94 eV and −1.25 eV for **3** and **9** respectively. The HOMO-LUMO gaps for compounds **3** and **9**, hence calculated, were 1.7 eV and 1.38 eV, respectively.

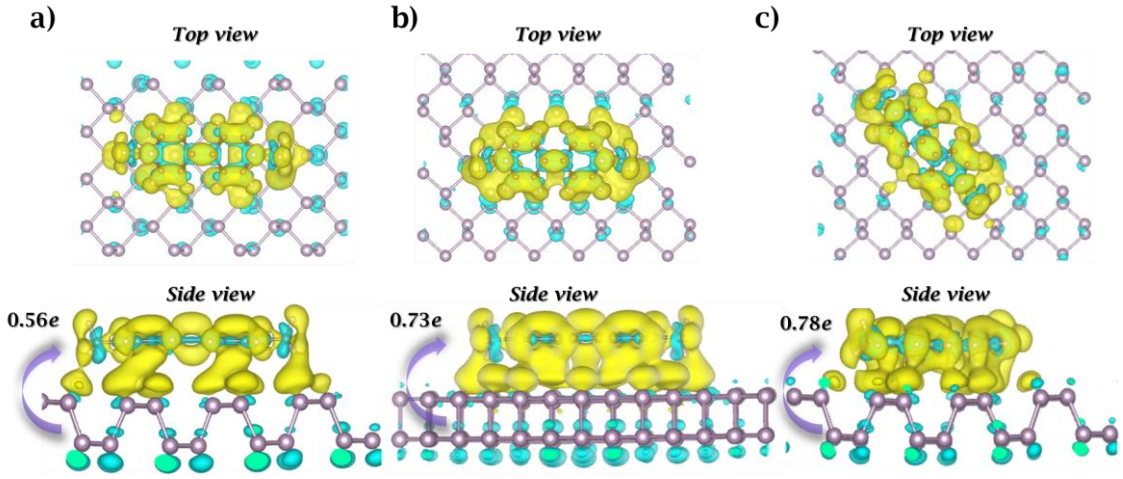

Figure 2.17 *Electron-density difference plots of the molecule **3** on top of a single-layer BPNS slab, (a) perpendicular to the ridge, (b) parallel to the ridge, (c) diagonal to the ridge. The yellow region represents areas of electron accumulation, while the cyan region indicates areas of electron depletion.*

Table 2.4 *Total and average adsorption energy of the **3**-BPNSs composites along different directions from the ridges of BPNSs calculated by DFT.*

Materials [3-BPNSs]	**E_{ads} (eV)**	**Number of atoms**	**E_{ads}/X (apprx.) (eV)**
Perpendicular	−1.45	28	−0.052
Parallel	−1.47	28	−0.052
Diagonal	−1.44	28	−0.052

Normalised adsorption energies while interacting with a single-layer BPNS surface, were calculated for **3** and **9** in parallel, perpendicular and diagonal direction to the ridges of BPNSs (**Figure 2.17**, **Figure 2.18**). For both compounds, the normalised adsorption energy is greater in the parallel direction, and the orbital overlap is also maximum in the parallel direction. It is noteworthy that the normalised adsorption energy value was found to be lower for compound **9** (−0.049 eV) compared to **3** (−0.052 eV) (**Table 2.4**, **Table 2.5**).

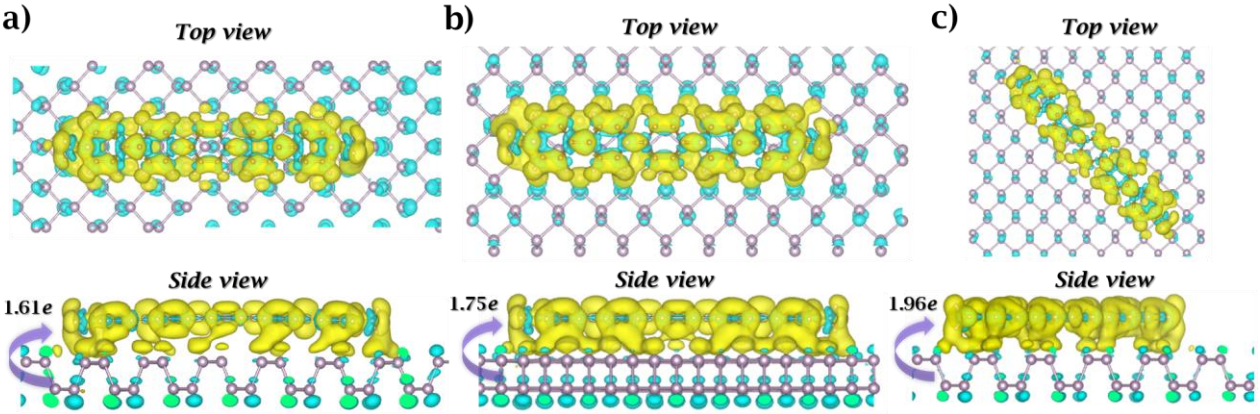

Figure 2.18 *Electron-density difference plots of the molecule **9** on top of a single-layer BPNS slab, (a) perpendicular to the ridge, (b) parallel to the ridge, (c) diagonal to the ridge. The yellow region represents areas of electron accumulation, while the cyan region indicates areas of electron depletion.*

Table 2.5 *Total and average adsorption energy of the* ***9****-BPNSs composites along different directions from the ridges of BPNSs calculated by DFT.*

Materials [9-BPNSs]	**E_{ads} (eV)**	**Number of atoms**	**E_{ads}/X (apprx.) (eV)**
Perpendicular	−2.74	58	−0.047
Parallel	−2.83	58	−0.049
Diagonal	−2.67	58	−0.046

The orbital overlap picture also suggests that the interaction of the nanosheets with the small molecules were possibly a type of cation-induced dipole interaction. In the parallel configuration, both molecules were predicted to have a charge-accumulation zone, which was measured to be 0.73*e* and 1.75*e* for the **3**-BPNS and **9**-BPNS composites, respectively (**Figure 2.17**, **Figure 2.18**).

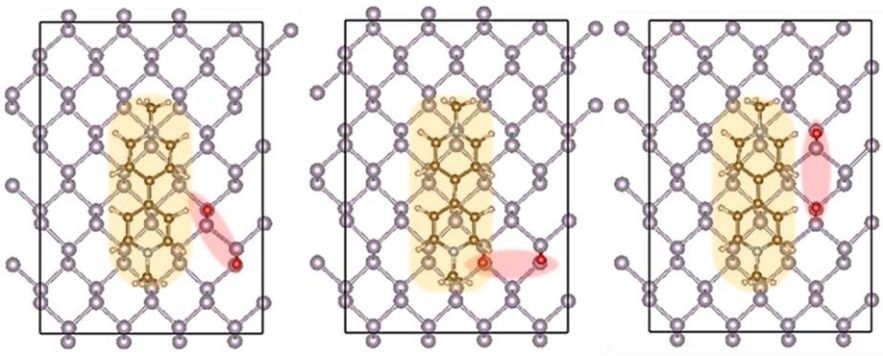

Figure 2.19 *Structures of O_2 after adsorption at different sites on* ***3****-BPNS.*

Oxygen adsorption on the nanosheets is one of the key phenomena and provides a deep insight into the degradation pathway of the nanosheets under ambient exposure. One of the key events during the process is immediate dissociation of oxygen molecules into atoms[65] on the nanosheet surface and the free energy of adsorption for the oxygen atoms (**Figure 2.19**) onto the nanosheet surface is a very crucial parameter for evaluating the ease of BPNS oxidation.

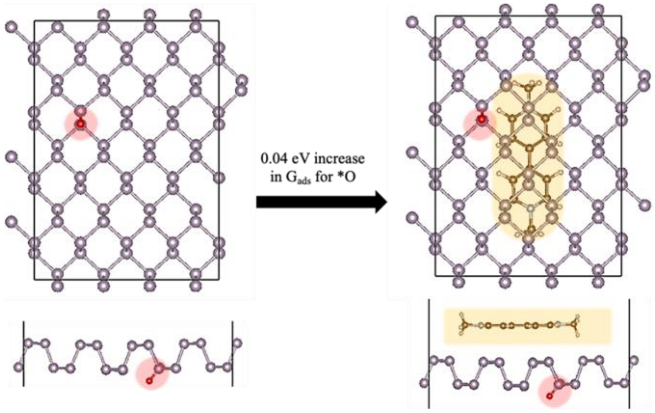

Figure 2.20 *The calculated adsorption-free energy increased by 0.04 eV for the* ***3****-BPNS composite, compared to the pure BPNS. Increment in free energy of adsorption usually implies energetically less favourable i.e. weaker binding to the surface. Here, the increment suggests that the adsorption of*

*oxygen atom is comparatively less favourable once the compound **3** is adsorbed onto the nanosheet surface.*

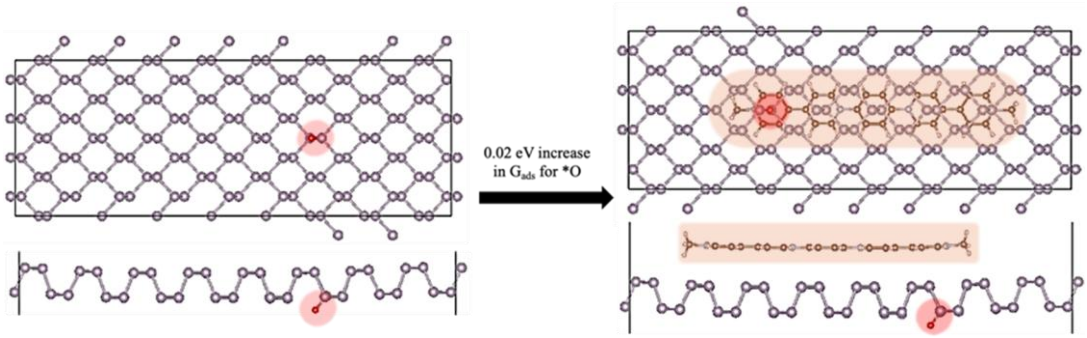

***Figure 2.21** The calculated adsorption free energy increased by 0.02 eV for the **9**-BPNS composite, compared to the pure BPNS. Here, the increment suggests that the adsorption of oxygen atom is less favourable once the compound **9** is adsorbed onto the nanosheet surface but will comparatively be stronger than the case of compound **3**.*

The Gibbs free energy for the adsorption of the oxygen atoms was calculated for the surfaces of pure BPNSs, **3**-BPNS and **9**-BPNS composites. Interestingly, the Gibbs free energy was calculated to be increased by 0.04 eV (**Figure 2.20**) and 0.02 eV (**Figure 2.21**) for the **3**-BPNS and the **9**-BPNS composites respectively, compared to that of pure BPNSs (possibly due to lesser electron density onto the exposed nanosheet surface). This suggests the more favourable and spontaneous nature of the oxidation process on the pure BPNSs, whereas the composites are comparatively less prone to oxidation (**3**-BPNS being the least prone). The calculations were performed for pure adsorption scenario and did not consider the following: the excitonic pairs generated on the nanosheets under light exposure and the charged superoxide radical anion species formed through electron transfer from the conduction band of the nanosheets to the molecular oxygen.

2.6 Beyond the initial set

As small molecules such as methyl viologens were found to provide effective protection to BPNSs, their counterparts bearing an oligo-styrene backbone were observed to be comparatively less effective. Consequently, a modified viologen-based design was considered, in which the methyl groups were replaced with alkyl chains terminated by aliphatic quaternary ammonium functionalities. Owing to the sp^3-hybridised nature of these ammonium centres, the positive charge is localised on the nitrogen atom. This was expected to increase the electrostatic contribution to the interaction with BPNSs while preserving a relatively compact molecular structure. Since these charges are localised and most likely to interact in electrostatic manner, hence, are very different from the cationic charges delocalised onto the π-cloud of pyridinium-type species. Two variants of such compounds were designed and synthesised with 3-C (**11a**) and 5-C (**11b**) long chains (**Scheme 2.4**).

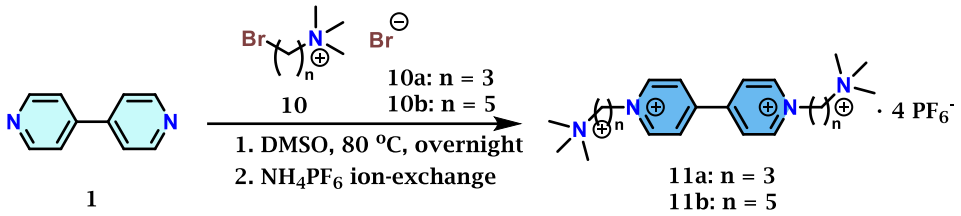

Scheme 2.4 *Synthetic route for compound* ***11****. The difference between the two variants is only the chain length.*

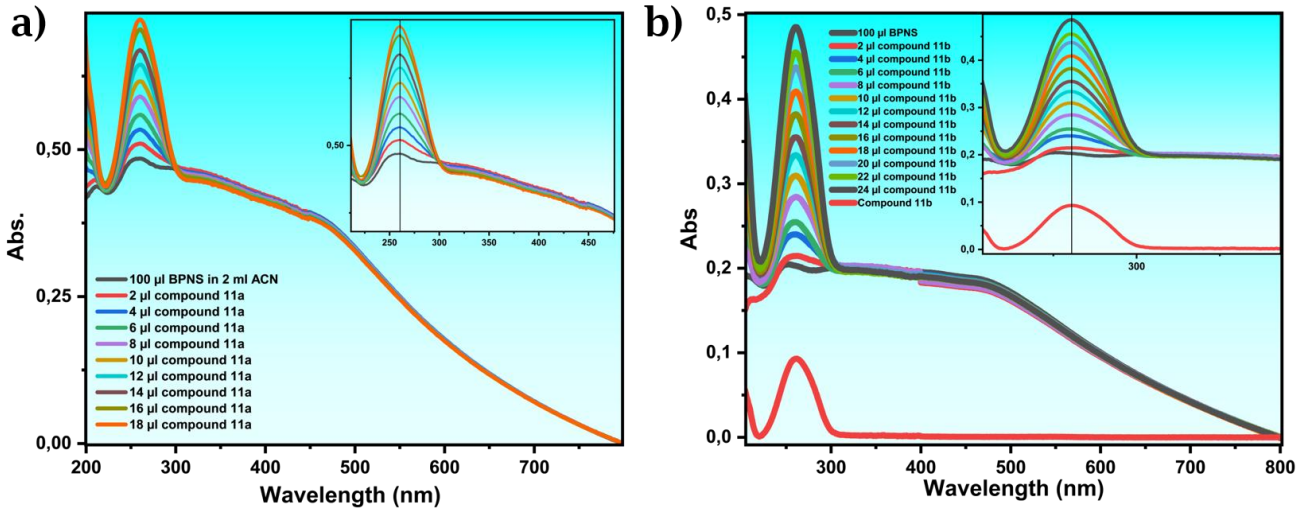

Figure 2.22 *Titrimetric studies with BPNSs using UV-Vis spectroscopy, (a) with compound* ***11a*** *and (b) with compound* ***11b****. No clear evidence of interaction was noted, the anomaly around 400 nm in (b) was caused by the lamp-changing from visible region to UV region inside the instrument.*

UV-Vis-based titrations with freshly prepared BPNSs didn't show any clear indication of the interaction. Neither have there been any shifts in the peak positions for either **11a** or **11b**, nor were there any visible precipitation or any sort of aggregation (**Figure 2.22**).

Precipitation usually tells us that the involved systems are coming together and forming aggregates, which is a classic sign of non-covalent interactions. Therefore, the absence of aggregation can also provide useful information. Adding bulkier end-groups and stronger electrostatic features might have kept the molecules apart from the nanosheets. Which reduced the close electronic contact that probably was driving aggregation for BPNSs, allowing the system to stay dispersed while the deeper electronic interaction becomes much weaker.

3. Functionalisation of MXenes for Improved Ambient Stability

3.1 The problem

$Ti_3C_2T_x$ MXene is an excellent electrical conductor because of its intrinsically metallic Ti–C lattice. Its surface terminations are not the primary origin of its high electrical conductivity but can tune the conductivity. However, the nature of the bonds between the transition metal and the surface terminations are of coordination type which also makes the material vulnerable to degradation. When exposed to air and especially to water, the surface begins to react, gradually degrading the crystalline structure of the MXene from a useful 2D conductor to less crystalline solids and finally into an unusable, white oxide powder.[81]

This degradation does not occur uniformly across the sheet. It typically begins at the flake edges and at structural defects.[82] At these sites, titanium atoms are less protected and more accessible to water and oxygen, and therefore, act as initiation points. Water molecules adsorb first, followed by dissolved oxygen, and together they generate reactive oxygen species capable of attacking the Ti–C bonds that hold the MXene lattice together. As these bonds break, titanium is released from the structure and oxidises to form nanoscale anatase TiO_2 crystals (rutile later);[83] the same compound found in sunscreen and white pigments. The carbon that remains no longer fits into an ordered lattice and instead collapses into a disordered, soot-like residue.

Over time, this process converts a smooth, conductive MXene sheet into a mixture of oxide particles and amorphous carbon, causing a sharp loss in electrical conductivity and mechanical integrity. Heat and light accelerate the reaction, and the presence of both water and oxygen is essential, which is why $Ti_3C_2T_x$ degrades far more rapidly in aqueous dispersions than as a dry powder or film. These sensitivities make storage conditions critical, e.g., keeping MXene dry, cold, oxygen-limited, and protected from light can significantly slow degradation, even though it cannot prevent it entirely. Any strategy aimed at stabilising MXene must therefore address this fundamental challenge i.e., minimising the access of water and oxygen to its reactive surface.

3.2 Working hypothesis and introduction to our MXenes

In our lab we follow a general procedure to prepare our own $Ti_3C_2T_x$–MXenes which involves an etchant based exfoliation method of MAX (Metal–Aluminium–Carbide/Nitride) powder in acidic media, followed by a manual shaking-based delamination method.[84] We use a combination of lithium fluoride (LiF) and hydrochloric acid (HCl) mixture to generate hydrogen fluoride (HF) in situ. This step is extremely important as Al–F bond is very strong (ΔHf_{298} = ~664 kJ/mol)[36] and gets etched away in the exfoliation process. This in turn not only takes away all the aluminium from the MAX powder leaving behind the 2D sheets of MXene (as 'A' leaves from 'MAX') but also adds the surface group to the MXene-sheets. Fluorides are the predominant nucleophiles in the etchant and hence have the high likelihood of being the surface functional groups. Here the bond dissociation energy also plays a huge role as Ti–F and Ti–O bonds both are very strong (Ti–F: ΔHf_{298} = ~569 kJ/mol,

Ti–O: ΔHf_{298} = ~662 kJ/mol)[36] and Ti–OH becomes the other dominant surface group due to plenty of water being present in the etchant media.

The etching process is performed at slightly elevated temperatures which also affects the surface groups. Over the temperature range of ~65-70 °C, the surface groups have more –OH groups compared to lower temperatures, such as 50 °C. At lower temperatures the surface groups have more –F groups. For the experiments discussed in this thesis, the MXene was exfoliated at 65 °C for maximizing –OH group concentration onto the sheets to observe clearly the changes during ambient degradation. MXene nanosheets exfoliated at 65 °C showed three very distinct and typical peaks for MXenes, the plasmonic band at 765 nm and the inter-band transitions at 270 nm and 320 nm. Identical absorption spectrum was recorded for MXene exfoliated at 50 °C apart from the plasmonic band around 750 nm which seemed to have shifted (**Figure 3.1**) in the earlier case.[85]

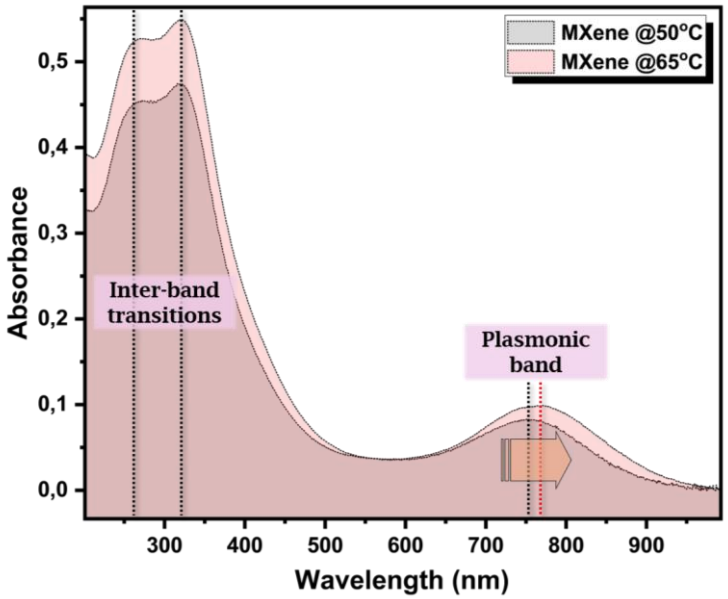

Figure 3.1 *Changes in absorption behaviour for the MXenes exfoliated in 50 °C and in 65 °C.*

Another interesting property of the MXene that originates because of its unique structure is that it gets a negative surface charge in aqueous media because of the overall coordination environment. This can be used for noncovalent type of interactions with our oligomer-**15b** with positively charged pendant groups described in the previous chapter. The hypothesis is that the charged part will interact with the 2D sheet leaving behind the hydrophobic backbone exposed, preventing water and oxygen to interact with the nanosheets (**Figure 3.2**).

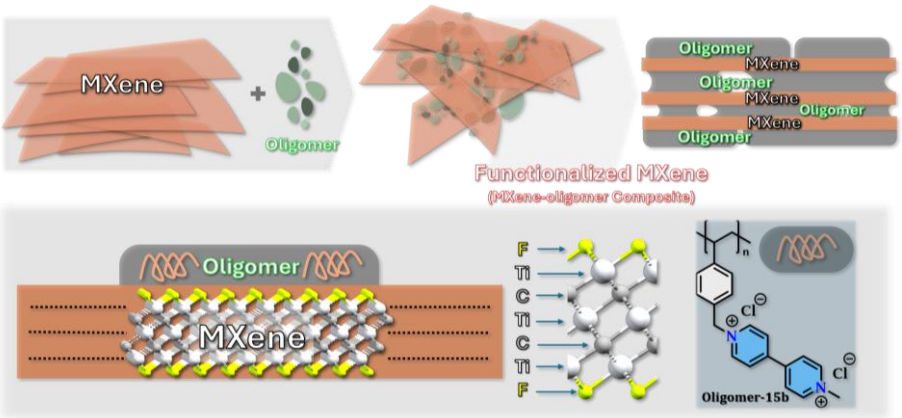

Figure 3.2 *Schematic illustration: composite formation and capsulation using oligomer-**15b**.*

To prepare the MXene–oligomer composite, $Ti_3C_2T_x$ MXene was dispersed in water to form a stable colloidal suspension followed by adding the charged oligomer-**15b** solution under

controlled swirling. A visible precipitate slowly appeared, marking the first clear sign of electrostatic binding and loss of colloidal stability. For characterisation in the solid phase, the resulting **15b**-MXene composite was collected by centrifugation and the solid was washed to remove any unbound oligomer.

3.3 Results and discussions

3.3.1 Physicochemical studies

The solubility of the **15b** in water was very good, therefore, titration experiments were conducted in water as solvent. Viologen motifs usually absorb around 258 nm (π–π*) as shown in previous chapters and this was also the case under the experimental conditions used in this study. In the unprocessed spectra, scattering loss (**Figure 3.3a**) was observed for the oligomer, evident from an abnormally high absorbance in the non-absorbing region. This behaviour is typical of dispersions and is also observed for pure MXene nanosheets, which scatter a fraction of the incident light. The spectra were normalised at 320 nm (**Figure 3.3b**) as that peak of the MXene nanosheets didn't have any overlap with the oligomer absorption and consequently observed the absorption converging at 262 nm. This didn't by itself tell us anything about the interaction as it might be resultant of two different peaks overlapping. But additionally, the scattering loss seemed to decrease with addition of the oligomer in the unprocessed spectra, simultaneously increasing the formation of larger aggregates. And at a mass fraction of 0.23 I found that the scattering loss along with absorption-loss started to stabilise and simultaneously λ_{max} converged to 262 nm (**Figure 3.3c**) as we discussed earlier.

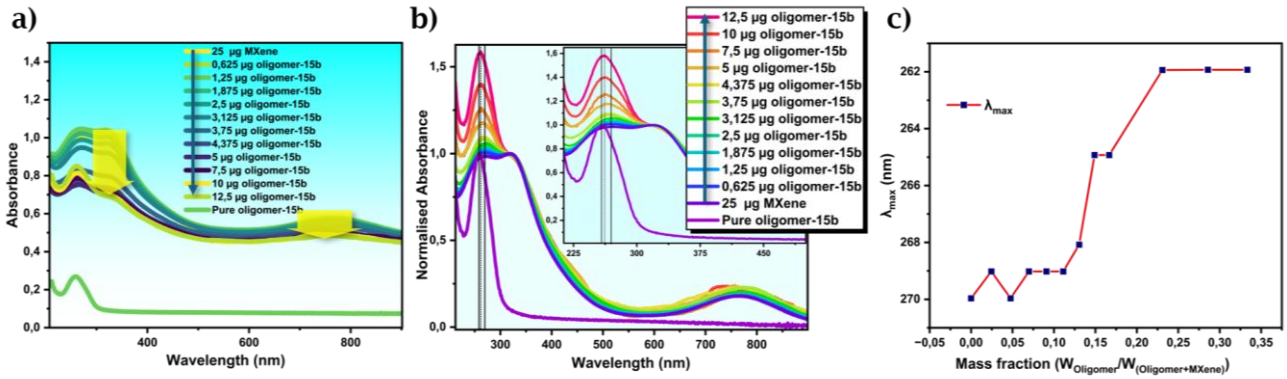

Figure 3.3 *Titrimetric studies using UV-Vis measurements indicating the interaction between **15b** and the MXene nanosheets, (a) raw data showing the decrease in absorption and the decrease in scattering with increasing oligomer-**15b** content, (b) normalised data at 320 nm to show the peak intensity of the oligomer rising and (c) the change in λ_{max} with increasing mass fraction of the oligomer.*

At first glance, this result may appear counterintuitive, since scattering intensity generally increases with particle size and, in the Rayleigh regime, scales with the sixth power of the particle diameter. However, the aggregates formed in this system were significantly larger than the wavelength of the incident UV-Visible light, reaching dimensions in the micrometre to sub-millimetre range. Consequently, the optical response is no longer governed by conventional Rayleigh or Mie scattering. Instead, reflection, refraction, and diffraction around the surfaces and edges of the aggregates become the dominant mechanisms influencing light propagation. Such behaviour is more effectively described by Fraunhofer

diffraction, which provides a better approximation for particles that are much larger than the wavelength of the incident light.

To further investigate the type of interaction between the MXene nanosheets and **15b**, Zeta potential based titrations were carried out. MXene possessed an overall very stable dispersion with a negative Zeta potential (−41.46 ± 4.45 mV, **Figure 3.4**), which upon addition of **15b**, slightly decreased and later increased to charge neutralisation point at a mass fraction close to 0.035. Further addition of oligomer rapidly increased the Zeta potential but beyond the charge neutralisation point didn't result in any rapid increasement of the Zeta potential (at mass fraction 0.18, observed Zeta potential: +24.74 ± 3.54 mV). However, the resultant Zeta potential of the **15b**-MXene composite was higher than that of the pure oligomer **15b** (+13.78 ± 1.03 mV) which might arise from larger hydrodynamic radii–distribution of the aggregates. Flocculation due to inadequate guest-oligomers could be observed in the lower mass fractions, but complete precipitations were never observed even after redispersing until the charge neutralisation point. The converging Zeta potential after the charge neutralisation point indicated saturated coating of the nanosheets as described by Hu et al., suggesting electrostatic interactions between the host-MXene and guest-oligomers.[86] The discrepancy of the mass fractions might arise due to electrostatic interactions rather than π-interactions as the oligomer dispersion is not at all planar which might reduce the effective surface necessary for the π–interactions.

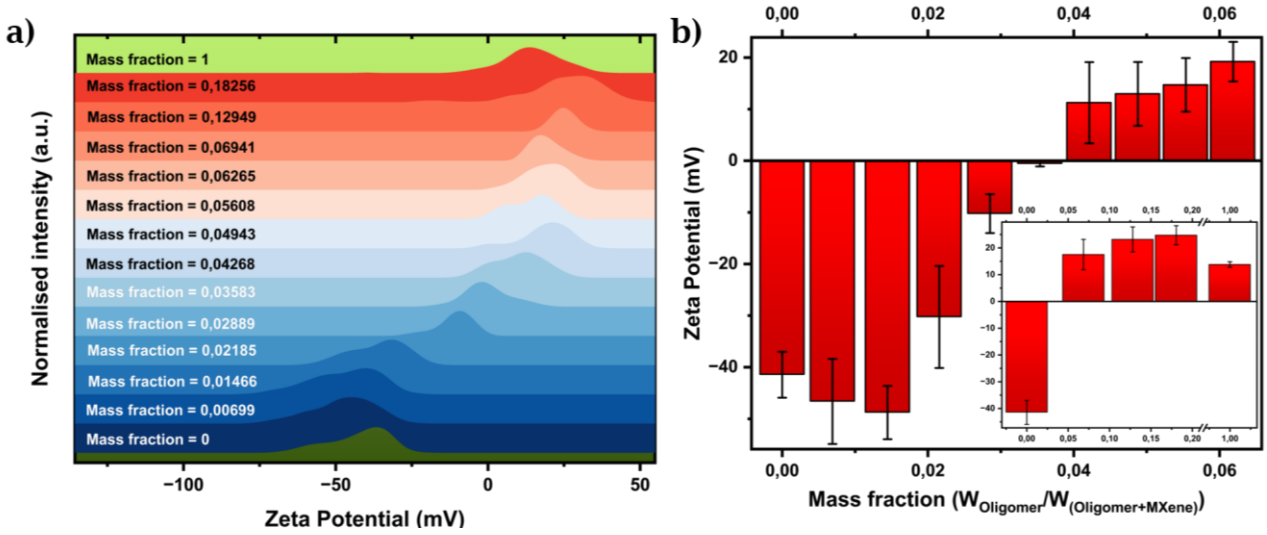

Figure 3.4 *Observation of composite formation using Zeta potential, (a) shift of potential distribution with increasing mass fraction and (b) overall change in Zeta potential (inset changes in higher mass fraction, notice the Zeta potential of the composite is increasing however is greater than the original oligomer).*

3.3.2 Morphological studies of the composites

MXene flakes are substantially different from BPNSs and are usually much thinner and more transparent. Also, due to the freeze-drying process it appears with more spaces in between. To identify the flakes, one must look at sharp edges of the flakes, together with an appearance similar to a snapshot of an explosion (**Figure 3.5a, b**). The flake features were seen in the composite samples but covered with translucent cotton like features (**Figure 3.5c, d**).

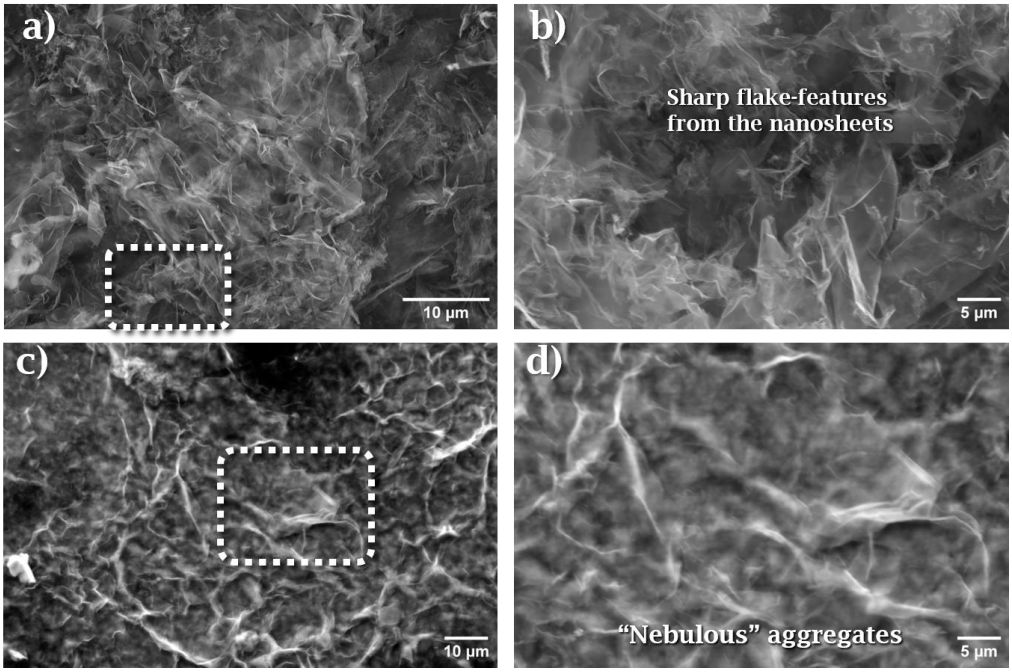

Figure 3.5 *SEM images showing the morphology of (a, b) bare MXene sheets, (c, d) nebular aggregates of the* ***15b****-MXene composite. (b, d) are the zoomed in images of the highlighted areas of (a, c).*

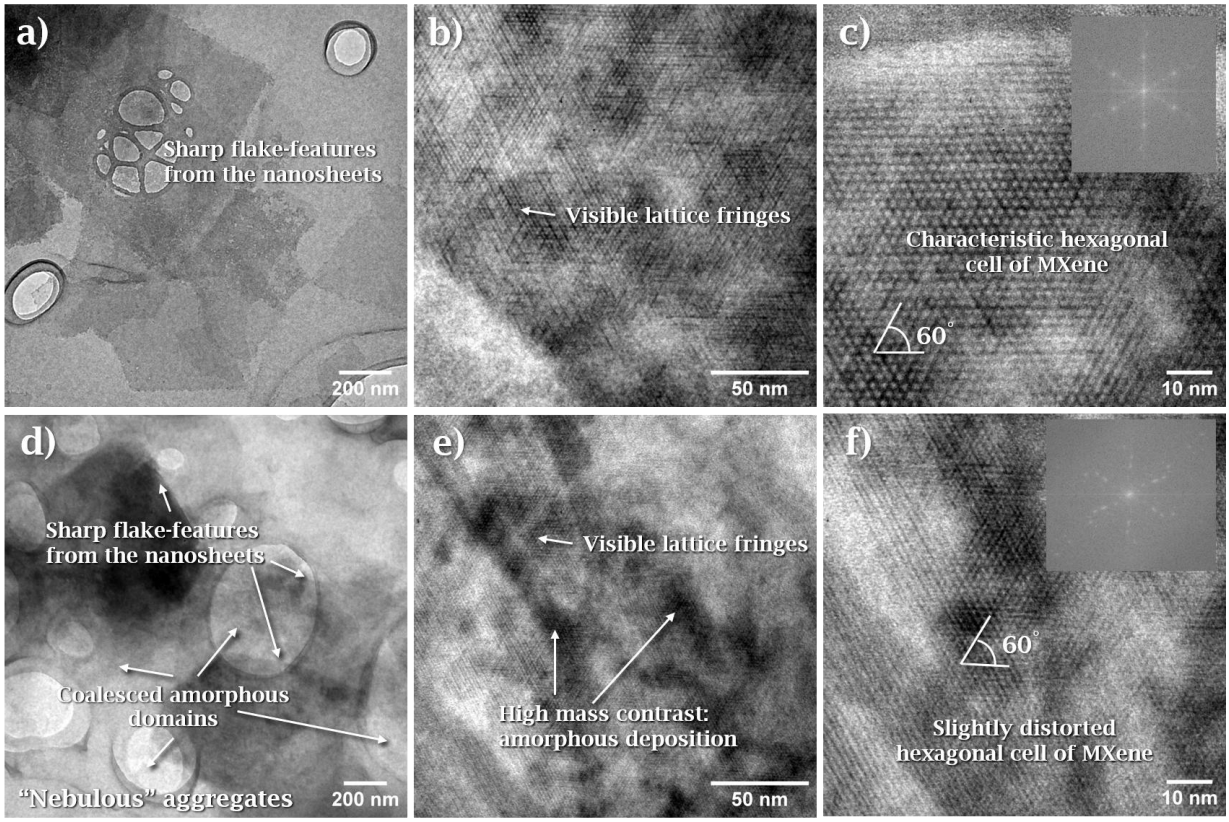

Figure 3.6 *TEM and HR-TEM image comparison of (a-c) bare MXene nanosheets and (d-f) 15b-MXene composites.*

This fluffy morphology needed a scientific and elegant name, and the phrase "nebulous aggregates" captures the appearance perfectly. These were observed in the high resolution-

TEM (HR-TEM) studies, where the flakes were seen covered by the characteristic cotton-like morphology (**Figure 3.6d**) of the oligomer-**15b**. The flakes showed numerous dark spots, most likely arising from the gaps left by the oligomer (high mass contrast, **Figure 3.6e, f** and **Figure 3.8**), resulting in highly diffused encapsulation. However, the hexagonal lattice fringes were very obvious and very visible in the composite sample.

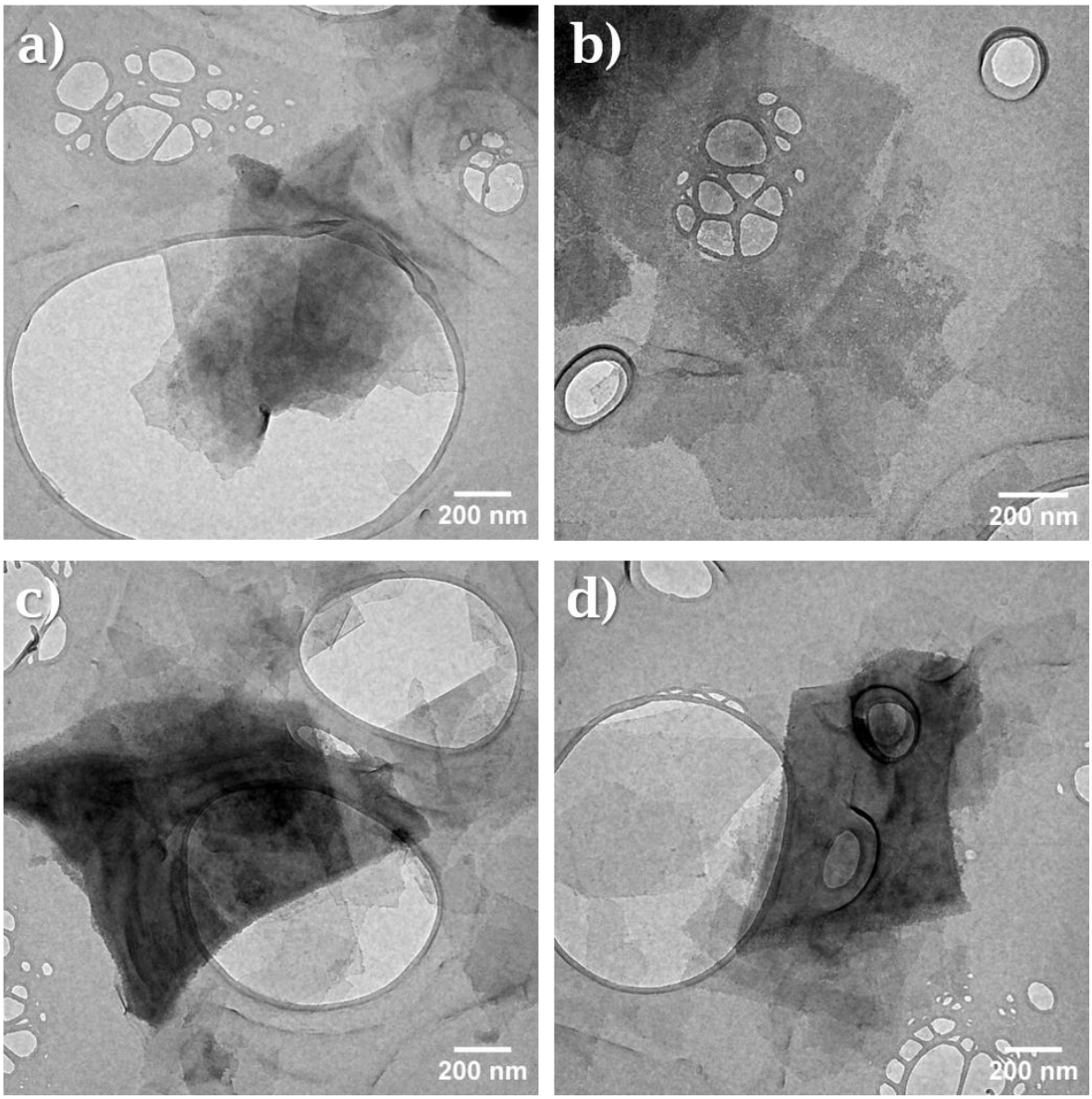

Figure 3.7 *TEM images of bare MXene (a-d) with clean and almost transparent flakes.*

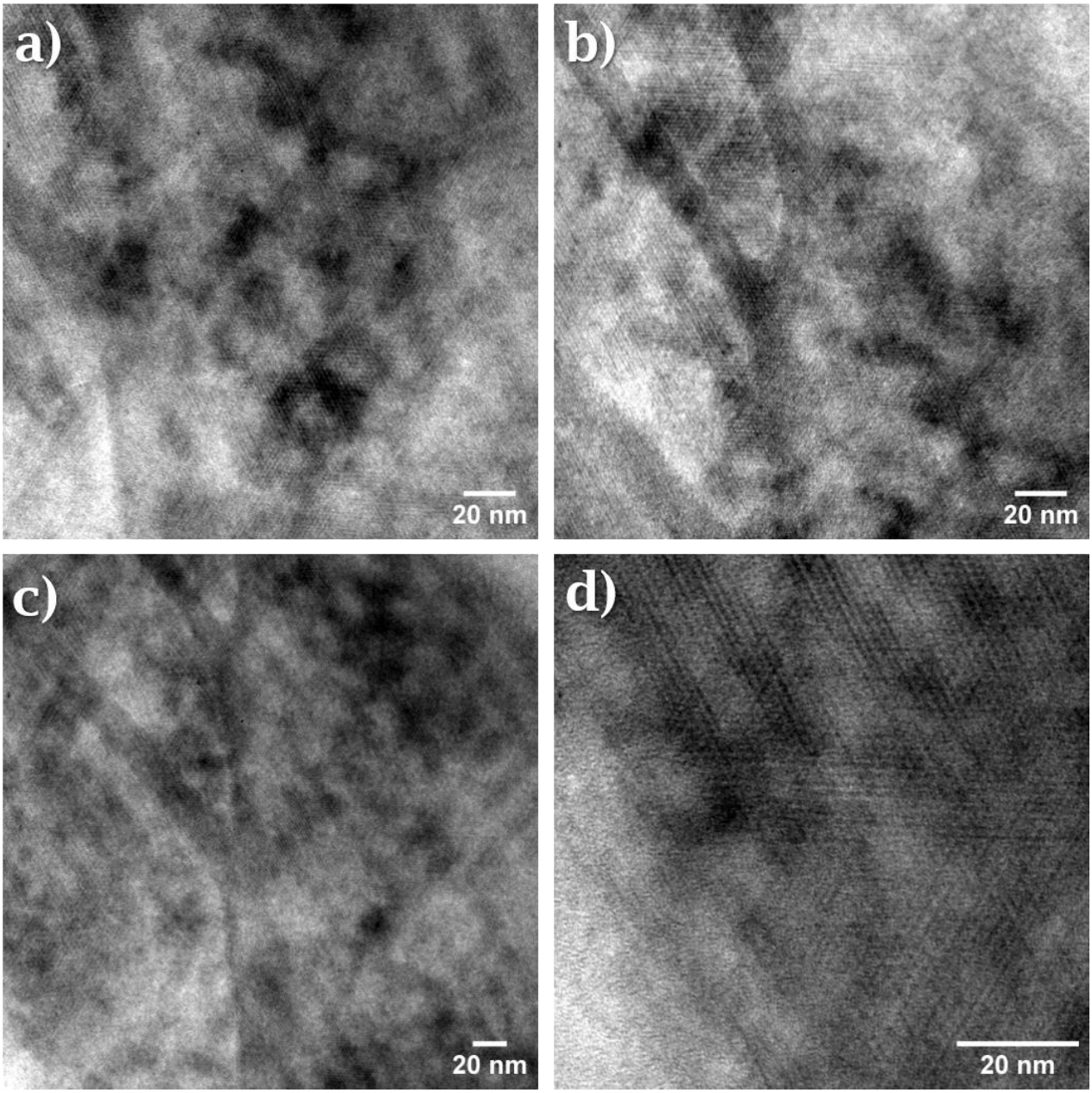

Figure 3.8 *HR-TEM images of* ***15b****-MXene composites (a-d) with dark spots indicating oligomer-****15b*** *onto the MXene sheets.*

The images contained considerably more information than was initially apparent as exemplified by the lattice fringes obtained through high resolution images. A fast Fourier transform (FFT) was applied to the images and highlighted the points directly related to the lattice planes (**Figure 3.9**). Inverse FFT of those points gave back the reconstructed lattice planes. This highlighted the distortion of the lattice planes of the MXene flakes in the composite sample, and nothing of that sort was seen in the bare MXene flakes.

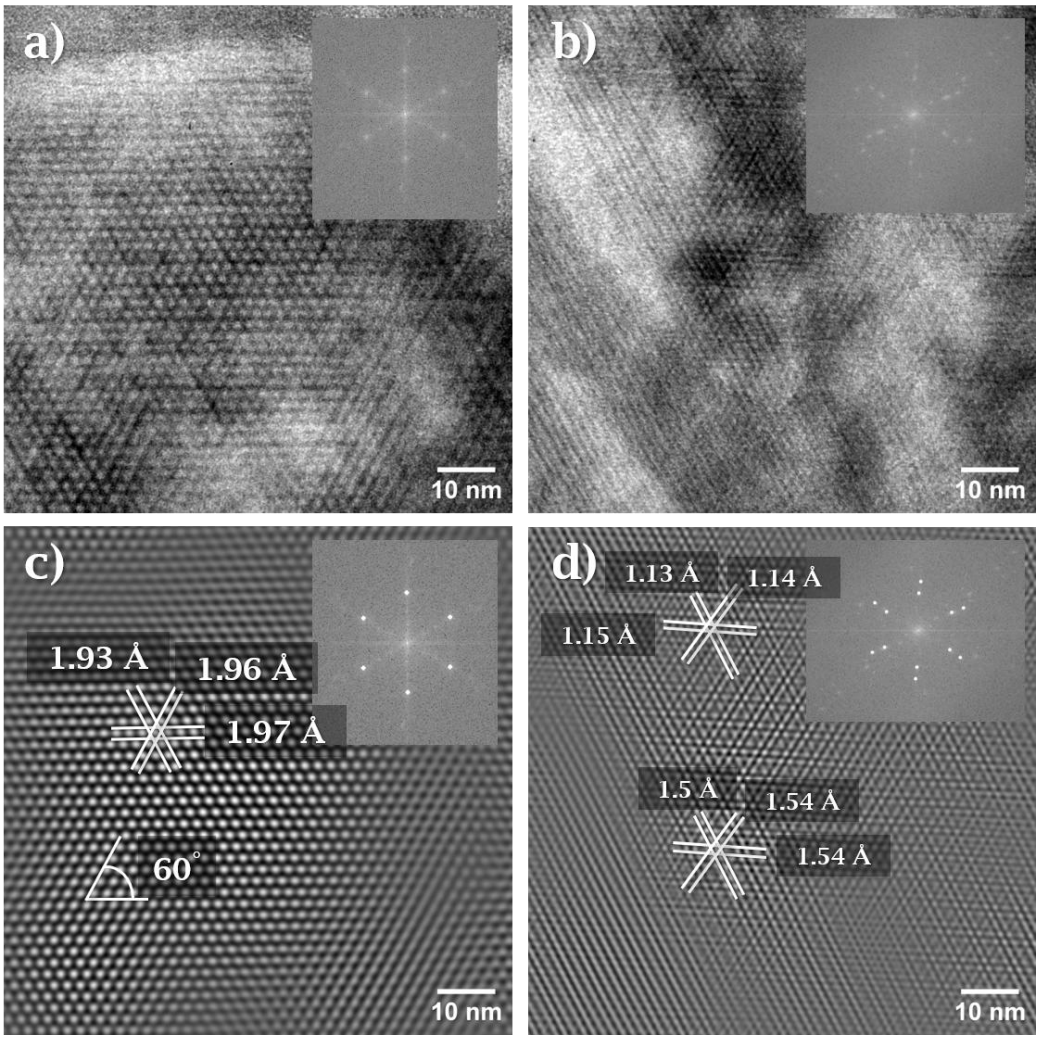

Figure 3.9 *Comparison of the HR-TEM images and its FFT images of (a) MXene and (b) composite. Notice, the distortion could clearly be seen in the FFT of the composite. Below are the reconstructed lattice fringes of (c) MXene and (d) the composite.*

3.3.3 Characterisation of the Composites

Consistent with the previous chapter, XPS studies were employed to gain further insight into the formation of the composites and the extent of their degradation under ambient conditions. Survey spectra (**Figure 3.10**) contained all the main peaks like Ti, C, F, O etc. except N for the pure MXene samples, whereas the composite material contained the N-signals as well. This is a direct proof of the composite formation. Unlike the previous chapter, acetonitrile wasn't involved in the composite formation step, hence, the origin of the N1s signals must have been the oligomer-**15b**.

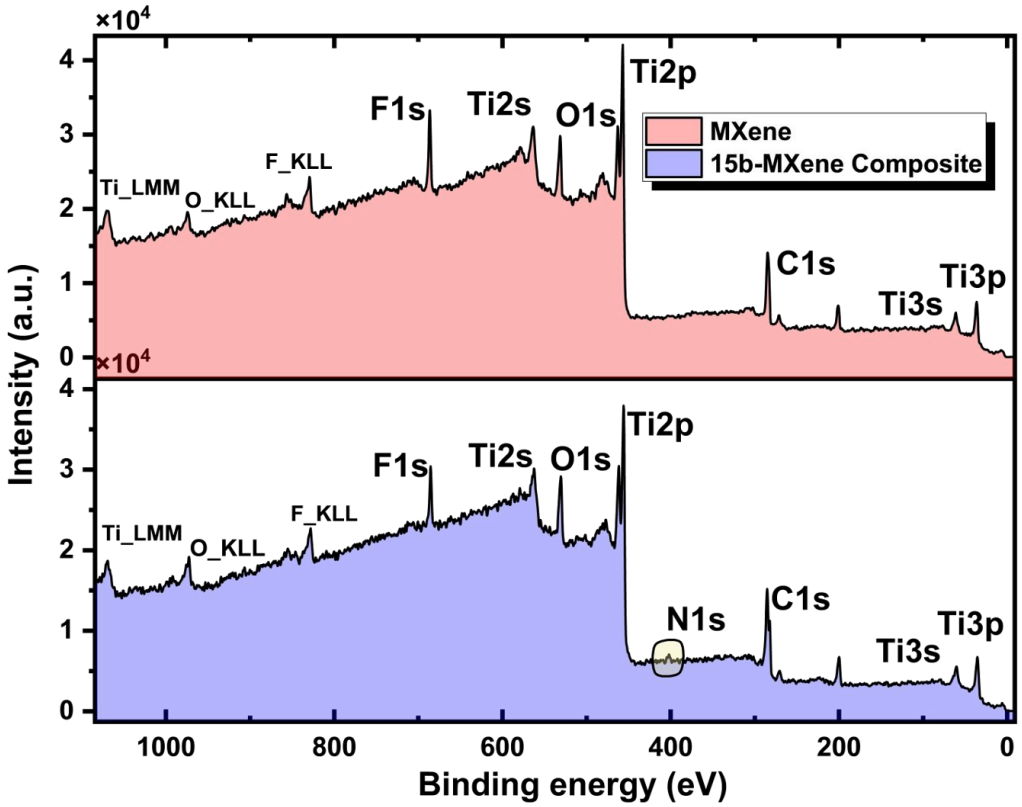

Figure 3.10 *Survey spectra comparison of MXene and the* ***15b****-MXene composite highlighting the presence of nitrogen.*

The $Ti2p_{3/2}$ peaks were deconvoluted to components assigned to Ti–C, Ti^{2+}, Ti^{3+}, Ti–O species and Ti–F species components and the peak positions are given in the **Table 3.1**. It is noteworthy that the deconvolution of the C1s spectrum for the composite was never complete without including a component at 288.22 eV attributed to C=N signal (**Figure 3.11**, **Table 3.2**). This is another signal that confirms the presence of the oligomer in the composite.

The TiO_2 component in the O1s spectra (**Figure 3.12a, c**) suggests an initial oxidation of the flakes. This is consistent with the Ti2p signals where I saw some degree of oxidation. Upon a close look at the N1s spectrum for the composites we can see the typical viologen signatures with N^+ signal at 402.02 eV and the $N^{\bullet+}$ signal at 399.54 eV (**Table 3.4**, **Figure 3.12**) as discussed in chapter 2. No N1s signals were seen in case for the pure nanoflakes. The F1s signals indicated the surface groups present in both the pure MXene and the composite (**Table 3.3**).

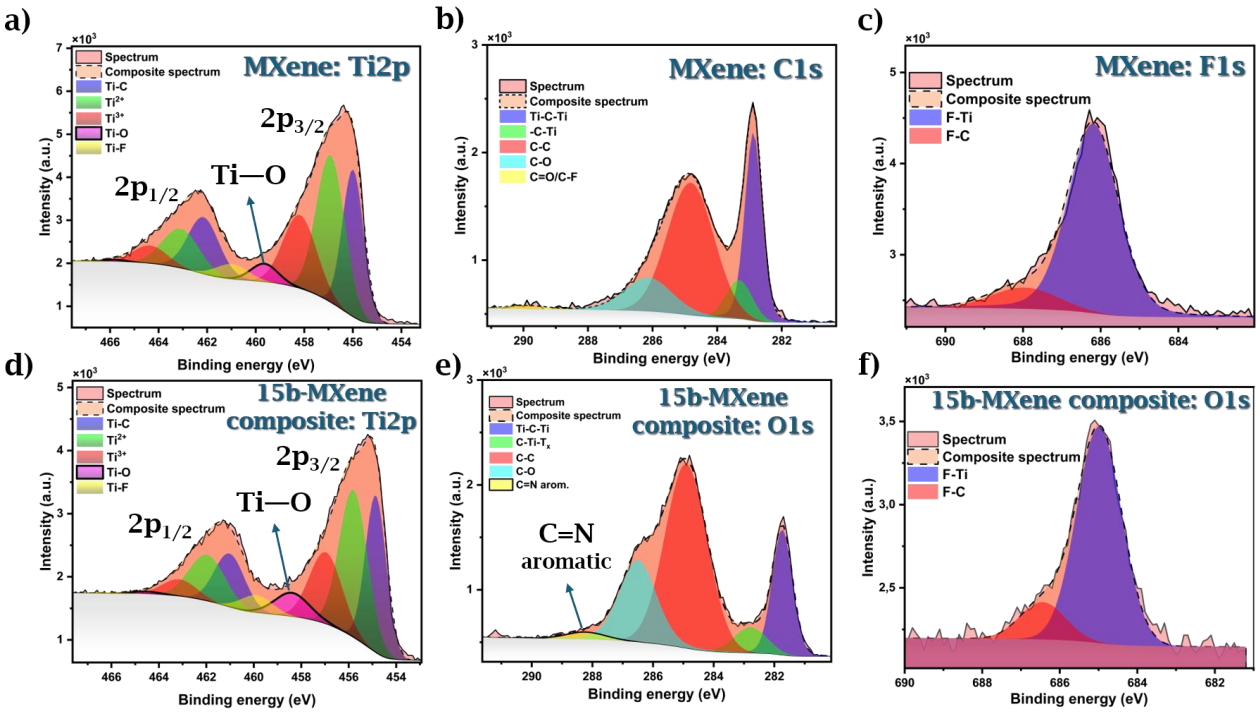

Figure 3.11 *XPS comparison of the high-resolution spectra, (a) Ti2p, (b) C1s and (c) F1s of MXene and (d) Ti2p, (e) C1s and (f) F1s of the composite. The C=N in C1s is an indication of the composite formation.*

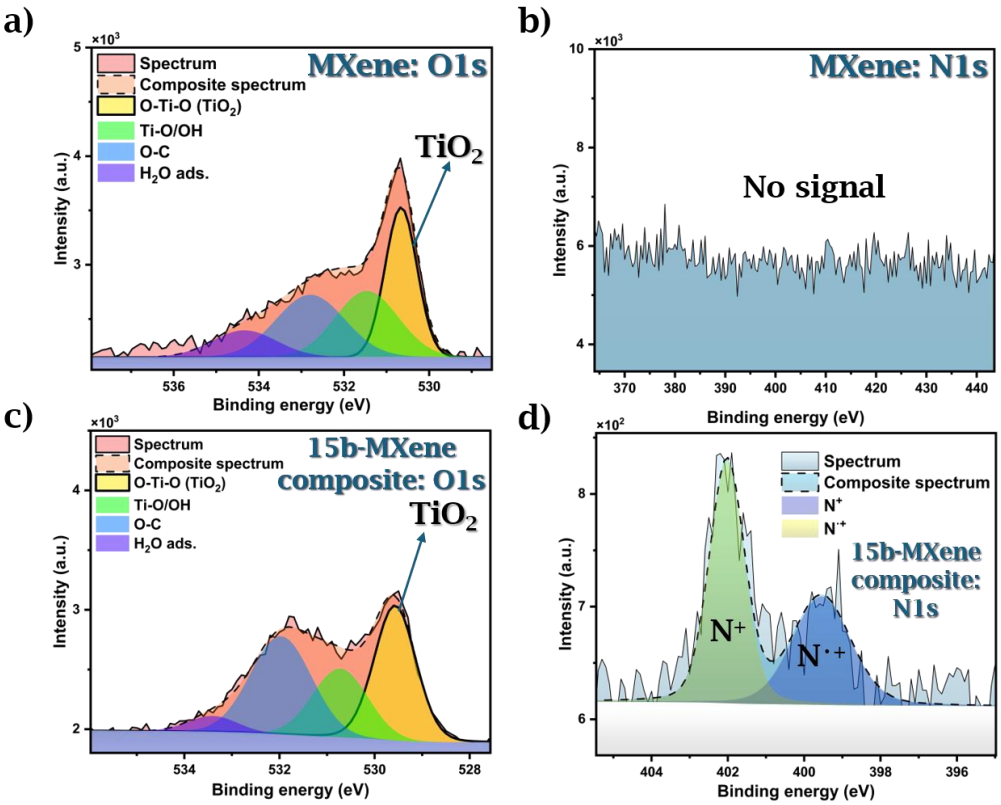

Figure 3.12 *XPS comparison of the high-resolution spectra, (a) O1s of MXene and (c) O1s and (d) N1s of the composite. No N1s signal in MXene (b) suggest the composite formation in (d).*

Table 3.1 *Ti2p binding energies of MXene and* ***15b****-MXene composite in XPS measurements.*

Binding energy	**Spin-orbit component**	**Ti–C [eV]**	**Ti^{2+} [eV]**	**Ti^{3+} [eV]**	**Ti–O [eV]**	**Ti–F [eV]**
Pure MXene$^{(P)}$	$2p_{3/2}$ $2p_{1/2}$	455.97 462.14	456.91 463.08	458.17 464.34	459.64 465.81	460.98 467.15
15b-MXene Composite$^{(P)}$	$2p_{3/2}$ $2p_{1/2}$	454.84 461.01	455.79 461.96	456.95 463.12	458.39 464.56	459.89 466.06

$^{(P)}$ Protected

Table 3.2 *C1s binding energies of MXene and* ***15b****-MXene composite in XPS measurements.*

Binding energy	**Ti–C–Ti [eV]**	**–C–Ti [eV]**	**C–C [eV]**	**C–O [eV]**	**C=O/C–F [eV]**	**C=N [eV]**
Pure MXene$^{(P)}$	282.87	283.31	284.81	286.12	289.92	—
15b-MXene Composite$^{(P)}$	281.72	282.77	284.90	286.49	—	**288.22**

$^{(P)}$ Protected

Table 3.3 *F1s binding energies of MXene and* ***15b****-MXene composite in XPS measurements.*

Binding energy	**F–Ti [eV]**	**F–C [eV]**
Pure MXene$^{(P)}$	686.18	687.96
15b-MXene Composite$^{(P)}$	684.98	686.44

$^{(P)}$ Protected

Table 3.4 *N1s binding energies of MXene and the 15b-MXene composite in XPS measurements.*

Binding energy	**$N^{\bullet+}$ [eV]**	**N^{+} [eV]**
Pure MXene$^{(P)}$	—	—
15b-MXene composite$^{(P)}$	399.54	402.02

$^{(P)}$ Protected

3.3.4 Ambient stability studies of the composites

The samples were subjected to UV-Vis titration and checked the first signs of the ambient degradation. Obviously, the water would evaporate if cuvette was left open for 6 days! So,

the air inside the cuvette headspace was repeatedly replaced with fresh air each day for 6 days and shaken vigorously to increase the fresh air dissolved in the water. This was repeated for both the pure MXene and the composite. The peak near 260 nm in the UV-Vis spectrum progressively increased over time for the pure MXene attributed to the anatase TiO_2 formation. The reason for the decrease in absorbance at λmax over time could not be established; however, rearrangement of the aggregates during the shaking process might have caused the hypochromic shift (**Figure 3.13**).

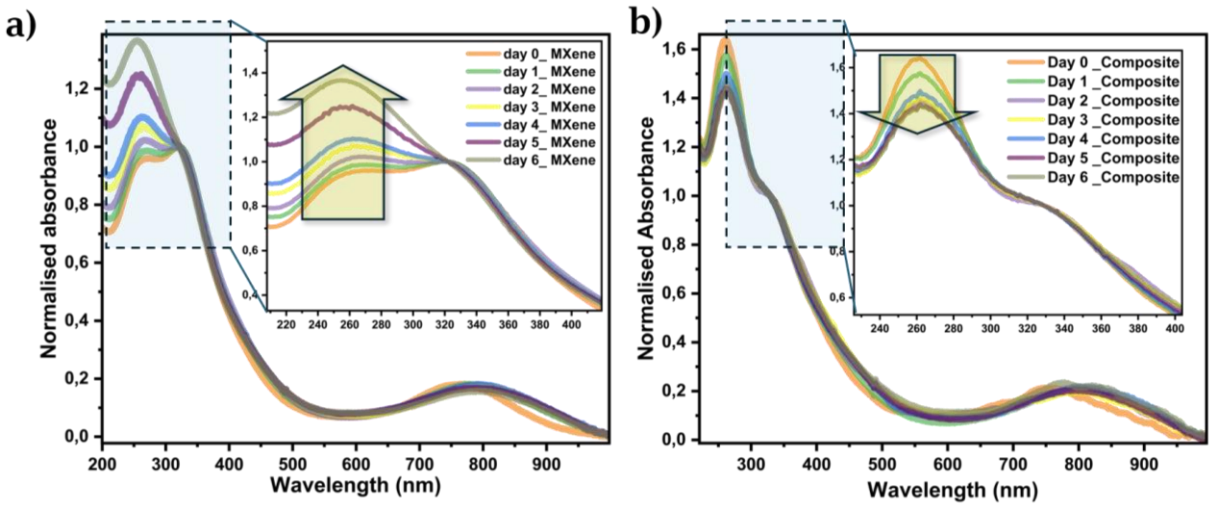

Figure 3.13 *Observing ambient degradation in solution phase using UV-Vis studies, (a) changes in pure MXene absorption and (b) changes in composite absorption for 6 days,*

Raman spectra of MXene could reveal a lot about the lattice and its changes during the degradation process. Raman spectra for pure MXene contain the skeletal or flake region (100–200 cm^{-1}), the surface group region (T_x region, 200–500 cm^{-1}) and the carbon region (500–800 cm^{-1}). They correspond to group vibration of carbon and two titanium layers, vibration of the surface groups and collective in-plane and out-of-plane vibrations of the carbon atoms, respectively.[87-89] The two bands at 263 and 419 cm^{-1} (Figure) correspond to the E_g modes of the surface groups attached to Ti, and the band at 608 cm^{-1} is associated with the E_g vibrational modes of C. As per the MXene exfoliation process, conducting the reaction at 65 °C was reported to have higher amount of −OH compared to −F, the peaks for the surface groups were different compared with our group's previous report,[90] whereas the E_g vibrational modes for the C atoms were similar. The anatase form of TiO_2 appears at 153 cm^{-1} which is well documented in literature and the intensity was found to be increased (**Figure 3.14a**) for the pure MXene nanosheets after being exposed to ambient conditions for 6 days, whereas minimal change in TiO_2 content was observed in case of the **15b**-MXene composite (**Figure 3.14b**).

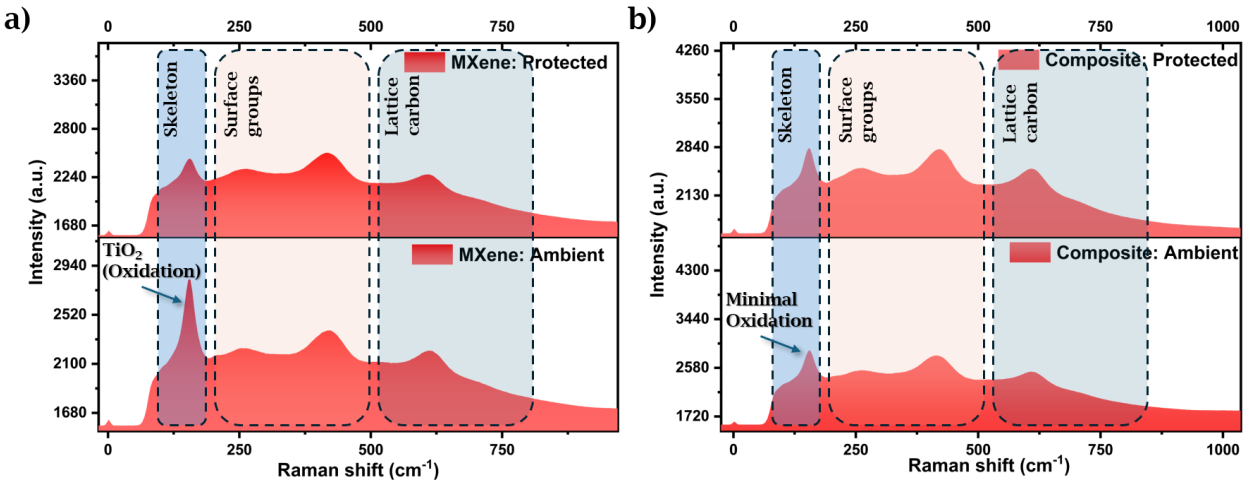

Figure 3.14 *Observing ambient degradation in solid phase by looking at Raman shifts, (a) pure MXene with a huge change in TiO_2 content and (b) composite with no significant change in the skeletal region of MXenes involved after 6 days of ambient exposure.*

The degradation of both the MXene and the composite was assessed by XPS through comparison of samples exposed to ambient conditions with their counterparts stored under inert conditions. The Ti–O contribution in the Ti2p region is considered a clear indicator of oxidation in literature and was therefore monitored closely. The signals associated with O–Ti species in the O1s region and Ti–C species in the C1s region may also reflect degradation and is particularly relevant as progressive oxidation leads to the cleavage of Ti–C bonds and the preferential formation of titanium oxides. However, their use for quantification is less reliable due to the small peak separations and the resulting uncertainties in spectral deconvolution. Consequently, the Ti2p spectra being reliable, was used to quantify the oxidation extent, although both the Ti2p and O1s regions provided evidence of degradation.

The calculation from all the replications showed that the average Ti–O content increasement for the pure MXene was around 131% (**Figure 3.15a, b**), whereas the same for the composite on an average was found to be very low (~1%, **Figure 3.15c, d**). The calculation method was the same as the one followed in chapter 2.

The peaks from the deconvolution of the Ti2p and O1s for the samples studied at ambient conditions are given in the upcoming tables in this chapter.

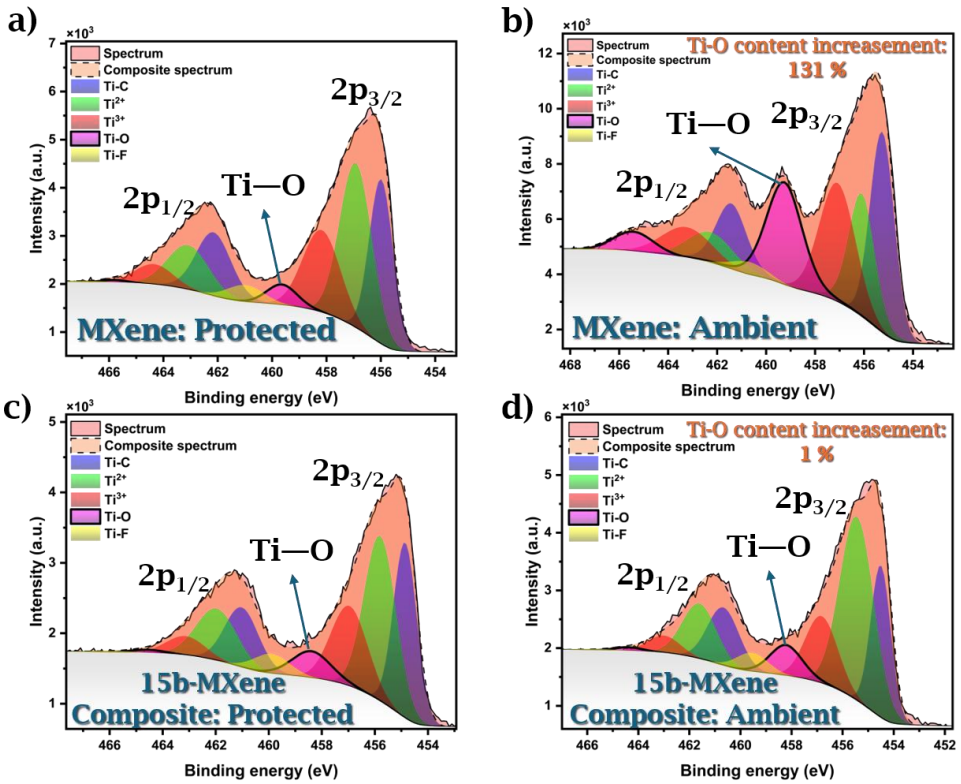

Figure 3.15 *High resolution Ti2p XPS spectra showing oxidation extent increasement over 6 days; (a) pure MXene in inert conditions, (b) pure MXene in ambient conditions, (c)* ***15b****-MXene composites in inert conditions and (d)* ***15b****-MXene composite in ambient conditions.*

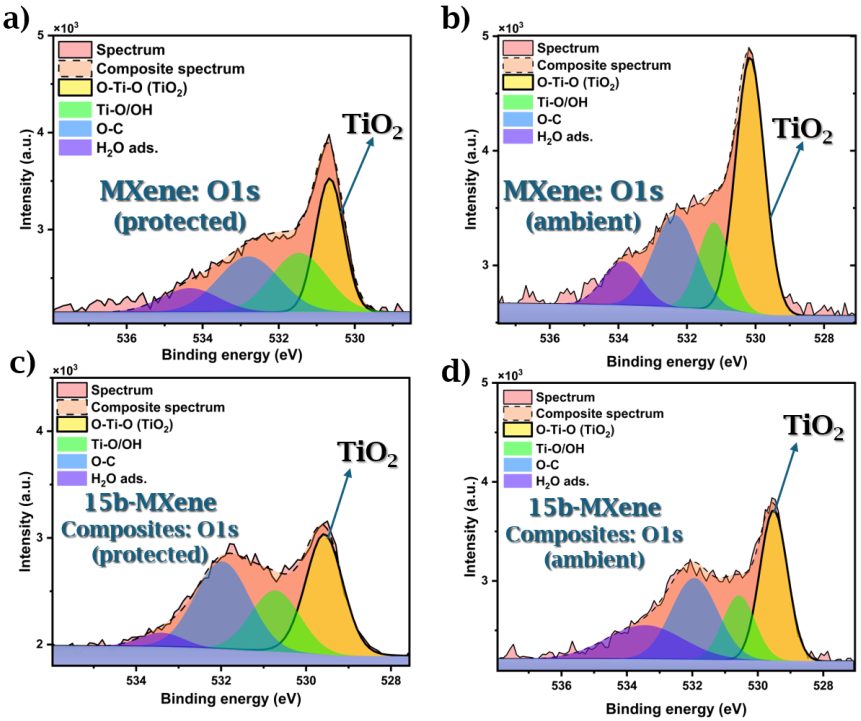

Figure 3.16 *High resolution O1s XPS spectra showing increasement in TiO_2 content over 6 days(a) pure MXene in inert conditions, (b) pure MXene in ambient conditions, (c)* ***15b****-MXene composites in inert conditions and (d)* ***15b****-MXene composite in ambient conditions. It is to be noted that this is purely a qualitative estimation.*

Table 3.5 *Ti2p binding energies of MXene and* ***15b****-MXene composite kept in ambient conditions in XPS measurements.*

Binding energy	**Spin-orbit component**	**Ti–C [eV]**	**Ti^{2+} [eV]**	**Ti^{3+} [eV]**	**Ti–O [eV]**	**Ti–F [eV]**
Pure MXene[(A)]	$2p_{3/2}$ $2p_{1/2}$	455.24 461.41	456.08 462.25	457.07 463.24	459.26 465.43	460.68 466.85
15b-MXene Composite[(A)]	$2p_{3/2}$ $2p_{1/2}$	454.49 460.66	455.43 461.60	456.81 462.98	458.21 464.38	459.53 465.70

[(A)] Ambient

Table 3.6 *O1s binding energies of MXene and* ***15b****-MXene composite in XPS measurements.*

Binding energy	**TiO_2 [eV]**	**Ti–O/OH [eV]**	**O–C [eV]**	**H_2O (ads.) [eV]**
Pure MXene[(P)]	530.66	531.46	532.78	534.33
Pure MXene[(A)]	530.16	531.20	532.34	533.87
15b-MXene Composite[(P)]	529.57	530.72	531.96	533.40
15b-MXene Composite[(A)]	529.52	530.57	531.93	533.45

[(P)] Protected, [(A)] Ambient

3.4 Understanding the results

The experiment was repeated three times (**Figure 3.17**) and the results were reproducible. The negative values for oxidation increasement in experiment 1 and 2 are purely statistical and do not imply reversal of oxidation process. The noncovalent approach with the system that didn't work with the BPNSs but showed promising results for increasing the ambient stability of MXenes in the solid phase.

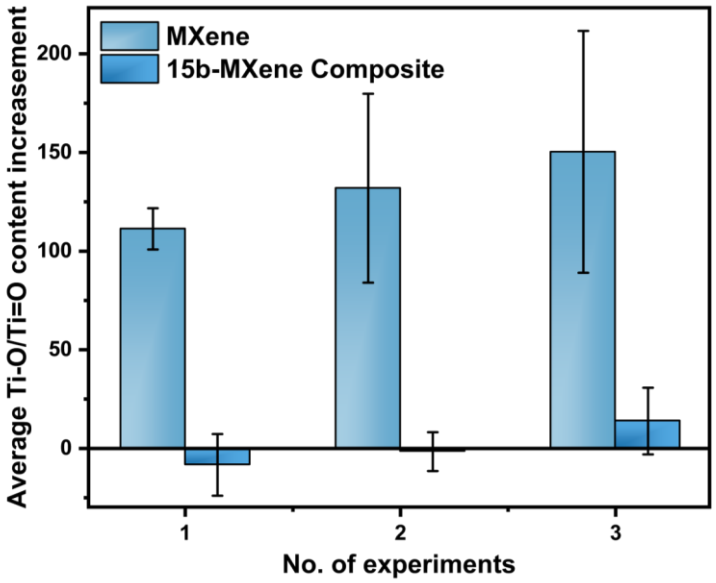

Figure 3.17 *Comparison of the oxidation between pure MXene and the composite in various iterations.*

Thus far, the experimental results and subsequent analyses have consistently indicated favourable interactions between the MXene and the oligomer. However, the extent to which these observations are supported by existing theoretical

frameworks, remains to be examined. Furthermore, it is necessary to assess whether the current theory is sufficient to explain all aspects of the experimental findings. These considerations are explored in greater detail in the following section.

3.5 DFT insights

In a computational setting, the physical system is very big, on one hand it consists of a large 2D slab of MXene (purely $Ti_3C_2F_2$, no hydroxyl groups), and on the other hand it is composed of an oligomer with repeating units increasing its complexity further. Also, while defining a composite system in computational modelling the bigger the molecules are, the 2D slab also has to be made bigger. This requires access to great computing powers with which comes great responsibilities!

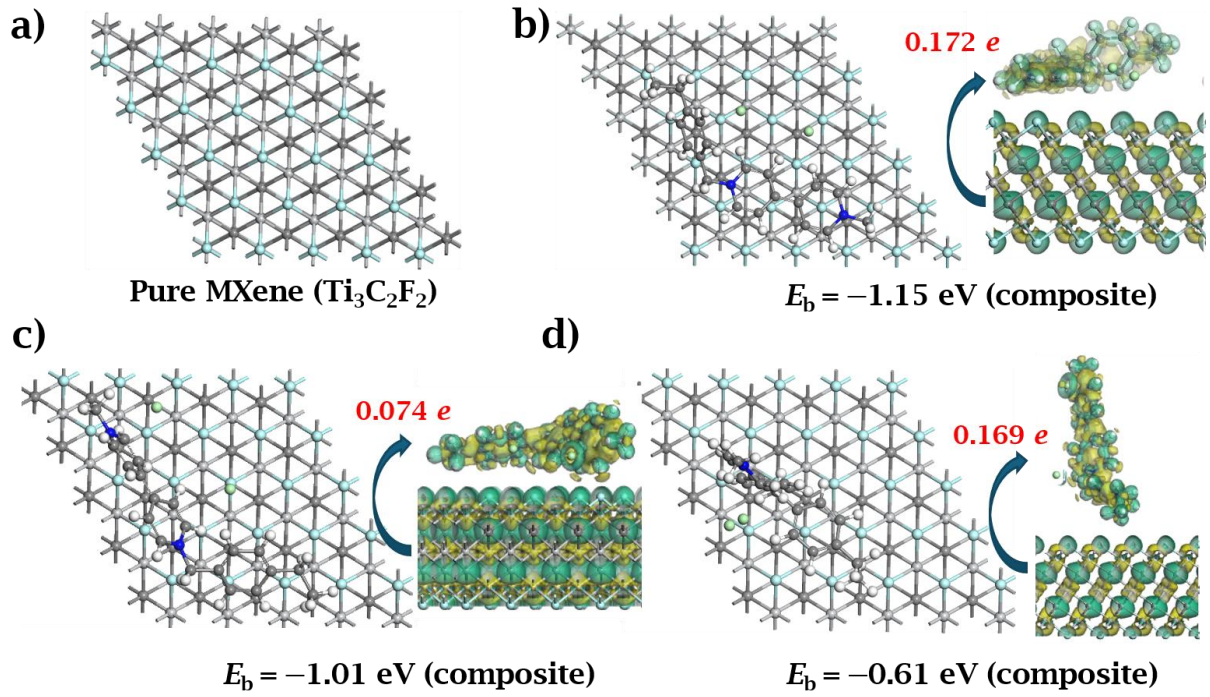

Figure 3.18 *Binding energy calculations of the oligomer-**15b** onto a 2D MXene slab, (a, b) in parallel orientation and (d) in perpendicular orientation. The pure MXene slab used for the calculations is shown in (a).*

Therefore, an approximate model was employed in which the oligomer-**15b** was represented by a single monomeric unit (**14b**), with the alkene functionality substituted by the corresponding alkane. This approach was adopted in collaboration with the *theoretical modelling team* to simplify the calculations while preserving the essential characteristics of the system. Binding interactions were then evaluated for a range of monomer orientations. If favourable binding was observed consistently across these configurations, favourable interactions between oligomer-**15b** and the MXene surface could reasonably be anticipated.

Our collaborators calculated the binding energy (E_b) using this formula,

$$E_b = E_{x+y} - E_{mono} - E_{MXene}$$

Where E_{x+y} is the total energy of the binding between the alkane-terminated monomer unit and MXene, E_{mono} is the energy of only the alkane-terminated monomer unit, and E_{MXene} is the energy of the MXene.

The calculation with the monomer and MXene suggested an effective binding with negative binding energies in different orientations. When the molecular plane of the monomer was parallel to the 2D slab, the binding energy was less than −1 eV (**Figure 3.18**) whereas the orientation of the monomer plane perpendicular to the slab had a binding energy of −0.61 eV. This as we hypothesised already, might be extrapolated to the composite with oligomer-**15b** and MXene.

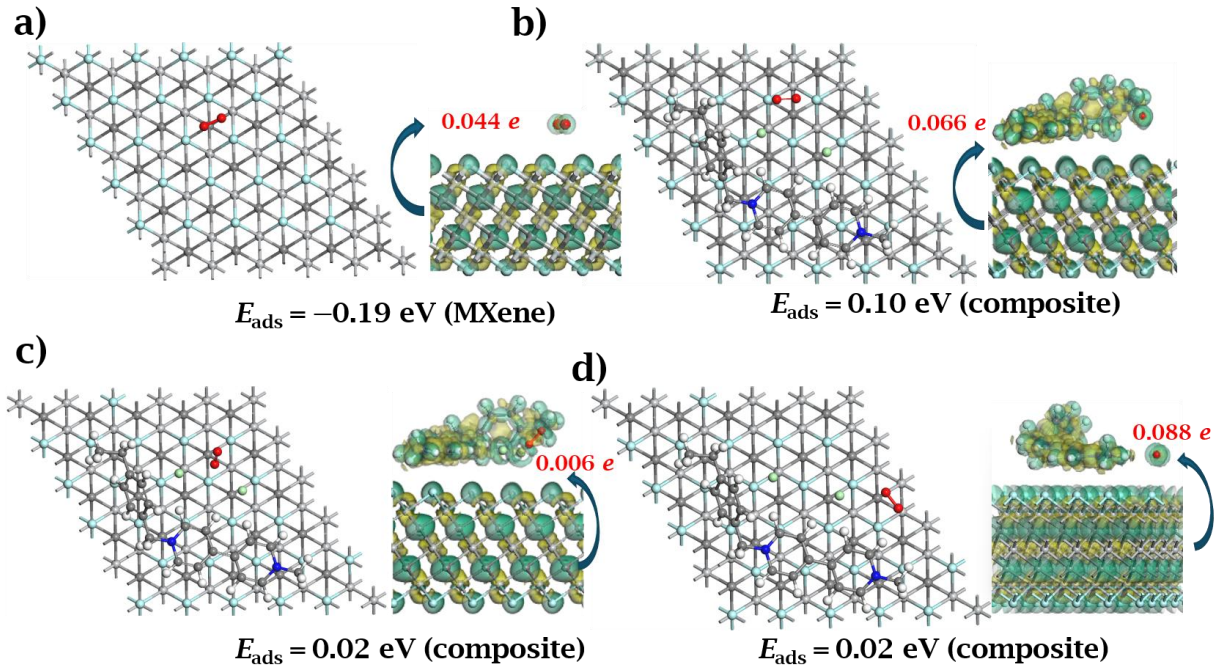

Figure 3.19 *Calculated adsorption energy of O_2 molecule onto (a) pure MXene, (b–d) onto the composite with the monomer unit where the position of the O_2 is being varied.*

They also calculated the adsorption energy of one oxygen molecule onto the MXene sheet, and the adsorption energy of an oxygen molecule onto the slab was around −0.19 eV. This favourable adsorption might be the first step of the chemisorption leading to oxidation.

O_2 adsorption energy (E_{ads}) was calculated by the following formula,

$$\mathbf{E_{ads} = E_{total} - E_{Oxygen} - E_{x+y}}$$

where the total energy of the system is E_{total} after introducing O_2, and the energy of the O_2 molecule is E_{Oxygen}.

Then they looked into the oxygen adsorption onto the slab while the monomer unit was attached (the orientation chosen was with the lowest binding energy, i.e., most favourable). The position of the oxygen was varied onto the slab with no change in the composite. The result showed positive adsorption energy in all the cases, or in other words, unfavourable binding for the oxygen molecule onto the composite sample (**Figure 3.19**).

3.6 Coalescing behaviour of the oligomer-15

While the interactions of oligomer-**15b** with MXene have been discussed extensively, the properties of the oligomer-**15b** haven't been discussed before. The GPC data (Appendix: Experimental Section) showed the presence of two different populations in the oligomer one with ~3 units and one with ~11 units (predominant). The Zeta potential experiment includes the Zeta potential of the pure oligomer, which was around +14 mV, clearly showing the cationic nature of the oligomer.

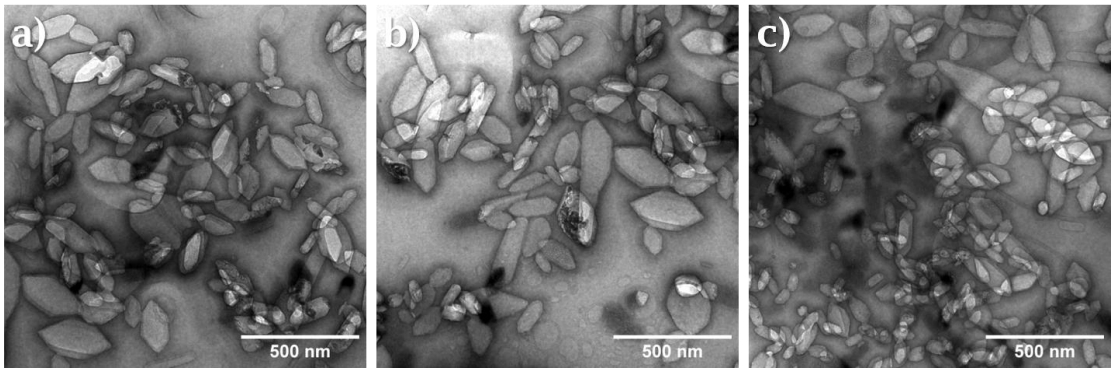

Figure 3.20 *Oligomer-**15b** as seen under TEM.*

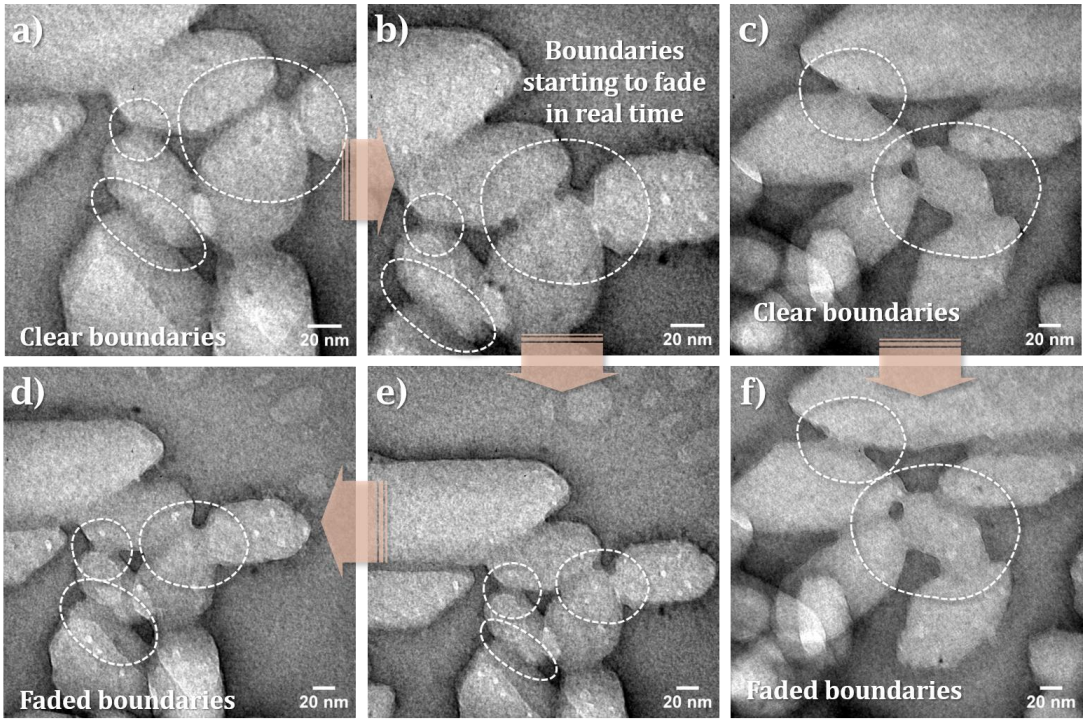

Figure 3.21 *Coalescing behaviour of 15b, (a→b→e→d) fading boundaries of the particles (c→f) another example of the same.*

However, the morphological studies in TEM (**Figure 3.20**) and HRTEM (**Figure 3.21**) studies reveals much more about the pure oligomer. The oligomer was first dissolved in small amount of good solvent (water) and precipitated out by adding an excess amount bad solvent (acetone). Since this process is very fast, the solid particles formed are very small,

as could be seen in the TEM images in **Figure 3.20**. Interestingly, in the HRTEM images it was observed that the oligomers merged together, very similar to oil droplets coalescing in an emulsion. Such assembly could be driven by the tendency of the hydrophobic backbone segments to minimise their exposure to the solvent, while being modulated by electrostatic interactions arising from the charged functionalities and their associated counterions.

Some clarification is needed at this point. Although the particles appeared to coalesce, this behaviour should not be regarded as a hydrophobic interaction. The phenomenon was observed under vacuum, where the solvent-mediated entropy gains ($\Delta S > 0$) responsible for hydrophobic association cannot occur. When only the oligomer particles are considered, coalescence reduces the number of accessible configurations and therefore lowers the entropy of the system. Nevertheless, the process occurs spontaneously, indicating the presence of a favourable thermodynamic driving force. In this case, the behaviour is more reasonably explained by a reduction in surface free energy, which can be expressed as

$$\Delta G_{\text{surface}} = \gamma \Delta A$$

where γ is the surface energy and ΔA is the change in surface area. As neighbouring particles merge, the total exposed area decreases, lowering the surface free energy of the system. This reduction provides the driving force for the observed coalescence. Thus, while the merging behaviour resembles hydrophobic association, the underlying mechanism is fundamentally different and arises from the tendency of the system to minimise its surface energy.

These effects may also contribute to the formation of the composite between **15b** and MXene, whereas they appear to be considerably less pronounced for BPNSs. These differences and trends are discussed in greater detail in the next chapter. Furthermore, this stabilisation strategy represents a potentially significant advance in MXene research, demonstrating that the combination of electrostatic interactions and hydrophobic encapsulation can yield composites with substantially improved resistance to oxidation. Such enhanced stability might open the door to more reliable MXene integration in energy storage systems, catalytic platforms, and emerging optoelectronic technologies where long-term performance is essential.

4. Mechanism of the Interactions

4.1 Types of interactions

Universal van der Waals forces act as the baseline attraction between all molecules and two-dimensional surfaces. These non-specific dispersion forces depend directly on the total contact area and the distance between the atoms. In pristine 2D materials like graphene or transition metal dichalcogenides, these weak physical forces allow non-polar polymer chains to adhere to the basal plane. When aromatic molecules or conjugated polymers are involved, this force manifests as specialised π-π stacking. The aromatic rings align completely flat against the electron-dense π-cloud of the 2D sheet. This spatial alignment maximizes the physical contact area without altering the target crystal structure.

Electrostatic interactions govern the assembly when dealing with charged molecules and functionalised or defect-rich 2D materials. Materials like graphene oxide or liquid-exfoliated MXenes carry permanent negative surface charges due to their localised oxygen or hydroxyl groups. These charged surfaces exert long-range Coulombic attraction on oppositely charged polyelectrolytes, ionic surfactants, and metal cations. Similarly, dense hydrogen-bonding networks form between polar polymer chains, like polyvinyl alcohol, and the oxygenated functional groups on the 2D sheet. These localised polar bindings are highly directional and significantly stronger than basic dispersion forces.

Charge transfer interactions involve a partial shift of electronic charge between the 2D lattice and the adsorbed chemical species. In this mechanism, one component acts as an electron donor while the other serves as an electron acceptor. For example, strong electron-withdrawing molecules can draw density directly out of a pristine graphene sheet, acting as p-type dopants. Conversely, electron-donating molecules inject carriers into the 2D conduction band. This physical exchange of charge modifies the Fermi level and tunes the carrier concentration of the material. Crucially, this electronic tuning occurs without forming any permanent covalent bonds or structural lattice defects.

4.2 What controls binding

Surface Properties

The physical and chemical states of the 2D surface directly dictate the strength and nature of the non-covalent interface. Surface cleanliness is critical, as ambient contaminants and airborne hydrocarbons quickly mask the surface and lower its binding affinity. The presence of atomic defects, grain boundaries, and step edges also alters local reactivity by creating highly active site regions. Furthermore, the chemical composition of the surface determines which interaction dominates. Pristine, uncharged basal planes favour pure van der Waals and π-π stacking, whereas chemically oxidised sheets shift the binding mechanism toward electrostatic and hydrogen bonding.

Molecule Properties

The intrinsic structural and chemical traits of the adsorbing molecule or polymer govern how effectively it couples with the 2D host. Molecular conformation and overall chain length determine the total number of physical contact points along the 2D surface. Larger

macromolecules or longer polymer chains achieve greater overall binding stability through collective, multi-point contacts. The presence of specific functional groups, such as aromatic rings, polar groups, or charged groups, directly dictates which primary interactions are activated. Additionally, the conformational flexibility of the molecule controls how easily it can flatten its backbone to maximize contact with the 2D sheet.

4.3 BPNSs vs MXenes

Divergent Non-Covalent Binding Pathways

The variance in non-covalent behaviour between the two studies 2D materials, BPNS and MXene stems entirely from their distinct surface chemistry and electronic profiles. MXene sheets inherently display a highly polar surface due to native oxygen, hydroxyl, and fluorine termination groups acquired during chemical etching. These polar terminations force the interface to prioritise long-range electrostatic Coulombic interactions and dense hydrogen bonding networks. Consequently, MXenes pair preferentially with hydrophilic polymers like polyvinyl alcohol or positively charged polyelectrolytes through ionic bridging and hydration shell displacement. Conversely, black phosphorus features a highly anisotropic, puckered atomic surface entirely devoid of native ionic terminations or polar groups. Because BPNSs lack such charged functionalities, their interfacial assembly is expected to be dominated by short-range van der Waals forces and local orbital-overlap interactions, rather than long-range electrostatic attractions.

Electronic and Charge Transfer Disparities

The electronic disparity between the materials dictates how they participate in non-covalent charge transfer interactions. Owing to its metallic character and high electronic density of states near the Fermi level, adsorption on MXene surfaces is often accompanied by charge redistribution between the adsorbate and the substrate. The resulting charge transfer is dictated primarily by the end-groups of the adsorbing molecule, altering the work function without triggering any electronic phase transition (metallic → semiconducting, semiconducting → metallic, insulating → conducting, etc.). In contrast, black phosphorus behaves as a semiconductor with a highly tuneable direct band gap. Its lone pairs of electrons project outward from the puckered phosphorus atoms, making the surface exceptionally electron-dense and chemically reactive. When electron-deficient polymers or strong electron-withdrawing molecules like TCNQ adsorb onto the sheet, they trigger a dramatic p-type doping process via direct physical charge abstraction. This interfacial charge transfer fundamentally changes the carrier concentration of the semiconductor.

Structural Degradation and Passivation Mechanics

Both materials suffer from severe ambient instability, but the chemical pathways driving their oxidation operate through fundamentally distinct mechanisms. Black phosphorus degrades via a purely topochemical photo-oxidation process. Its exposed surface lone pairs interact directly with ambient oxygen under light, generating highly reactive oxygen species that rapidly convert the elemental phosphorus lattice into hydrophilic phosphoric acid droplets. In contrast, MXene oxidation relies heavily on a water-driven nucleophilic attack that targets vulnerable, uncoordinated titanium surface atoms and sheet edges. Dissolved oxygen and water molecules break down the internal titanium-carbon bonds, forcing a

phase separation that turns the conductive carbide lattice into insulating titanium dioxide (TiO_2) nanocrystals while releasing carbon dioxide gas. Because of these distinct degradation pathways, the required non-covalent passivation strategies must target different targets. For black phosphorus, dense hydrophobic aromatic networks like perylene di-imides are deployed as a blanket physical barrier to block oxygen diffusion entirely. For MXenes, molecular engineering focuses on preferential capping of chemically active edge and defects sites. Polyanions and cationic surfactants preferentially adsorb at these locations, where they reduce the accessibility of water and oxygen to exposed titanium centres and suppress the nucleation of titanium oxides. Guided by these mechanistic insights, the molecular systems investigated in this work were designed to improve upon existing passivators by promoting favourable interfacial interactions while simultaneously enhancing resistance towards structural degradation.

4.4 General trends

Across BPNSs and MXene, some patterns of non-covalent stabilisation are shared. In both cases, protection is strongly influenced by how well the molecule's charge and structure matches the surface chemistry, meaning interactive compatibility with the surface is consistently a prerequisite for effective adsorption, even though the deeper mechanism that follows from that adsorption can differ.

What they do not share is the dominant protection mechanism itself. BP stabilisation depends on specific electronic interactions, since its degradation is tied to photoexcited charge transfer, so protection favours small, mobile molecules capable of close, well-oriented surface contact. MXene stabilisation depends more on physical barrier formation and adsorption strength, since its degradation relies on continuous water and oxygen access, so protection favours larger or multivalent structures that maximize surface coverage and persistence. As a result, the structural features that help a molecule perform well on one material, small size and mobility for BP, bulk and multivalent electrostatic binding for MXene, are often the features that limit its performance on the other.

For BP-directed systems, keeping the backbones short and simple with accessible electron-accepting core and keeping the molecule mobile enough for close, flat surface contact helped with protection against ambient degradation. For MXene-directed systems, backbones were extended or repetitive, allowing multiple cationic or hydrogen-bonding groups to act cooperatively along one chain, consistent with multivalent binding.

5. From Protection to Practical Function through Molecular Design

5.1 Key takeaways

The results of this work show that non-covalent functionalisation does not act through a single, universal mechanism, even when the same molecule and the same goal, ambient stability, are involved. Protection arises from different physical mechanisms depending on the surface being functionalised, and a molecule's structure interacts with these mechanisms in ways that are not always predictable in advance. For instance, oligomer-**15a**, comprising of the same molecules (compound **3**) as the pendant groups which were observed to protect BPNS, was not effective at protecting BPNS but oligomer-**15b** was effective for MXene despite being the same cationic species. This shows that "good for stabilisation" is not a fixed property of a molecule but depends on the compatibility between molecular structure and the particular degradation pathway of the material it is applied to. The overall takeaway is that non-covalent functionalisation must be treated as a materials-specific design problem, one where the choice of molecule has to follow from an understanding of how a given material actually degrades, rather than being transferred by analogy from one material to another.

5.2 Design guidelines

Choosing a molecule for BPNS protection means prioritising the electronic character of the functional groups rather than their size or number. The functional group responsible for protection needs to act as an electron acceptor capable of intercepting photoexcited electrons from BPNS before they reach adsorbed oxygen. This favours planar, redox-active moieties, such as viologen or other electron-deficient aromatic units, that can sit flat against the surface and engage BPNS's exposed phosphorus lone pairs directly. Because this interaction depends on close, well-defined contact, the group should be presented on a small, mobile scaffold rather than a bulky or highly substituted one, and it should carry minimal steric hindrance around the redox-active core so that orientation on the surface isn't disrupted. Charge is still relevant, since a cationic group helps anchor the molecule to BP's polarized, defect-rich surface, but charge alone is not sufficient; the electronic accessibility of the redox-active group is what ultimately determines whether protection occurs.

Choosing a molecule for MXene protection shifts the emphasis toward electrostatic and multivalent binding rather than a specific redox function. Because the MXene surface is anionic, from its –O– and –OH terminations, functional groups need to be cationic and ideally repeated multiple times along a single scaffold, so that many binding events act cooperatively rather than relying on one strong interaction. Groups capable of hydrogen bonding with surface hydroxyls add further stability, and a flexible backbone that can spread across the surface and conform to it is more useful here than a compact, rigid one, since the goal is maximizing coverage rather than achieving one precise binding geometry. The same cationic group that worked poorly on BP, when it lacked electronic accessibility due to steric bulk, can work well here, because MXene protection doesn't require orbital-level contact, only consistent electrostatic engagement across many sites.

5.3 Designing molecular systems for energy-storage application

Building on the design guidelines above, this section outlines the molecular systems chosen for further study for which backbone choice determines how a functional group is going to interact with the nanosheet surfaces and how many redox-active sites it can carry. Stability on its own is not a final goal; protected materials must still be able to perform in real devices. For this reason, our focus shifts toward creating molecules that support practical function alongside preservation. In this chapter, I used the lessons from earlier sections to guide the development of new organic systems aimed at energy-storage applications, where both the ability to interact with 2D materials and useful electrochemical behaviours are required.

Pyrene-4,5,9,10-tetraone (PyT, later mentioned as compound **17**) was chosen as a core scaffold for its extended, planar aromatic system and two ortho-quinone units, which make it strongly electron-accepting while allowing flat and planar geometry. Since PyT offers two isolated electron-accepting sites on one scaffold, it might be worthwhile to check whether it can outperform single-site acceptors like viologens which has been successful in protecting BP against degradation considerably. And since viologens has already been the focus for protecting the 2D materials it might still be of value for the designs of newer molecules. Attaching viologen-like scaffolds to the PyT backbone might theoretically add two more sites for electron acceptance without changing the planar geometry significantly. This not only can make it useful for the reversible electron storage mechanisms (**Scheme 5.1**) required for good electrochemical performances but also tests whether the protection of the oxidation-prone 2D materials scales with π-conjugation of the shielding agent itself, or whether the compact viologen core is already close to optimal for BP.

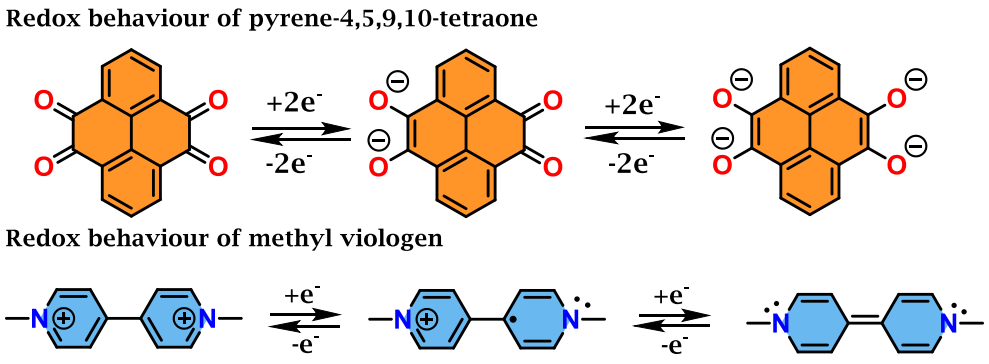

Scheme 5.1 *Redox behaviour of the pyrene-4,5,9,10-tetraone and methyl viologen systems*

Mixed-dimensional 3D-on-2D architectures are gaining a lot of interests lately as their interesting electronic interfaces are expected to play crucial role in surpassing the current limit of 2D materials, especially in electronic, optoelectronic and in spintronic applications.[91] Here I developed an idea of a viologen-like quaternary iminium-based zwitterionic system (Quaternary Iso-Nicotinic Acid based, in short: QINAgen class), carrying both a cationic and an anionic site, mainly as a linker for metal-organic frameworks (MOFs). The anionic group might anchor the linker to metal nodes, while the cationic parts might act as redox sites whilst being exposed to the pores. This might also be

proven to be very useful as a 3D-on-2D architectures with MXenes as they might possess cationic surface charges essential for a good non-covalent interaction with MXenes.

Together, these systems isolate different variables from the design guidelines, electron-accepting strength, degree of π-conjugation, and charge balance, so their individual contributions to BPNS and MXene protection as well as their electrochemical performance could be evaluated.

5.3.1 Pyrene-4,5,9,10-tetrone based molecular systems

Our design of the pyrene-based acceptor system (compound **25a**) involves two units of methyl pyridinium scaffolds onto the 2 and 7 positions of the pyrene and the ketone groups are located at the 4, 5, 9 and 10 positions. Addition of the pyridine could be achieved by Suzuki Coupling onto the pyrene backbone. However, the coupling requires Pd-catalysts and the two diketones in the pyrene-4,5,9,10-tetraone system being very efficient redox active sites deactivates the catalysts rendering the coupling unsuccessful. Hence the two diketone systems need to be protected prior to the coupling steps. The coupling, therefore, could be performed in two different ways e.g., either between a boronic ester derivative of protected pyrene-4,5,9,10-tetrone (Compound **21**) and bromo-derivatives of pyridine (Path B, **Scheme 5.2**) or between a dibromo- derivative of protected pyrene-4,5,9,10-tetrone (Compound **19**) and boronic acid/ester- derivatives of pyridine (Path B, Scheme X).

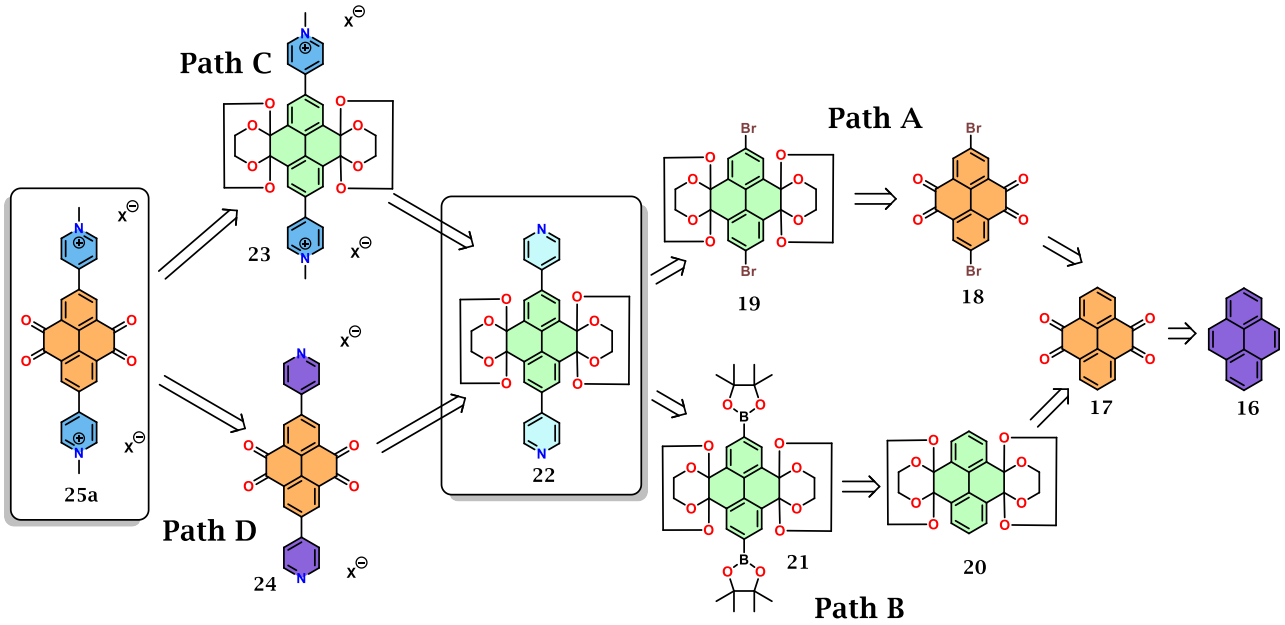

Scheme 5.2 *Retrosynthetic pathways for the pyrene-4,5,9,10-tetrone derivative* ***25a****.*

Pyrene-4,5,9,10-tetrone (**17**) was synthesised from pyrene (**16**); this step is an oxidation reaction and usually gives low to moderate yield. Many attempts have been taken to find the perfect oxidants and catalyst-systems dating back to 1937 (Oxidant: Chromic acid, products: 2,7-dione, 1,6-dione and 1,8-dione).[92] Then back in 1959, when the oxidation of pyrene by osmium tetroxide (OsO_4) and ruthenium dioxide (RuO_2) was described instead of chromic acid based oxidations, where pyrene-4,5-dione was showed as one of the major products formed with a maximum yield of 23%. The yield was maximum when OsO_4 was used and scaled with the increased molar ratio of periodate to pyrene (5:1).[93] The

periodate was more efficient as an oxidant compared to hydrogen peroxide in terms of regenerating the catalysts (water was important for this step) along with which, higher consumption of pyrene was also observed. However, when RuO_2 was used the yield dropped to 11% along with other -diketone products such as 1,6-diketone and some unknown aldehydes and carboxylic acids (**Scheme 5.3**). Then in 1974, the pyrene-4,5-dione was reported to be synthesised from sodium dichromate dihydrate in an acidic mixture of acetic anhydride and acetic acid (1:1).[94] These oxidation steps are extremely harsh and uses very toxic and corrosive substances, and only the RuO_2 based oxidation was fairly okay to work with. Later many other systems were also developed such as hydrogen peroxide with iron(III)porphyrin complexes[95] and higher valent iodine species (H_2IO_5 and HIO_3)[96] to further convert pyrene to pyrene-4,5,9,10-tetrone, for this oxidation step but the Ru-based step remains much safer and easier alternative with a decent yield to operate in a lab scale.

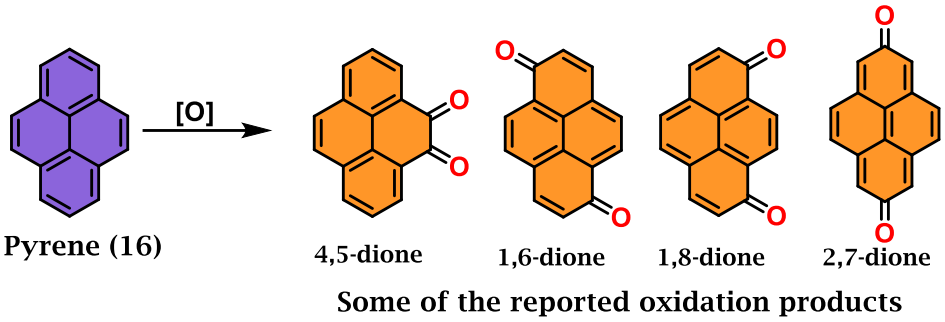

Scheme 5.3 *Oxidation products possibly generated in the oxidation of pyrene (**16**).*

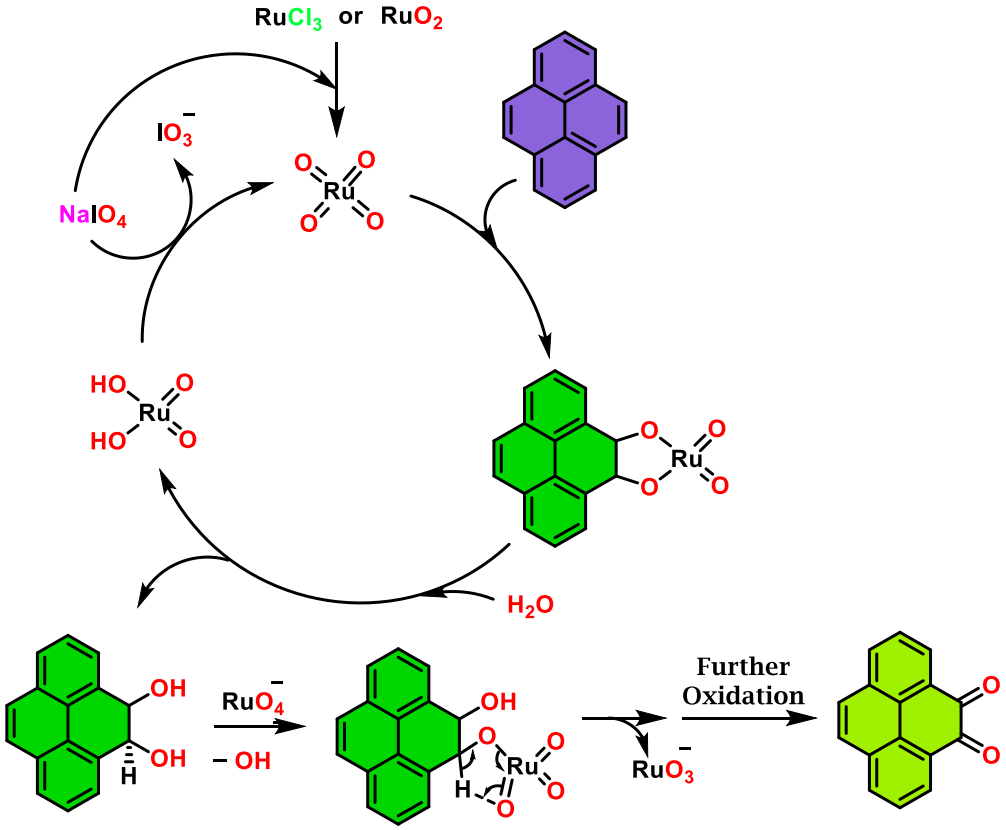

Scheme 5.4 *Plausible mechanism for Ru-based oxidation.*[97, 98]

The oxidation of pyrene, hence, was performed following a now well-known IO_4^- based oxidation reaction with $RuCl_3$ as the catalyst (In situ RuO_4, **Scheme 5.4**) in a ternary mixture of solvents (dichloromethane, acetonitrile and water in a ratio of 4:4:5)[99] where in situ RuO_4 formation is speculated.[100] Higher valent ruthenium oxide species are known to be sluggish and incomplete in the absence of acetonitrile as a co-solvent. Addition of acetonitrile helps in keeping the relative content of the active species high by coordinating with the lower valent ruthenium species inhibiting the coordination with byproducts (carboxylic acids), allowing the regeneration of the catalyst.[101] The double bromination (Path A) at the 2,7- positions was achieved by N-bromosuccinimide in concentrated sulfuric acid environment to yield **18** (**Scheme 5.5**).

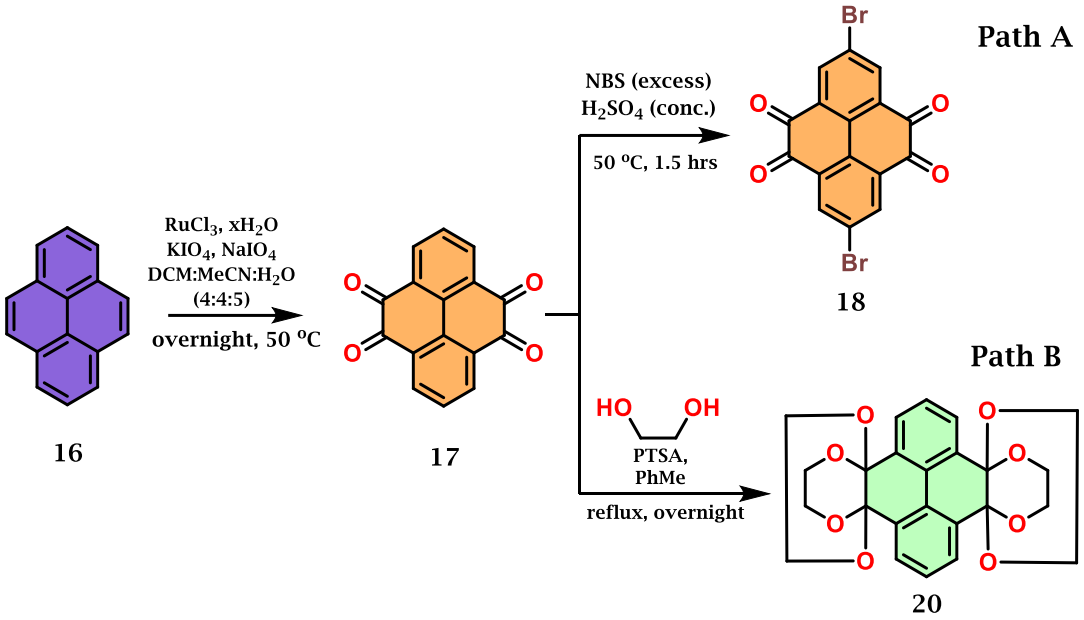

Scheme 5.5 *Synthetic routes from pyrene to path A and path B through pyrene-4,5,9,10-tetraone.*

The path B involves the protection of the -tetraone system first. The protection of **17** was performed using ethylene glycol, catalysed by p-toluenesulphonic acid, in refluxing toluene. The protection of **18** in path A was performed using the same condition as before, yielding **19** (Path A, **Scheme 5.8**) for the coupling step. In path B, a pinacol boronate addition at the 2,7- position of compound **20** was performed using bis(pinacolato)diborane through iridium-based borylation. The pre-catalyst used was a dimer of Ir–OMe where each iridium is also protected by one 1,5-cyclooctadiene unit ($[Ir(COD)OMe]_2$, **Scheme 5.6**). This is a very known C–H activator and a very well-known borylating agent.[102, 103] This step is suspected to depend on PinB–OMe (**Scheme 5.6**) formation resulting in $[Ir(dtbPy)(COD)](BPin)_3$.[102] This gave product **21** with moderate yields and the Suzuki coupling was performed on both compound **19** and **21**. The synthetic route from **16** to **19** and **16** to **21** has been reported previously,[104] however, the Suzuki coupling product (Compound **22**, **Scheme 5.2**) is completely novel and has never been prepared before.

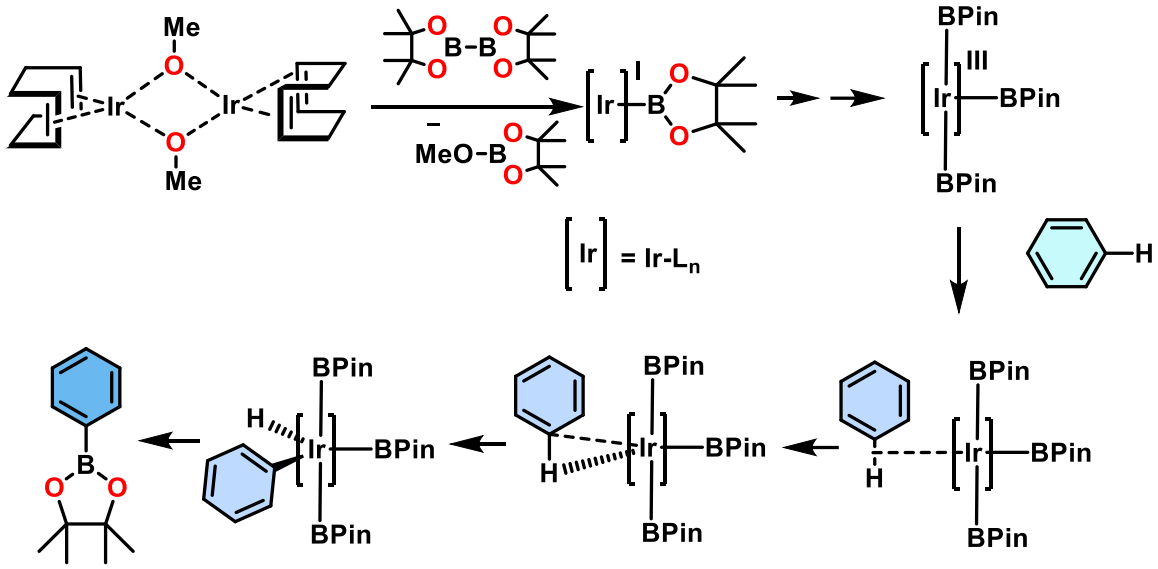

Scheme 5.6 *Plausible mechanism for Ir-based borylation.*[105]

A Suzuki coupling (**Scheme 5.7**) was then performed between **19** and 4-pyridinylboronic acid in path A, and between **21** and p-bromopyridine in path B, catalysed by XPhos-Pd-G2 (**Scheme 5.8**). The reaction was performed using a typical Suzuki coupling setup with a binary mixture of solvents (1M aq. Cs_2CO_3 and dry THF with a 1:1 ratio) under a nitrogen environment to yield **22**. The path B yielded trace product whereas path A yielded notably larger conversion. Therefore, path A was used in subsequent synthesis of required compounds.

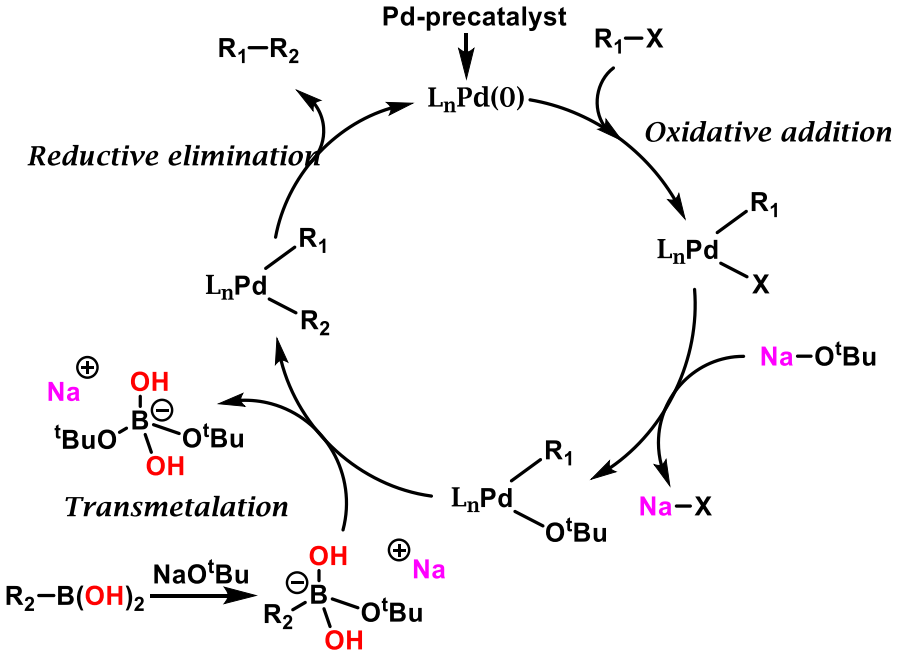

Scheme 5.7 *Plausible mechanism for Suzuki coupling.*

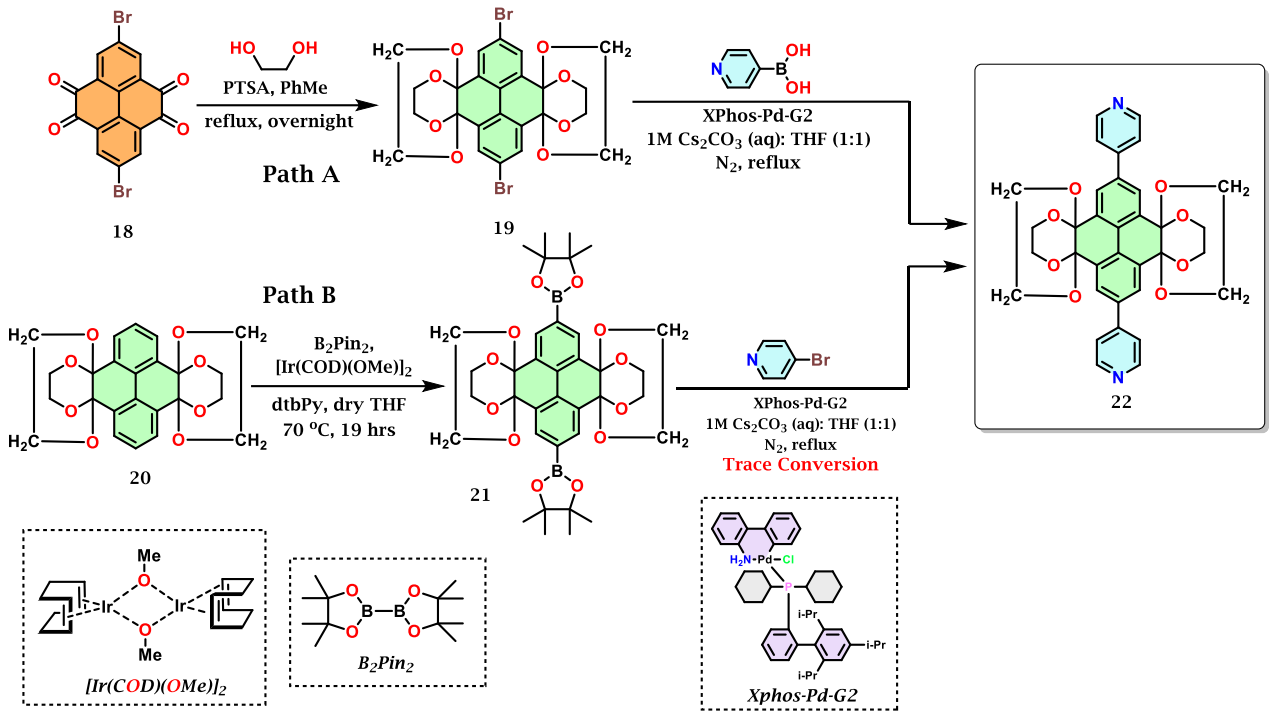

Scheme 5.8 *Synthetic routes towards the Suzuki-coupling step following path A and path B.*

Compound **23** was prepared by di-methylation of **22** using an excess of methyl iodide. For the deprotection of the ketals on **23**, TFA:H_2O (9:1) was employed. However, so far, no evidence for the formation of compound **25a** has been obtained (**Scheme 5.9**). A shift of the aromatic protons towards high ppm indicates toward a more electron deficient nature of the product formed. However, one extra aliphatic proton peak and several aliphatic carbon (one connected to a heteroatom) points in the direction of incomplete deprotection (Appendix: Experimental Section, **Figure A 20**, **Figure A 21**).

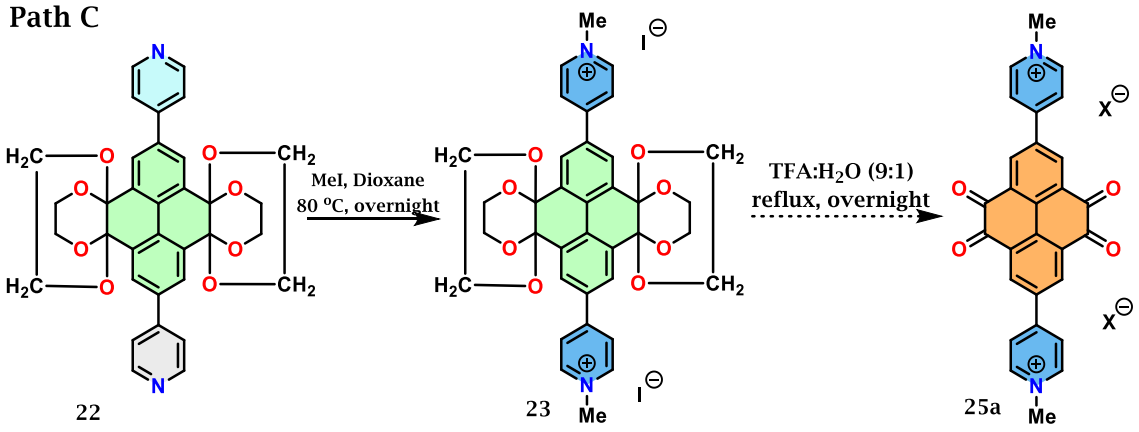

Scheme 5.9 *Synthetic routes for methylation followed by the deprotection of the keto-groups.*

The deprotection of the Suzuki coupling product was also performed using the similar system mentioned above as it might be a very good donor-acceptor (D-A) system (Compound **24**, **Scheme 5.10**). The scale for the reaction was much less; hence, the NMR signals are not conclusive about the product forming. Further standardisation of this step along with a good purification method needs to be developed.

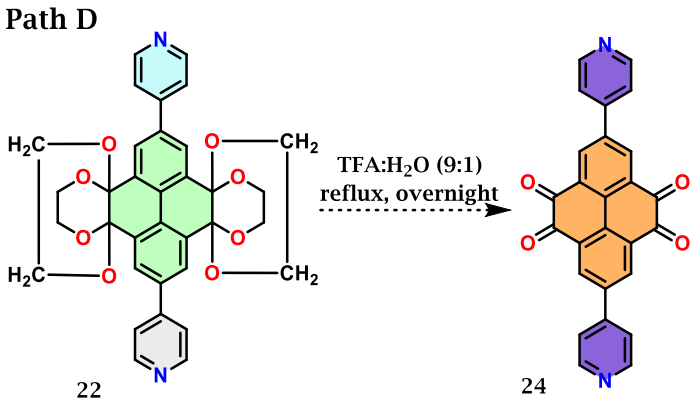

Scheme 5.10 *Synthetic routes for the deprotection of the keto-groups for D-A systems (**24**).*

Furthermore, I wanted to explore structure-property relationships in the molecular context and observe if the electron-storage mechanism might be similar for the monosubstituted version, compound **25b** (**Scheme 5.11**). Conceptually it must be different from **25a** as the redox behaviour of **25b** would involve an odd number of electrons and reduced version would be a radical. To explore all these ideas, the synthesis for **25b** was initiated.

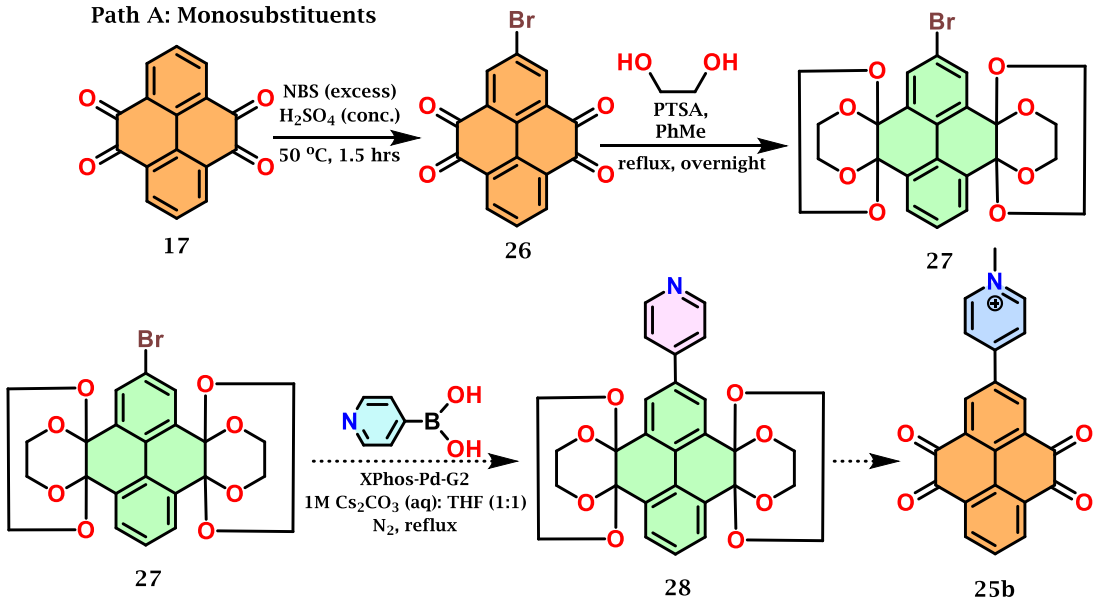

Scheme 5.11 *Synthetic strategy towards mono-side substitution following path A.*

The mono-bromo derivative (**26**), the ketal-protection (**27**) and the Suzuki coupling (**27** to **28**) was performed following the exact same procedure as before. However, the Suzuki-coupling product not successfully isolated (**Scheme 5.11**).

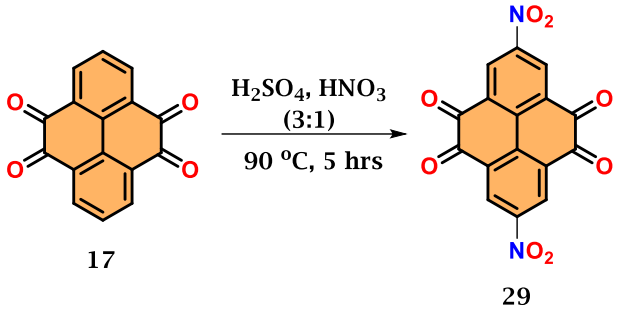

17 29

Scheme 5.12 *Nitration of* ***17*** *to synthesise 2,7-dinitro product.*

I also prepared 2,7-dinitro derivative (**29**) to make the system more electron-deficient. The nitration was done using a mixture of concentrated sulphuric acid and fuming nitric acid (3:1) at 90 °C (**Scheme 5.12**). Preliminary titration of BPNSs (**Figure 5.1a**) and MXene (**Figure 5.1b**) with **29** in acetonitrile didn't reveal much information about the interaction behaviour. Also, the physical aggregation behaviour was neither consistent nor conclusive.

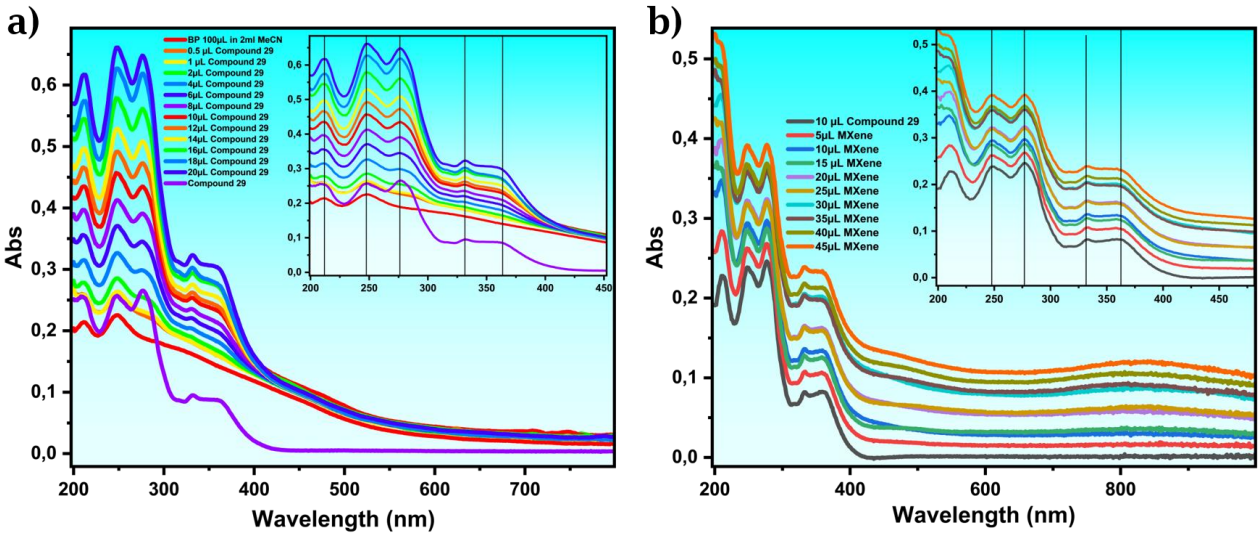

Figure 5.1 *UV-Vis titration of both (a) BPNS and (b) MXene with compound* ***29*** *with no significant indication towards non-covalent interaction.*

5.3.2 QINAgen-based framework systems (QDINA-linker)

Scientific discussions with *William Reinholdsson* from *Lars Öhrström's group* led to the idea of a linker comprising three benzene rings, similar to the linkers used in UiO-68 series of MOFs. A key difference is that the proposed linker contains a delocalised positive charge, which is expected to introduce electrostatic repulsion between neighbouring linkers. This would mean that the linker would be zwitterionic and there would be a possibility of two redox-sites. Our primary objectives were to monitor how the topology of the MOF changes, if the charged environment gave rise to interesting host-guest phenomena and last but not least, to improve its electrochemical performance. Since both goals depend on the building blocks of the framework, I began by synthesizing the linker system.

The QDINA-linker (Quaternary di-isonicotinic acid) synthesis is very similar to that of the other viologens, apart from the fact that the carboxylic acid group has to be protected

(**Scheme 5.13**). Hence, the ester-derivative of the isonicotinic acid (**30**) was chosen for the Zincke salt (**31**) preparation. The salt was then reacted to 1,4-phenylenediamine to yield compound **32**, which was charged. Numerous previously reported MOF synthesis procedures have employed in situ ester hydrolysis. The gradual hydrolysis of the ester can reduce overall reaction rate and thereby favour controlled MOF-growth. Simple hydrolysis of the compound **32** was performed to verify its crystal structure (Appendix: Experimental Section, **Figure A 30**).

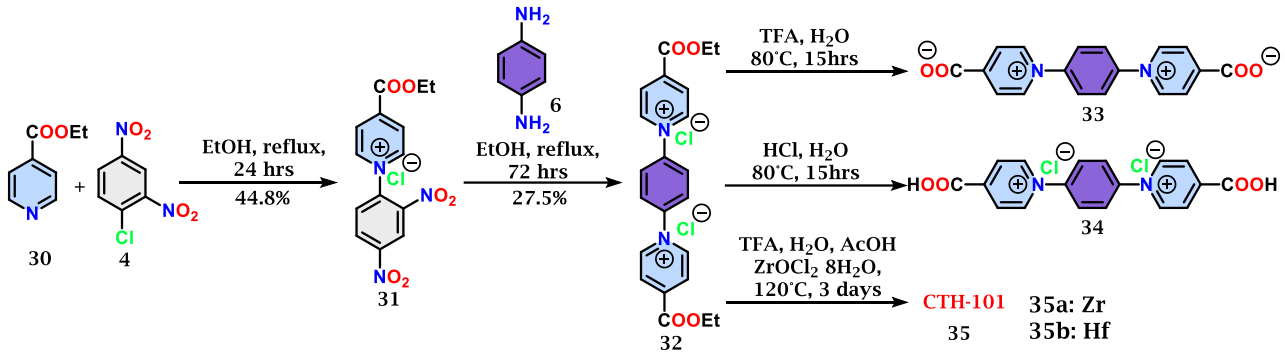

Scheme 5.13 *Synthesis scheme for the QDINA-linker and* ***CTH-101*** *synthesis strategy.*

The MOF **CTH-101** (**35**) synthesis and characterisations including the crystallographic analyses was performed by *Lars Öhrström's group*. To our surprise, the topology never came to be a UiO-68, instead we found a much less discussed topology called the **Reo** net which consisted of two kinds of pores, octahedral pores with vdW diameter of 17 Å and cuboctahedral pores with vdW diameter of 34 Å (**Figure 5.2**). We obtained two variants of **35** by using zirconium (Zr) and hafnium (Hf) metals for the clusters at the nodes.

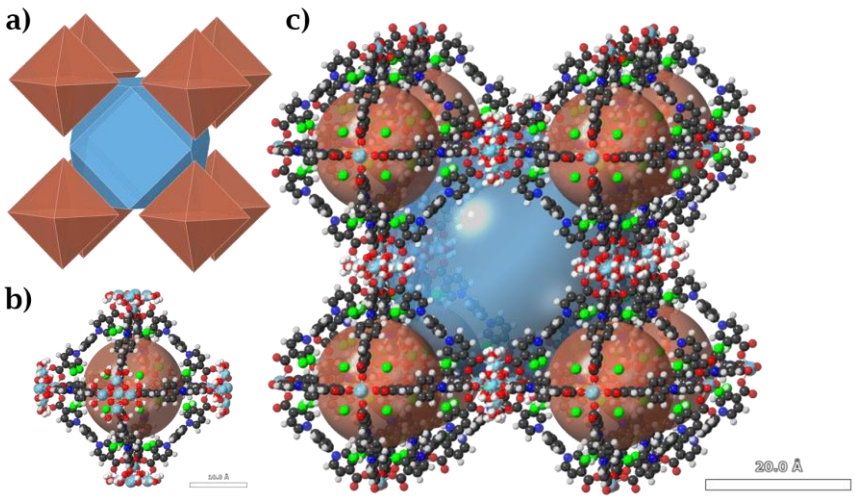

Figure 5.2 *Illustration of Reo net topology, (a) the octahedra and the cuboctahedron forming the Reo net, (b) QDINA-linker and Zr_6-clusterencapsulating the octahedron and (c) the octahedra connecting to create the cuboctahedral cavity.*

XPS was performed to get further refinement on the structure and some key details surfaced that helped with the structure determination of **35**. From Zr3d spectra (**Figure 5.3b**) it was evident that there were two different Zr-species in the cluster. Their ratio was calculated from the peak intensities and it turned out to be approximately 2:1, which is correlatable to the equatorial and axial Zr-atoms in the cluster. From the O1s spectra in **Figure 5.3c** the amount of oxygen from water coordinated to the cluster was found to be almost similar to the amount of the oxygen in constituting the cluster. In the linker, there are 3-carbons connected to each nitrogen (total 6 of such carbon) atom and there are two carbons which are connected to oxygens;

which was also observed in the C1s spectra (C_N:C_O ~ 3:1, **Figure 5.3e**). N1s spectrum showed typical viologen behaviour as explored in both chapter 2 and 3 (**Figure 5.3f**). The most important clue found was that there were chloride signals present in the survey spectra (Cl2p at 197.75 eV and Cl2s at 269.75 eV, **Figure 5.3a**) and their amount is more or less the same as the amount of the nitrogen in the framework. This helped us look into the chemical environment of the MOF and *Lars Öhrström's group* made an educated guess on mapping the chloride ions which previously could not be located on the electron density map; and we could finally arrive at the formula for the **CTH-101** (**35a**) as, $[Zr_6O_8(OH_2)_8(QDINA)_4]Cl_8$.

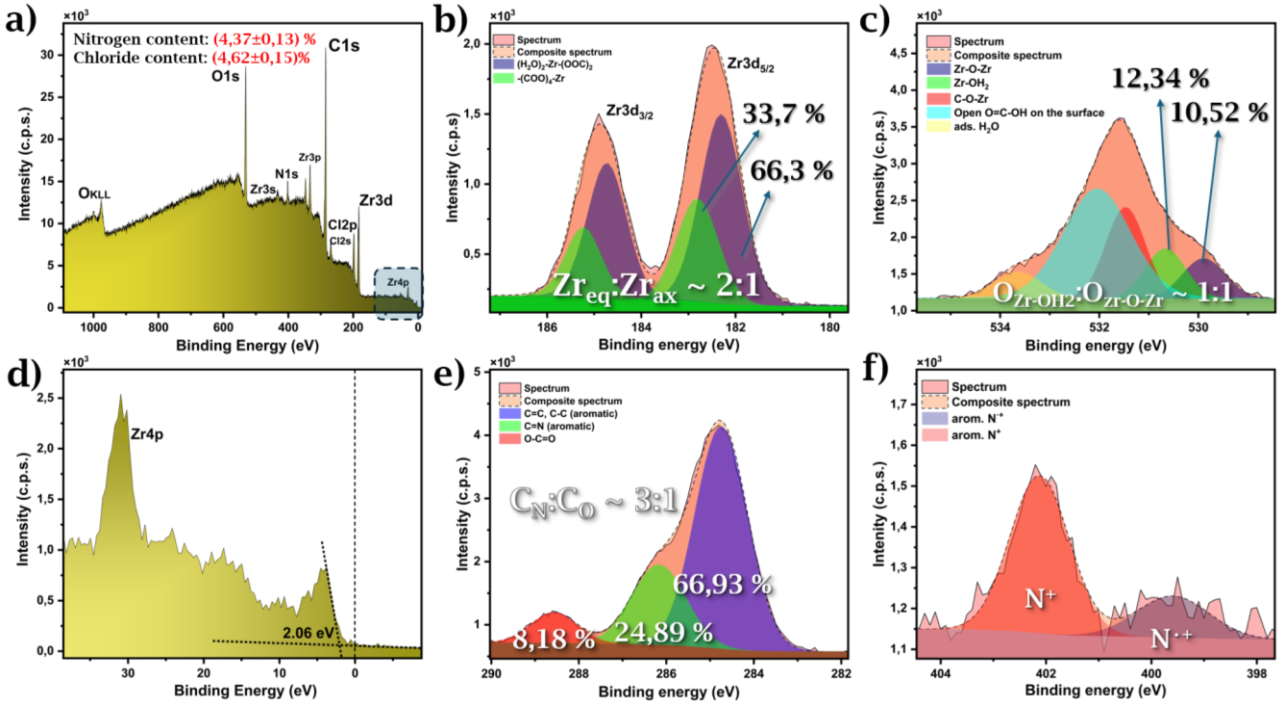

Figure 5.3 *XPS spectra showing (a, d) survey spectra showing all the elemental signals, (b) Zr3d, (c) O1s, (e) C1s and (f) signature viologen-type N1s spectrum.*

These discussions also addressed the possible relationship between crystal structure, crystal growth, and the resulting morphology of the microcrystals. Although the origin of the observed morphologies remains uncertain, crystals exhibiting well-defined polyhedral shapes were occasionally obtained. In particular some **CTH-101** crystals displayed morphologies resembling the cuboctahedra and the octahedra, as observed by both optical microscopy and SEM (**Figure 5.4**). These observations provide an interesting illustration of the distinct microcrystalline morphologies that can emerge during the MOF growth.

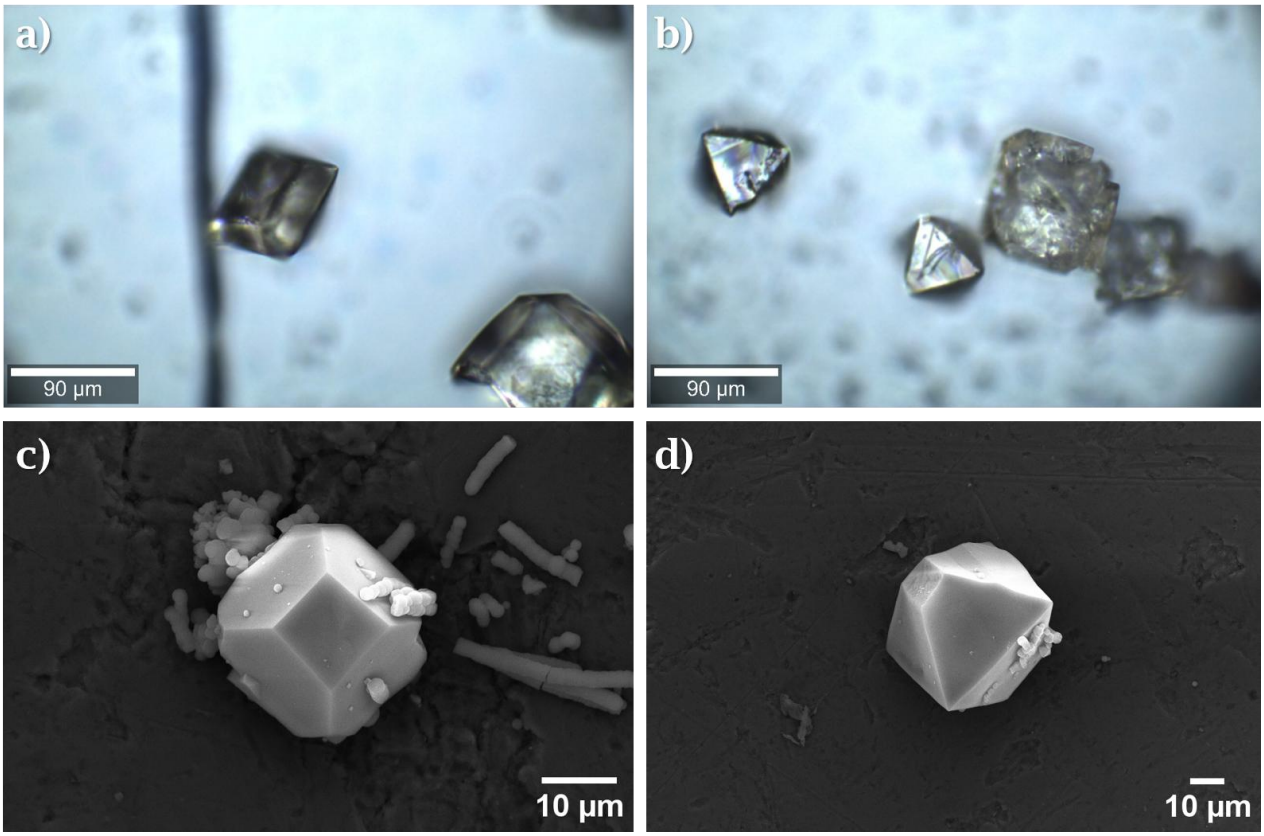

Figure 5.4 *Crystals of* ***CTH-101*** *under (a) optical microscope and (b) SEM.*

The energy-storage application was evaluated by electrochemical measurements which were performed by the lab members from our group in *Tianjin University*, China and the discussion is beyond the scope of this thesis. They showed that **CTH-101(Zr, 35a)** electrode delivers a specific capacitance of 42.2 F/g at a current density of 1 A/g and a capacitance retention of 66% after 7,500 cycles at 2 A/g. The **CTH-101(Zr, 35a)**//Fe-HCF full cell delivers a specific capacitance of 14.7 F/g at 0.2 A/g with a capacitance retention of 71.1% after 3,000 cycles at a current density of 1 A/g. The **CTH-101(Hf, 35b)** electrode delivers a specific capacitance of 29.7 F/g at a current density of 1 A/g and a capacitance retention of 56% after 5,500 cycles at 2 A/g. The **CTH-101(Hf, 35b)**//Fe-HCF full cell delivers a specific capacitance of 15.6 F/g at a current density of 0.2 A/g with a capacitance retention of 64.1% after 3,000 cycles at a current density of 1 A/g. This are very important results as while providing good performance in framework context[106] the architecture remains intact and we do not have to resort to any other destructive processes to create new materials (e.g., carbonization to make frameworks into carbon materials without metals[107]) to improve the performance.

6. Summary and Outlook

6.1 Conclusion

This thesis work was set out to examine how non-covalent modification can protect 2D BP and $Ti_3C_2T_x$ MXene from ambient degradation. Along the way we designed a set of molecules and materials with carefully varied features, we built our hypothesis of what can work, what might not. One thing that became evident was that the effectiveness of a molecular design depended as much on the properties of the material as on the molecular structure itself. Often times, we see materials characteristics being generalised in many contexts, and the focus shifts to molecular systems with interesting and appealing phenomena, regardless of whether they are effective or not. This study enables us to identify which molecular features lead to meaningful protection and why.

The results demonstrate that 2D BP and MXene require fundamentally different approaches. Black phosphorus nanosheets are best stabilised by small, planar molecules capable of intercepting electrons and slowing photo-oxidation. MXene, in contrast, benefits from larger, flexible, multivalent molecules that can cover the surface and physically limit access to water and oxygen. Molecules that were effective for one material might fail on the other, confirming that protection strategies cannot be universal across 2D materials.

Computational analysis helped clarify the interaction modes responsible for protection and guided the design of new candidates. Combined with XPS, Raman spectroscopy and electron microscopy, , this approach allowed the protective behaviour to be demonstrated directly rather than inferred from slowed degradation alone.

Overall, the findings show that successful stabilisation of 2D materials relies on selecting molecules that interact with the surface in a way that addresses the specific degradation pathway. This provides a clearer basis for designing non-covalent functionalisation strategies that are predictable and material-specific.

6.2 Future work

The findings in this thesis point towards several directions in which the protective systems developed here can be evaluated more broadly and applied in practical contexts.

Some of the molecular systems explored, including the pyrene-4,5,9,10-tetraone and viologen pair, were designed to interact with the surface through reversible electron transfer. A next step is to test these coated materials directly in electrochemical devices such as batteries or supercapacitors. This would clarify whether the protective interaction also contributes to charge storage, cycling stability, or long-term performance under operational conditions. **CTH-101** has already tested for such applications and showed promising results. The properties of 2D materials (e.g., the metallic conductivity of MXenes, which could be very useful for electron injection), coupled with this redox-active framework in a 2D-3D mixed-dimensional architecture, could open the door to highly efficient electron-storage devices alongside a variety of other applications.

2D BP remains attractive for electronic applications, but its sensitivity to ambient conditions limits device reliability. The coatings developed here should be tested in simple device structures to determine whether they preserve or modify key electronic properties such as conductivity, mobility, and bandgap behaviour. This would show how the interaction mode influences device-level performance, not only material stability.

Several of the protective molecules exhibit environmental sensitivity or redox activity, which may be useful beyond stabilisation. Exploring whether these encapsulated materials can respond to chemical analytes would extend their function into sensing applications. This would also test whether the same interaction modes that provide protection can be used for detection.

The contrasting requirements of 2D BP and MXene highlight the need for material-specific strategies. Applying the same design approach to other 2D materials, e.g., MoS_2, Nb_2C MXenes, or emerging phosphorene derivatives, would help determine how widely the interaction principles identified here can be transferred.

Bibliography

1. Melsen, A. G. V., History and major representatives of the various atomisms. Encyclopædia Britannica, Inc.: **2025**.
2. Durant, W., *Our Oriental Heritage: The Story of Civilization*. Simon and Schuster, Inc.: **1935**; Vol. 1.
3. Novoselov, K. S.; Geim, A. K.; Morozov, S. V.; Jiang, D.; Zhang, Y.; Dubonos, S. V.; Grigorieva, I. V.; Firsov, A. A., *Science* **2004,** *306* (5696), 666.
4. Geim, A. K. Sir Andre Geim at GYSS 2023 – Random Walk to Graphene. https://youtu.be/lWB6JjaMh4w (accessed January 18).
5. Foller, T.; Joshi, R., *Curr. Opin. Solid State Mater. Sci.* **2024,** *32*, 101186.
6. Novoselov, K. S.; Geim, A. K.; Morozov, S. V.; Jiang, D.; Katsnelson, M. I.; Grigorieva, I. V.; Dubonos, S. V.; Firsov, A. A., *Nature* **2005,** *438* (7065), 197.
7. Joensen, P.; Frindt, R. F.; Morrison, S. R., *Mater. Res. Bull.* **1986,** *21* (4), 457.
8. Mattheiss, L. F., *Phys. Rev. B* **1973,** *8* (8), 3719.
9. Group®, D. M. G. Molybdenum Disulfide (MoS_2): Key Milestones in MoS_2 Research. https://molybdenumdisulfide.com/en/ (accessed October 21).
10. Radisavljevic, B.; Radenovic, A.; Brivio, J.; Giacometti, V.; Kis, A., *Nat. Nanotechnol.* **2011,** *6* (3), 147.
11. Bridgman, P. W., *J. Am. Chem. Soc.* **1914,** *36* (7), 1344.
12. Ling, X.; Wang, H.; Huang, S.; Xia, F.; Dresselhaus, M. S., *Proc. Natl. Acad. Sci.* **2015,** *112* (15), 4523.
13. Morita, A., *Appl. Phys. A* **1986,** *39* (4), 227.
14. Asahina, H.; Shindo, K.; Morita, A., *J. Phys. Soc. Jpn.* **1982,** *51* (4), 1193.
15. Takao, Y.; Asahina, H.; Morita, A., *J. Phys. Soc. Jpn.* **1981,** *50* (10), 3362.
16. Tran, V.; Soklaski, R.; Liang, Y.; Yang, L., *Phys. Rev. B* **2014,** *89* (23), 235319.
17. Liu, Y.; Xu, F.; Zhang, Z.; Penev, E. S.; Yakobson, B. I., *Nano Lett.* **2014,** *14* (12), 6782.
18. Yu, X.-f.; Ushiyama, H.; Yamashita, K., *Chem. Lett.* **2014,** *43* (12), 1940.
19. Castellanos-Gomez, A.; Vicarelli, L.; Prada, E.; Island, J. O.; Narasimha-Acharya, K. L.; Blanter, S. I.; Groenendijk, D. J.; Buscema, M.; Steele, G. A.; Alvarez, J. V.; Zandbergen, H. W.; Palacios, J. J.; van der Zant, H. S. J., *2d Mater.* **2014,** *1* (2), 025001.
20. Zhang, S.; Yang, J.; Xu, R.; Wang, F.; Li, W.; Ghufran, M.; Zhang, Y.-W.; Yu, Z.; Zhang, G.; Qin, Q.; Lu, Y., *ACS nano* **2014,** *8* (9), 9590.
21. Wang, H.; Wang, X.; Xia, F.; Wang, L.; Jiang, H.; Xia, Q.; Chin, M. L.; Dubey, M.; Han, S.-j., *Nano Lett.* **2014,** *14* (11), 6424.
22. Du, Y.; Liu, H.; Deng, Y.; Ye, P. D., *ACS nano* **2014,** *8* (10), 10035.
23. Das, S.; Zhang, W.; Demarteau, M.; Hoffmann, A.; Dubey, M.; Roelofs, A., *Nano Lett.* **2014,** *14* (10), 5733.
24. Buscema, M.; Groenendijk, D. J.; Blanter, S. I.; Steele, G. A.; van der Zant, H. S. J.; Castellanos-Gomez, A., *Nano Lett.* **2014,** *14* (6), 3347.
25. Buscema, M.; Groenendijk, D. J.; Steele, G. A.; van der Zant, H. S. J.; Castellanos-Gomez, A., *Nat. Commun.* **2014,** *5* (1), 4651.
26. Hong, T.; Chamlagain, B.; Lin, W.; Chuang, H.-J.; Pan, M.; Zhou, Z.; Xu, Y.-Q., *Nanoscale* **2014,** *6* (15), 8978.
27. Kou, L.; Frauenheim, T.; Chen, C., *J. Phys. Chem. Lett.* **2014,** *5* (15), 2675.
28. *P, black phosphorus (P black, p = 0.71 GPa) Crystal Structure: Datasheet from "PAULING FILE Multinaries Edition – 2022" in SpringerMaterials (https://materials.springer.com/isp/crystallographic/docs/sd_1214637)*, Springer-Verlag Berlin Heidelberg & Material Phases Data System (MPDS), Switzerland & National Institute for Materials Science (NIMS), Japan.

29. Keyes, R. W., *Phys. Rev.* **1953,** *92* (3), 580.
30. Warschauer, D., *J. Appl. Phys.* **1963,** *34* (7), 1853.
31. Xia, F.; Wang, H.; Jia, Y., *Nat. Commun.* **2014,** *5* (1), 4458.
32. Liang, L.; Wang, J.; Lin, W.; Sumpter, B. G.; Meunier, V.; Pan, M., *Nano Lett.* **2014,** *14* (11), 6400.
33. Mak, K. F.; Lee, C.; Hone, J.; Shan, J.; Heinz, T. F., *Phys. Rev. Lett.* **2010,** *105* (13), 136805.
34. Britnell, L.; Ribeiro, R. M.; Eckmann, A.; Jalil, R.; Belle, B. D.; Mishchenko, A.; Kim, Y.-J.; Gorbachev, R. V.; Georgiou, T.; Morozov, S. V.; Grigorenko, A. N.; Geim, A. K.; Casiraghi, C.; Neto, A. H. C.; Novoselov, K. S., *Science* **2013,** *340* (6138), 1311.
35. Naguib, M.; Kurtoglu, M.; Presser, V.; Lu, J.; Niu, J.; Heon, M.; Hultman, L.; Gogotsi, Y.; Barsoum, M. W., *Adv. Mater.* **2011,** *23* (37), 4248.
36. Speight, J., *Lange's Handbook of Chemistry*. 16 ed.; McGraw-Hill Education LLC: **2005**.
37. Lim, K. R. G.; Shekhirev, M.; Wyatt, B. C.; Anasori, B.; Gogotsi, Y.; Seh, Z. W., *Nat. Synth.* **2022,** *1* (8), 601.
38. Halim, J.; Lukatskaya, M. R.; Cook, K. M.; Lu, J.; Smith, C. R.; Näslund, L.-Å.; May, S. J.; Hultman, L.; Gogotsi, Y.; Eklund, P.; Barsoum, M. W., *Chem. Mater.* **2014,** *26* (7), 2374.
39. Lashgari, H.; Abolhassani, M. R.; Boochani, A.; Elahi, S. M.; Khodadadi, J., *Solid State Commun.* **2014,** *195*, 61.
40. Hu, T.; Zhang, H.; Wang, J.; Li, Z.; Hu, M.; Tan, J.; Hou, P.; Li, F.; Wang, X., *Sci. Rep.* **2015,** *5* (1), 16329.
41. Zha, X.-H.; Zhou, J.; Zhou, Y.; Huang, Q.; He, J.; Francisco, J. S.; Luo, K.; Du, S., *Nanoscale* **2016,** *8* (11), 6110.
42. Khazaei, M.; Ranjbar, A.; Arai, M.; Sasaki, T.; Yunoki, S., *J. Mater. Chem. C* **2017,** *5* (10), 2488.
43. Bharathi, G.; Hong, S. Prospects of Band Structure Engineering in MXenes for Active Switching MXetronics: Computational Insights and Experimental Approaches *Materials* [Online], **2025**, p. 104.
44. Magnuson, M.; Eklund, P.; Polley, C., *Phys. Rev. Lett.* **2025,** *134* (10), 106201.
45. Nesterova, V.; Korostelev, V.; Klyukin, K., Ti3C2T2.zip. figshare: **2024**.
46. Mauchamp, V.; Bugnet, M.; Bellido, E. P.; Botton, G. A.; Moreau, P.; Magne, D.; Naguib, M.; Cabioc'h, T.; Barsoum, M. W., *Phys. Rev. B* **2014,** *89* (23), 235428.
47. Dong, Y.; Chertopalov, S.; Maleski, K.; Anasori, B.; Hu, L.; Bhattacharya, S.; Rao, A. M.; Gogotsi, Y.; Mochalin, V. N.; Podila, R., *Adv. Mater.* **2018,** *30* (10), 1705714.
48. El-Demellawi, J. K.; Lopatin, S.; Yin, J.; Mohammed, O. F.; Alshareef, H. N., *ACS nano* **2018,** *12* (8), 8485.
49. Miranda, A.; Halim, J.; Barsoum, M. W.; Lorke, A., *Appl. Phys. Lett.* **2016,** *108* (3), 033102.
50. Dillon, A. D.; Ghidiu, M. J.; Krick, A. L.; Griggs, J.; May, S. J.; Gogotsi, Y.; Barsoum, M. W.; Fafarman, A. T., *Adv. Funct. Mater.* **2016,** *26* (23), 4162.
51. Wang, Z.; Kim, H.; Alshareef, H. N., *Adv. Mater.* **2018,** *30* (15), 1706656.
52. Sangu, S. S.; Illias, N. M.; Ong, C. C.; Gopinath, S. C. B.; Saheed, M. S. M., *BioNanoScience* **2021,** *11* (2), 314.
53. Ma, S.; Fan, X.; An, Y.; Yang, D.; Luo, Z.; Hu, Y.; Guo, N., *J. Mater. Sci.* **2019,** *54* (17), 11378.
54. Slot, T. K.; Yue, F.; Xu, H.; Ramos-Fernandez, E. V.; Sepúlveda-Escribano, A.; Sofer, Z.; Rothenberg, G.; Shiju, N. R., *2d Mater.* **2021,** *8* (1), 015001.
55. Couly, C.; Alhabeb, M.; Van Aken, K. L.; Kurra, N.; Gomes, L.; Navarro-Suárez, A. M.; Anasori, B.; Alshareef, H. N.; Gogotsi, Y., *Adv. Electron. Mater.* **2018,** *4* (1), 1700339.

56. Jiang, Q.; Wu, C.; Wang, Z.; Wang, A. C.; He, J.-H.; Wang, Z. L.; Alshareef, H. N., *Nano Energy* **2018,** *45*, 266.
57. Jiang, Q.; Kurra, N.; Alhabeb, M.; Gogotsi, Y.; Alshareef, H. N., *Adv. Energy Mater.* **2018,** *8* (13), 1703043.
58. Pang, J.; Mendes, R. G.; Bachmatiuk, A.; Zhao, L.; Ta, H. Q.; Gemming, T.; Liu, H.; Liu, Z.; Rummeli, M. H., *Chem. Soc. Rev.* **2019,** *48* (1), 72.
59. Jeong, J. H.; Kang, S.; Kim, N.; Joshi, R.; Lee, G.-H., *Phys. Chem. Chem. Phys.* **2022,** *24* (18), 10684.
60. Weiss, C.; Wagner, C.; Temirov, R.; Tautz, F. S., *J. Am. Chem. Soc.* **2010,** *132* (34), 11864.
61. Aykol, M.; Doak, J. W.; Wolverton, C., *Phys. Rev. B* **2017,** *95* (21), 214115.
62. *Lange's Handbook of Chemistry*. 17th Edition ed.; McGraw-Hill Education: New York, **2017**.
63. Ziletti, A.; Carvalho, A.; Campbell, D. K.; Coker, D. F.; Castro Neto, A. H., *Phys. Rev. Lett.* **2015,** *114* (4), 046801.
64. Edmonds, M. T.; Tadich, A.; Carvalho, A.; Ziletti, A.; O'Donnell, K. M.; Koenig, S. P.; Coker, D. F.; Özyilmaz, B.; Neto, A. H. C.; Fuhrer, M. S., *ACS Appl. Mater. Interfaces* **2015,** *7* (27), 14557.
65. Huang, Y.; Qiao, J.; He, K.; Bliznakov, S.; Sutter, E.; Chen, X.; Luo, D.; Meng, F.; Su, D.; Decker, J.; Ji, W.; Ruoff, R. S.; Sutter, P., *Chem. Mater.* **2016,** *28* (22), 8330.
66. Zhou, Q.; Chen, Q.; Tong, Y.; Wang, J., *Angew. Chem. Int. Ed.* **2016,** *55* (38), 11437.
67. Abellán, G.; Wild, S.; Lloret, V.; Scheuschner, N.; Gillen, R.; Mundloch, U.; Maultzsch, J.; Varela, M.; Hauke, F.; Hirsch, A., *J. Am. Chem. Soc.* **2017,** *139* (30), 10432.
68. Cheng, W.-C.; Kurth, M. J., *Org. Prep. Proced. Int.* **2002,** *34* (6), 585.
69. Sofer, Z.; Luxa, J.; Bouša, D.; Sedmidubský, D.; Lazar, P.; Hartman, T.; Hardtdegen, H.; Pumera, M., *Angew. Chem.* **2017,** *129* (33), 10023.
70. Ribeiro, H. B.; Pimenta, M. A.; de Matos, C. J. S., *J. Raman Spectrosc.* **2018,** *49* (1), 76.
71. Favron, A.; Gaufrès, E.; Fossard, F.; Phaneuf-L'Heureux, A.-L.; Tang, N. Y. W.; Lévesque, P. L.; Loiseau, A.; Leonelli, R.; Francoeur, S.; Martel, R., *Nat. Mater.* **2015,** *14* (8), 826.
72. Yang, S.; Chen, G.; Ricciardulli, A. G.; Zhang, P.; Zhang, Z.; Shi, H.; Ma, J.; Zhang, J.; Blom, P. W. M.; Feng, X., *Angew. Chem. Int. Ed.* **2020,** *59* (1), 465.
73. Thurakkal, S.; Zhang, X. Y., *Mater. Chem. Front.* **2021,** *5* (6), 2824.
74. Hultgren, R.; Gingrich, N. S.; Warren, B. E., *J. Chem. Phys.* **1935,** *3* (6), 351.
75. Bagus, P. S.; Nelin, C. J.; Brundle, C. R., *J. Vac. Sci. Technol. A* **2023,** *41* (6), 068501.
76. Sexton, B. A.; Avery, N. R., *Surf. Sci.* **1983,** *129* (1), 21.
77. Alvaro, M.; García, H.; García, S.; Márquez, F.; Scaiano, J. C., *J. Phys. Chem. B* **1997,** *101* (16), 3043.
78. Sampanthar, J. T.; Neoh, K. G.; Ng, S. W.; Kang, E. T.; Tan, K. L., *Adv. Mater.* **2000,** *12* (20), 1536.
79. Wei, Z.; Shin, W.; Jiang, H.; Wu, X.; Stickle, W. F.; Chen, G.; Lu, J.; Alex Greaney, P.; Du, F.; Ji, X., *Nat. Commun.* **2019,** *10* (1), 3227.
80. Sarkar, I.; Guo, C.; Peng, C.; Wang, Y.; Li, Y.; Zhang, X., *Small* **2025**, 2410300.
81. Mashtalir, O.; Cook, K. M.; Mochalin, V. N.; Crowe, M.; Barsoum, M. W.; Gogotsi, Y., *J. Mater. Chem. A* **2014,** *2* (35), 14334.
82. Xia, F.; Lao, J.; Yu, R.; Sang, X.; Luo, J.; Li, Y.; Wu, J., *Nanoscale* **2019,** *11* (48), 23330.
83. Adomaviciute-Grabusove, S.; Popov, A.; Ramanavicius, S.; Sablinskas, V.; Shevchuk, K.; Gogotsi, O.; Baginskiy, I.; Gogotsi, Y.; Ramanavicius, A., *ACS nano* **2024,** *18* (20), 13184.
84. Alhabeb, M.; Maleski, K.; Anasori, B.; Lelyukh, P.; Clark, L.; Sin, S.; Gogotsi, Y., *Chem. Mater.* **2017,** *29* (18), 7633.

85. Zhang, Q.; Yan, L.; Yang, M.; Wu, G.; Hu, M.; Li, J.; Yuan, K.; Yang, X., *J. Phys. Chem. C* **2020,** *124* (11), 6441.
86. Hu, K.; McClements, D. J., *Food Hydrocoll.* **2015,** *44*, 101.
87. Berger, E.; Lv, Z.-P.; Komsa, H.-P., *J. Mater. Chem. C* **2023,** *11* (4), 1311.
88. Sarycheva, A.; Gogotsi, Y., *Chem. Mater.* **2020,** *32* (8), 3480.
89. Shevchuk, K.; Sarycheva, A.; Shuck, C. E.; Gogotsi, Y., *Chem. Mater.* **2023,** *35* (19), 8239.
90. Thurakkal, S.; Zhang, X., *Mater. Chem. Front.* **2022,** *6* (5), 561.
91. Lee, S.; Song, M.-K.; Zhang, X.; Suh, J. M.; Ryu, J.-E.; Kim, J., *Nano Letters* **2024,** *24* (30), 9117.
92. Vollmann, H.; Becker, H.; Corell, M.; Streeck, H., *Justus Liebigs Annalen der Chemie* **1937,** *531* (1), 1.
93. Oberender, F. G.; Dixon, J. A., *The Journal of Organic Chemistry* **2002,** *24* (9), 1226.
94. Cho, H.; Harvey, R. G., *Tetrahedron Letters* **1974,** *15* (16), 1491.
95. Giri, N. G.; Chauhan, S. M. S., *Catalysis Communications* **2009,** *10* (4), 383.
96. El-Assaad, T. H.; Parida, K. N.; Cesario, M. F.; McGrath, D. V., *Green Chemistry* **2020,** *22* (18), 5966.
97. Pedrón, M.; Legnani, L.; Chiacchio, M.-A.; Caramella, P.; Tejero, T.; Merino, P., *Beilstein Journal of Organic Chemistry* **2019,** *15*, 1552.
98. Schmidt, A.-K. C.; Stark, C. B. W., *Organic Letters* **2011,** *13* (16), 4164.
99. Hu, J.; Zhang, D.; Harris, F. W., *The Journal of Organic Chemistry* **2004,** *70* (2), 707.
100. Martín, V. S.; Palazón, J. M.; Rodríguez, C. M.; Nevill Jr, C. R.; Hutchinson, D. K., Ruthenium(VIII) Oxide. In *Encyclopedia of Reagents for Organic Synthesis*, 2013.
101. Carlsen, P. H. J.; Katsuki, T.; Martin, V. S.; Sharpless, K. B., *J. Org. Chem.* **1981,** *46* (19), 3936.
102. Ishiyama, T.; Takagi, J.; Hartwig, J. F.; Miyaura, N., *Angewandte Chemie International Edition* **2002,** *41* (16), 3056.
103. Li, H.; Colacot, T. J., Di-μ-methoxobis(1,5-cyclooctadiene)diiridium(I). In *Encyclopedia of Reagents for Organic Synthesis*, 2010.
104. Ueberricke, L.; Mizioch, D.; Ghalami, F.; Mildner, F.; Rominger, F.; Oeser, T.; Elstner, M.; Mastalerz, M., *European Journal of Organic Chemistry* **2021,** *2021* (34), 4816.
105. Liu, Y.; Chen, J.; Zhan, K.; Shen, Y.; Gao, H.; Yao, L., *RSC Advances* **2018,** *8* (62), 35453.
106. Okba, D.; Hassan, S.; Abdel Aleem, A. A. H.; Shehab El-din, M. T.; El Tantawy El Sayed, I.; Abou-Elyazed, A. S., *RSC Advances* **2025,** *15* (2), 795.
107. Sung, Y.-S.; Lin, L.-Y., *Journal of Energy Storage* **2021,** *37*, 102480.

Appendix: Experimental Section

(All the NMR spectra are in well accordance with data from literature unless otherwise stated)

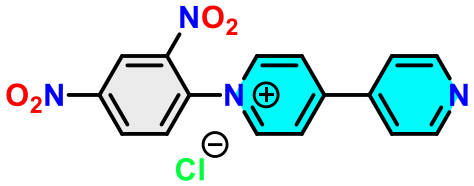

5

*Synthesis of compound **5**:* 2,4-dinitrochlorobenzene (1 g, 0.0049 mol) and 4,4'-bipyridine (848.2 mg, 0.0054 mol) were dissolved in ethanol (25 mL). The mixture was heated under reflux for 24 h. The hot mixture was filtered, and the filtered cake was washed with acetone (2 × 80 mL). The solvent was evaporated and the remaining solid was recrystallized from C_2H_5OH:ether (1:10). The compound was obtained as a brown solid. Yield: 25.3% (448 mg), ^1H NMR (600 MHz, D_2O, δ): 9.40 (d, 1H), 9.26 (d, 2H), 8.95 (dd, 1H), 8.86 (d, 2H), 8.70 (d, 2H), 8.29 (d, 1H), 8.06 (d, 2H).

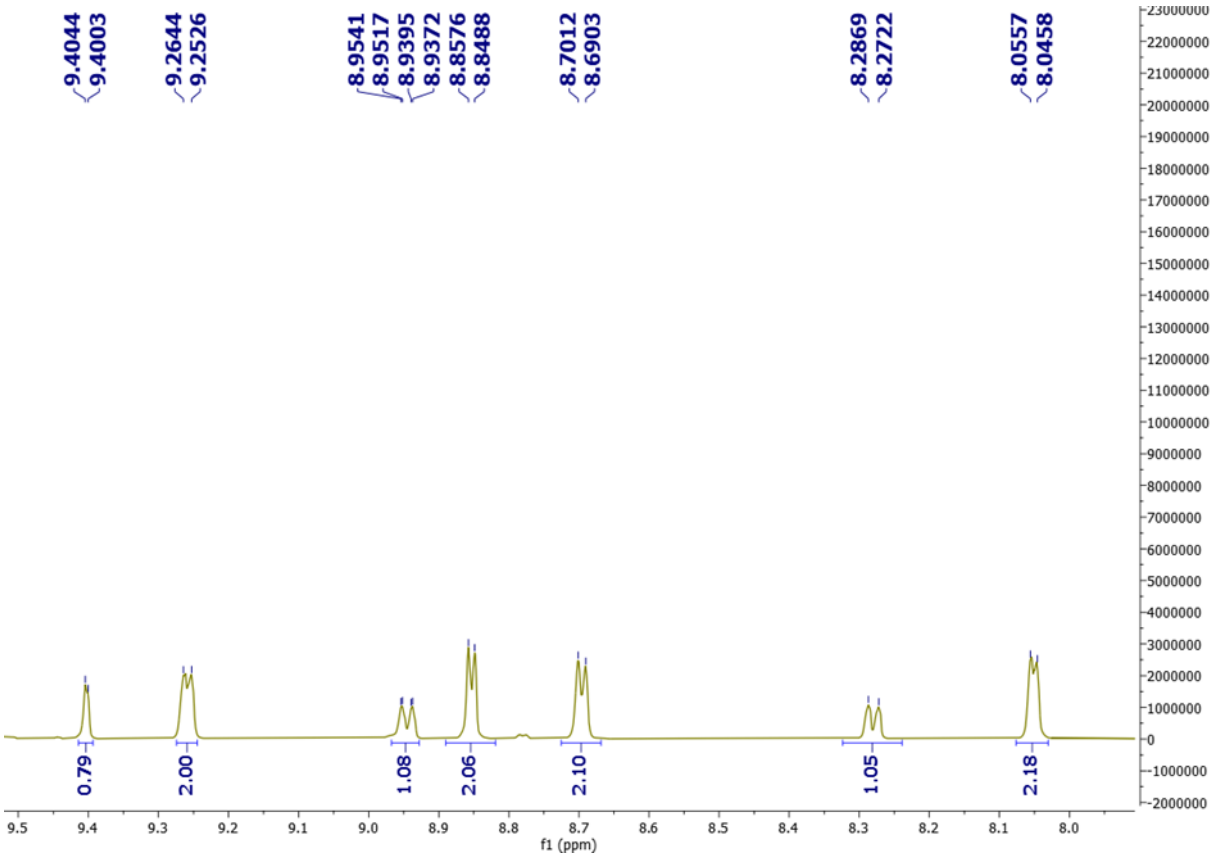

***Figure A 1** ^1H NMR spectrum of compound **5** (D_2O, 600 MHz).*

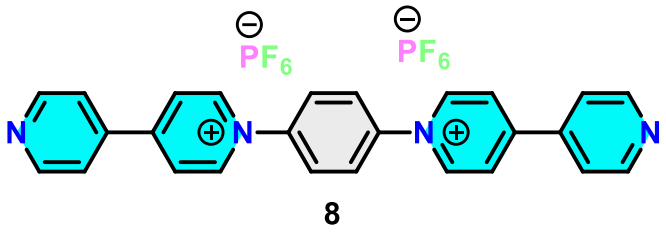

8

*Synthesis of compound **8**:* 1-(2,4-dinitrophenyl)-[4,4'-bipyridin]-1-ium chloride (447.6 mg, 1.249 mmol) and *p*-phenylenediamine (64.23 mg, 0.594 mmol) were dissolved in ethanol (15 mL). The mixture was heated under reflux for 72 h. The solvent was evaporated and the remaining solid was washed by acetone (200 mL). The filter cake was collected and dissolved in water and its hexafluorophosphate salt mixture was obtained by ion-exchange with NH_4PF_6 (excess). The pure compound was obtained as brown solid by recrystallization in MeCN/diethylether (1:3). Yield: 23.6% (91 mg), ^{1}H NMR (600 MHz, CD_3CN, δ): 9.11 (d, 4H), 8.93 (d, 4H), 8.58 (d, 4H), 8.12 (s, 4H), 7.93 (d, 4H).

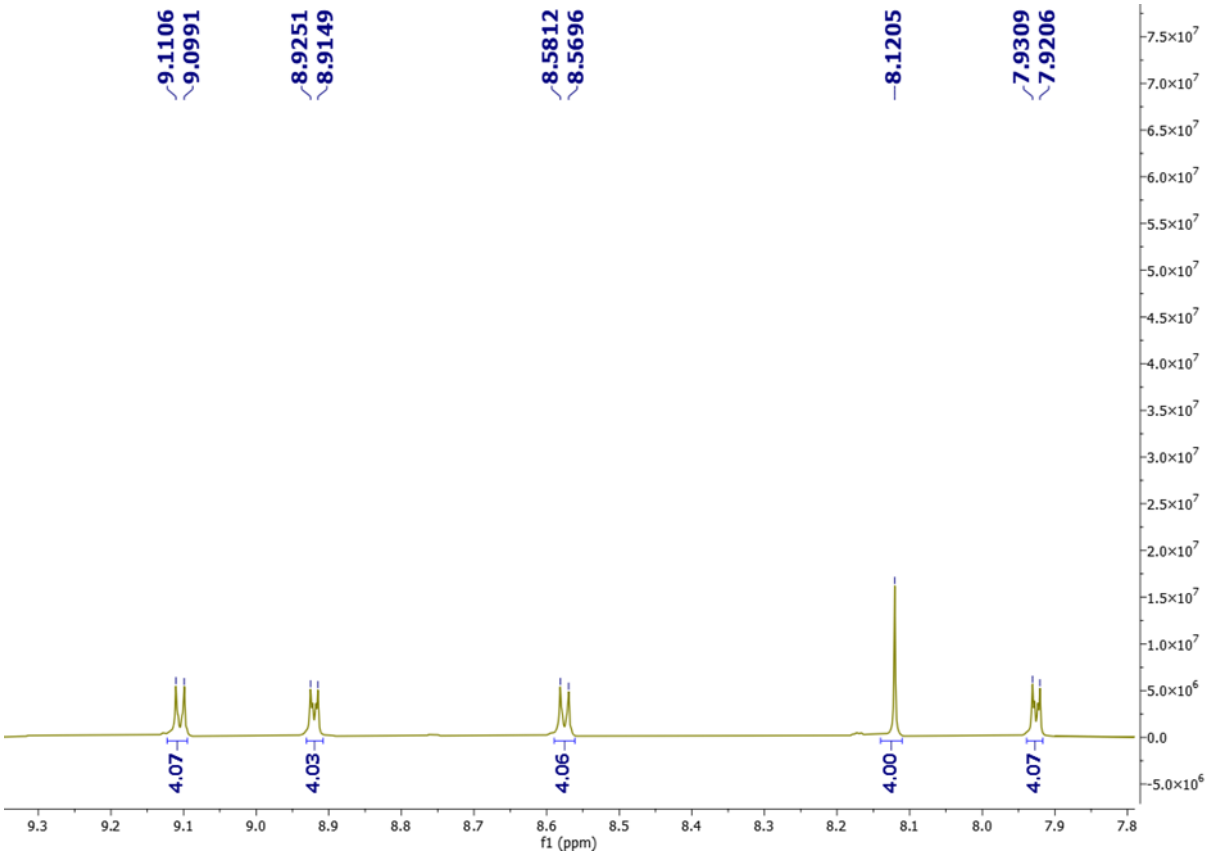

Figure A 2 *^{1}H NMR spectrum of compound **8** (CD_3CN, 600 MHz).*

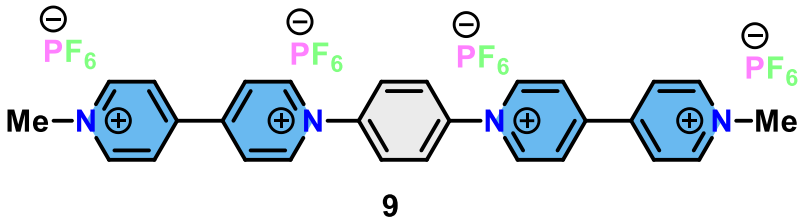

9

Synthesis of compound ***9****:* In a sealed tube, 1,1''-(1,4-phenylene)bis(([4,4'-bipyridin]-1-ium)) hexafluorophosphate (91 mg, 0.14 mmol) was dissolved in acetonitrile (5 ml) and to it methyl iodide (1 ml) was added. The mixture was heated to 80 °C and kept running overnight. The reaction was stopped afterwards, and the solvent evaporated. The solid obtained was dissolved into water and its hexafluorophosphate salt was obtained by ion-exchange with NH_4PF_6 (excess). Yield: 62.2% (87 mg), ^{1}H NMR (600 MHz, CD_3CN, δ): 9.25 (d, 4H), 8.92 (d, 4H), 8.66 (d, 4H), 8.50 (d, 4H), 8.17 (s, 4H), 4.45 (s, 6H).

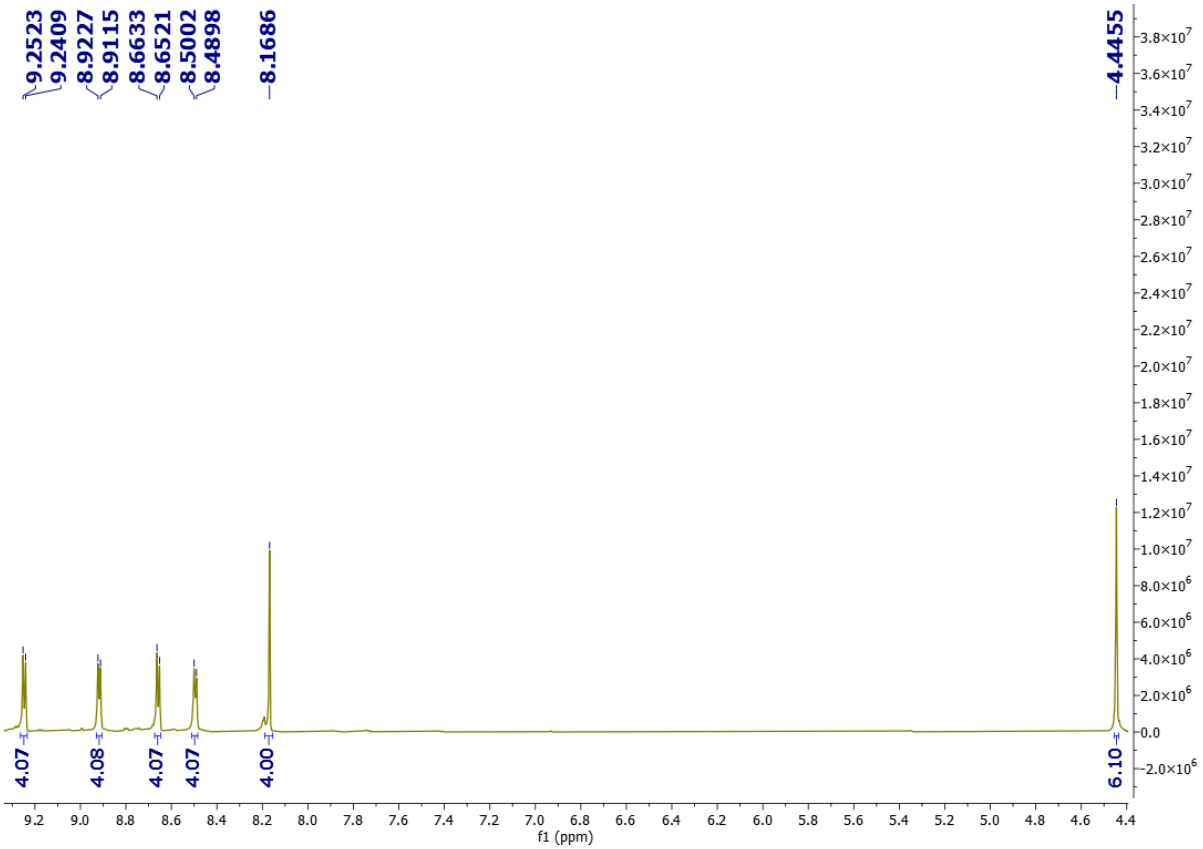

Figure A 3 *^{1}H NMR spectrum of compound* ***9*** *(CD_3CN, 600 MHz).*

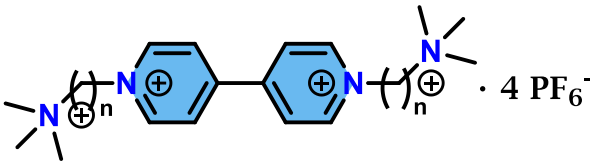

11a: n = 3
11b: n = 5

*Synthesis of compound **11a** and **11b**:* In a sealed tube, 4,4'-Bipyridine (100 mg) was dissolved in DMSO (4 ml) and to it bromoalkyltrimethylammonium bromide (**10a**: 334.2 mg, 2.4 eqv. or **10b**: 407.19 mg, 2.2 eqv.) was added and the mixture was heated at 80 °C overnight. The reaction was then stopped and to the mixture acetone was added. The precipitates were collected and washed several times with acetone and anion-exchange was performed using NH_4PF_6 (excess). Pure products were isolated as a white powder for **11a** and as red solid for **11b**. ^{1}H NMR of **11a** (600 MHz, CD_3CN, δ): 8.93 (d, 4H), 8.46 (d, 4H), 4.65 (t, 4H), 3,36 (t, 4H), 3.07 (s, 18H), 2.48 (m, 4H). ^{13}C NMR of **11a** (151 MHz, CD_3CN, δ): 151.46, 146.93, 128.51, 63.35, 59.28, 54.25, 25.53. ^{1}H NMR of **11b** (600 MHz, CD_3CN, δ): 8.91 (d, 4H), 8.41 (d, 4H), 4.64 (t, 4H), 3.21 (t, 4H), 3.02 (s, 18H), 2.01 (m, (7-3) H = 4H), 1.79 (m, 4H), 1.42 (m, 4H). ^{13}C NMR of **11b** (151 MHz, CD_3CN, δ): 151.08, 146.59, 128.28, 67.01, 62.59, 53.94, 53.89, 31.19, 23.14, 22.91.

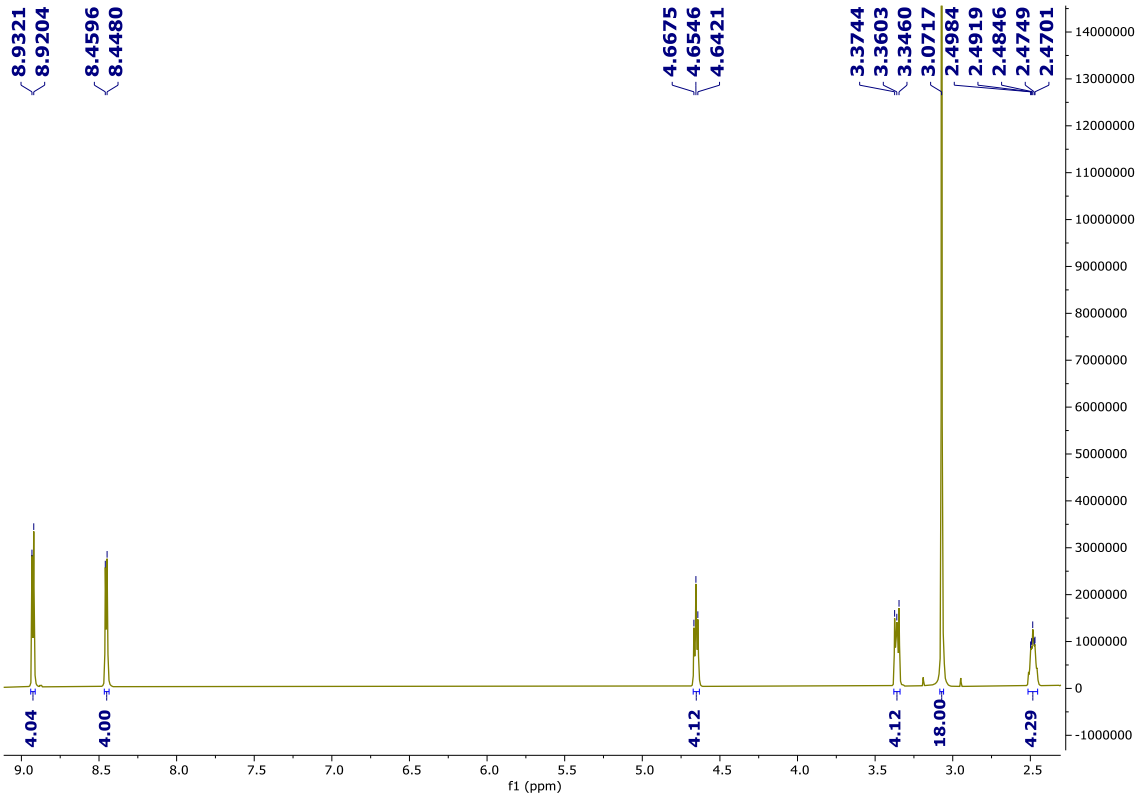

***Figure A 4** ^{1}H NMR spectrum of compound **11a** (CD_3CN, 600 MHz).*

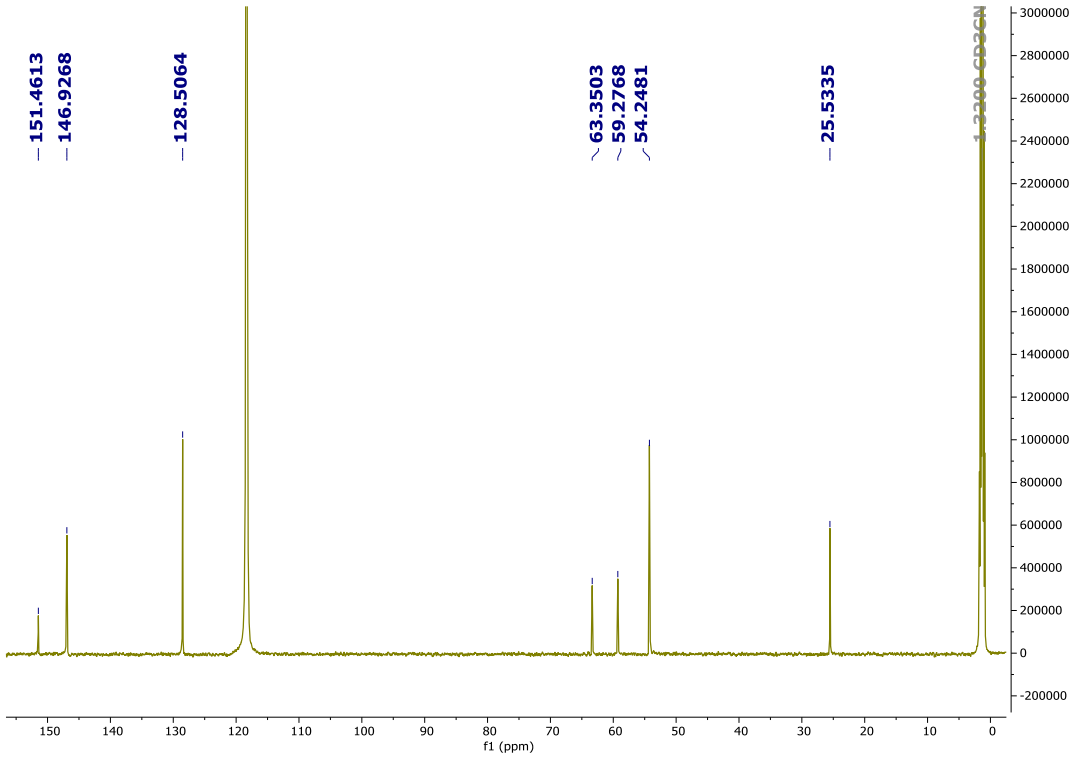

Figure A 5 *^{13}C NMR spectrum of compound* ***11a*** *(CD_3CN, 151 MHz).*

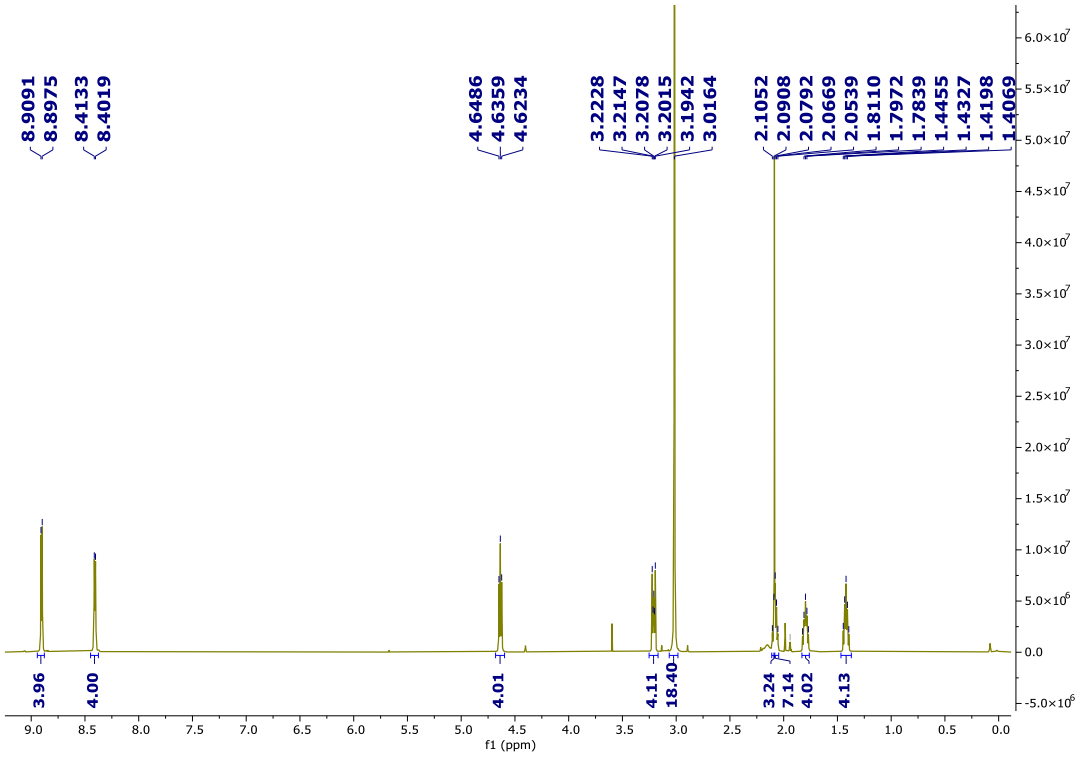

Figure A 6 *^{1}H NMR spectrum of compound* ***11b*** *(CD_3CN, 600 MHz).*

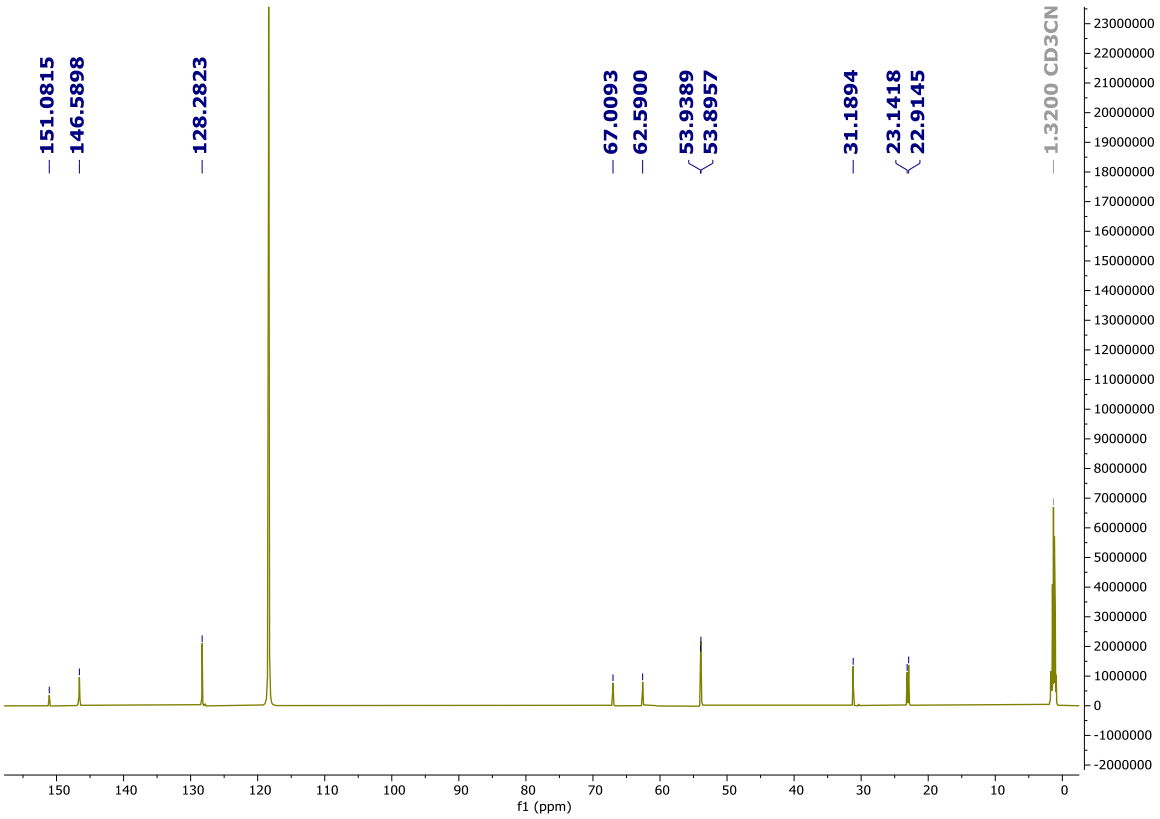

Figure A 7 *^{13}C NMR spectrum of compound* ***11b*** *(CD_3CN, 151 MHz).*

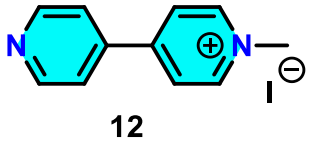

12

Synthesis of compound ***12****:* In a sealed tube, 4,4'-bipyridine (500 mg, 3.2 mmol, 1 eqv.) was dissolved in acetone (15 ml). To it, methyl iodide (0.4 ml, 6.43 mmol, 2 eqv.) was added. The mixture was stirred at room temperature for 24 hours. The precipitate was filtered, washed with acetone, and the filter cake was collected by redissolving it in methanol. Yield: 89.4% (853.11 mg), ^{1}H NMR (600 MHz, CD_3OD, δ): 9.04 (d, 2H), 8.84 (d, 2H), 8.51 (d, 2H), 7.99 (d, 2H), 4.47 (s, 3H).

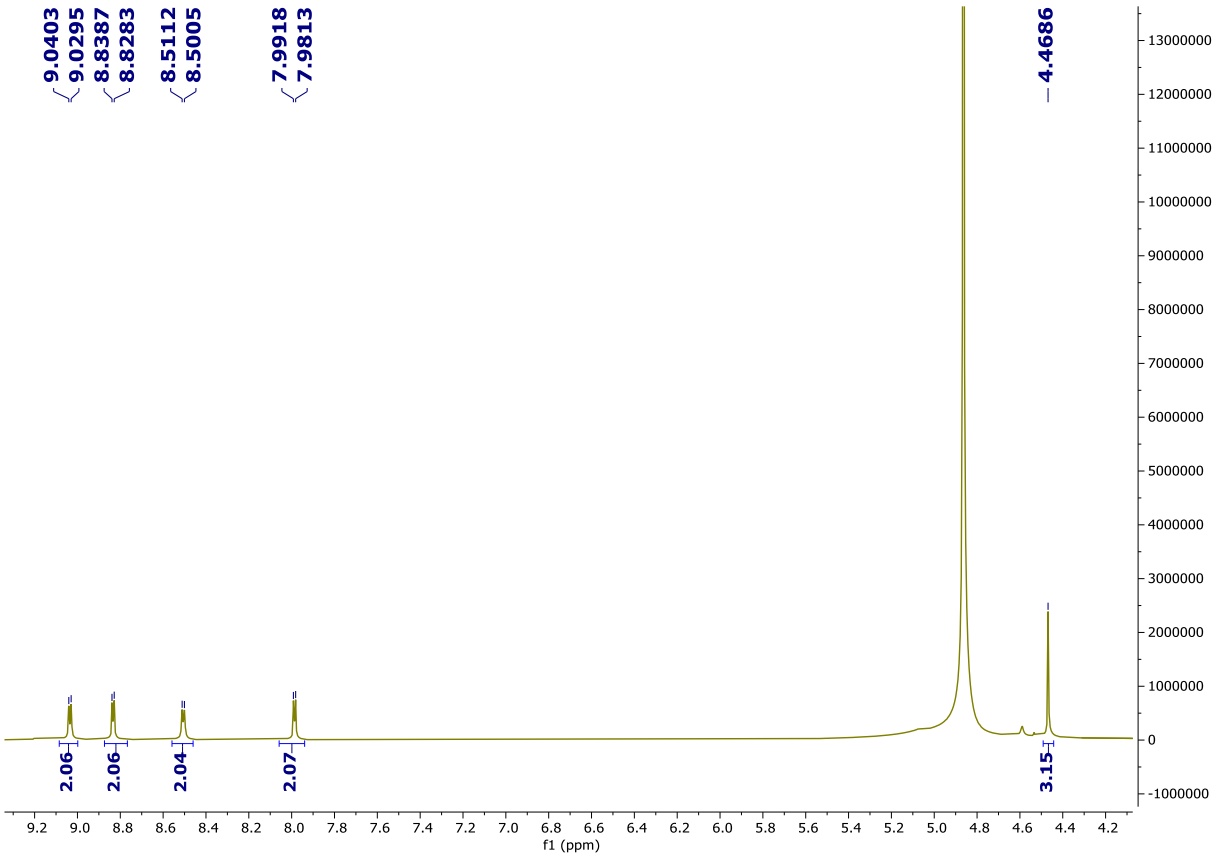

Figure A 8 *^{1}H NMR spectrum of compound* ***12*** *(CD_3OD, 600 MHz).*

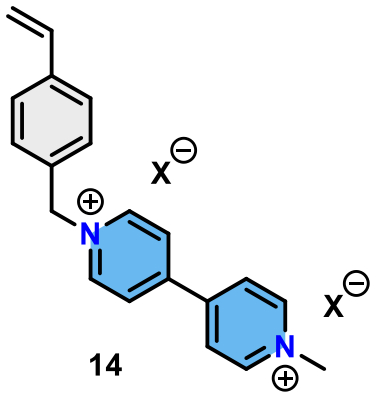

14

14a: X = PF_6
14b: X = Cl

Synthesis of compound ***14****:* In a capped vial, *N*-methyl-4,4'-bipyridinium iodide (500 mg, 1.68 mmol) was dissolved in DMSO (3 ml). To it, 4-vinylbenzylchloride (0.29 ml, apprx. 308 mg, 1.2 eqv) was added. The mixture was stirred at room temperature for 24 hours. To the mixture, acetonitrile (20 ml) was added. The orange solid was precipitated and collected by filtration. The filter cake was washed with acetonitrile and recollected using methanol. Yield: 50.9% (386.46 mg). The hexafluorophosphate salt derivative was obtained by ion-exchange with NH_4PF_6 (excess). The pure compound was obtained as white solid, ^{1}H NMR (600 MHz, CD_3OD, δ): 9.34 (d, 2H), 9.19 (d, 2H), 8.68 (d, 2H), 8.65 (d, 2H), 7.58

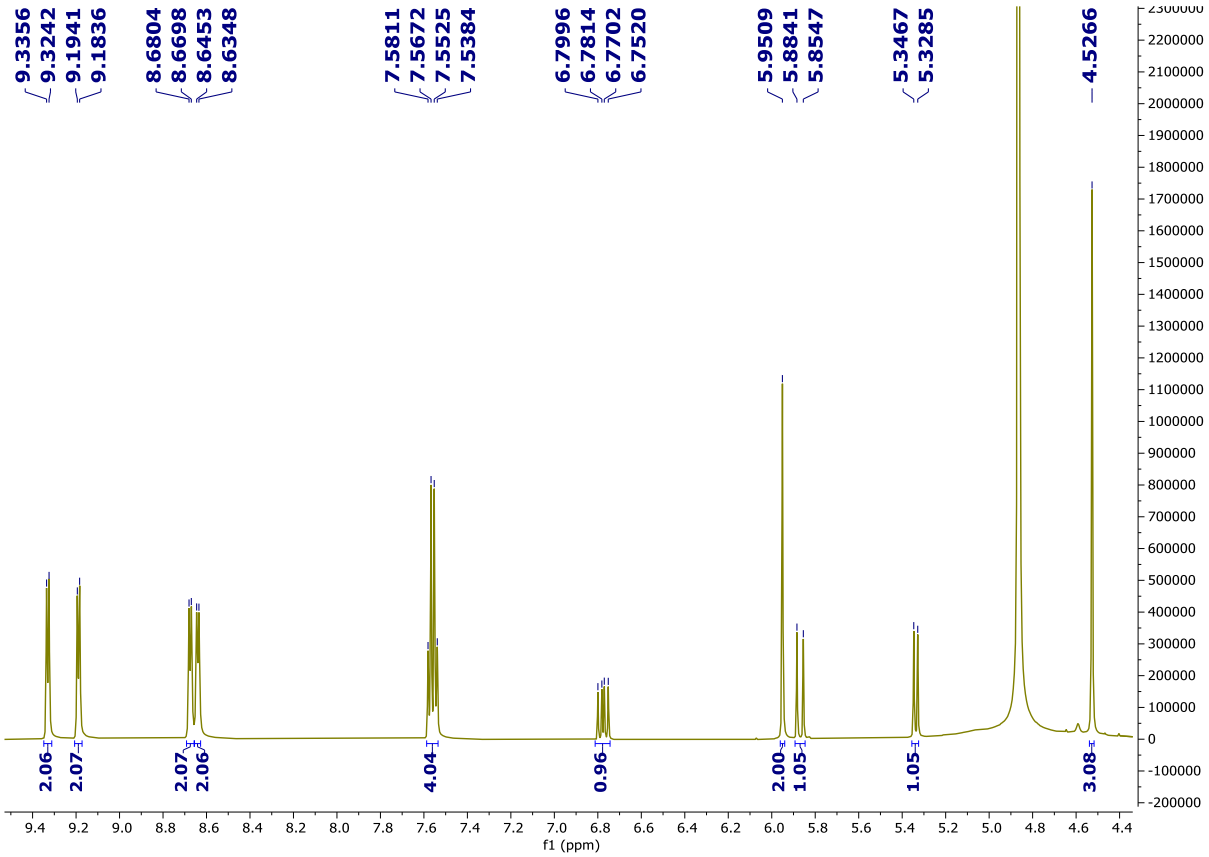

Figure A 9 *^{1}H NMR spectrum of compound* ***14*** *(CD_3OD, 600 MHz).*

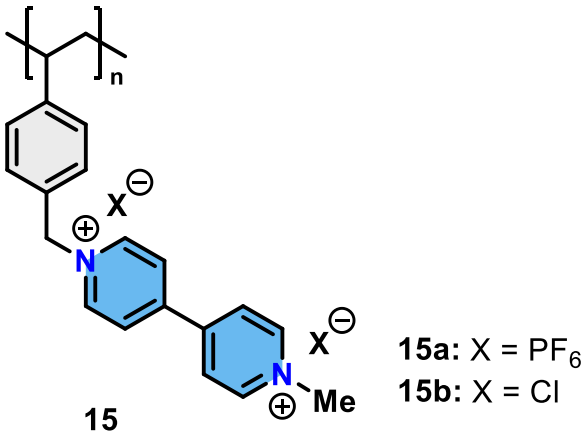

15

15a: X = PF_6
15b: X = Cl

Synthesis of compound ***15a****:* In a nitrogen-filled sealed tube, compound **14** (82.34 mg) was dissolved in DMSO (4 ml) and to it $K_2S_2O_8$ (15 mg) was added, and the mixture was heated to 80 °C overnight. The reaction was then stopped and to the mixture acetone was added. The precipitates were collected, redispersed in acetone by sonication and the solvent was removed by centrifugation. The washing step was repeated several times, and the solid was collected separately.

Synthesis of compound ***15b****:* Same as previous, with the starting material as **14b**.

SEC measurements for **15b** were done by our collaborator Giovanni Tizzanini from Anna Ström's group at Chalmers, some relevant experimental details are as follows:

Concentration: 2.000 mg/mL

Concentration Source: RI

Flow Rate: 0.500 mL/min

RI Instrument: Optilab T-rEX

Band Broadening Correction: Yes (Instrumental: 1.000 µL, Mixing: 50.000 µL)

Column: 13-7-MALS-RI 50C

Universal Calibration Function Fit Standard Error: 0

Conventional Calibration Function Fit Standard Error: 0.0383694

Calibration Technique: Conventional

Conventional Calibration Function:

$$M[v] = 10^{(11.78286185 - 0.4527392449v)}$$

Solvent: Water

Refractive Index: 1.327

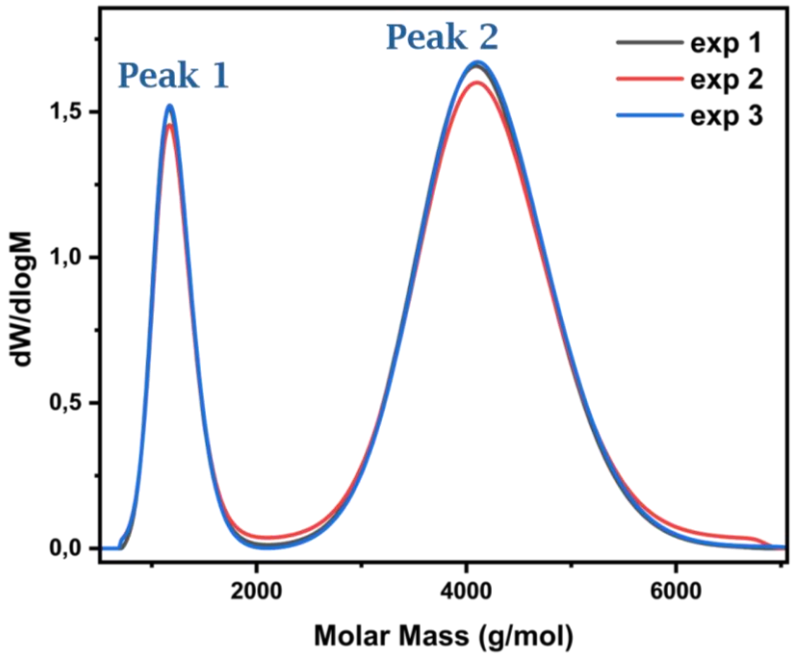

Figure A 10 *GPC measurements for oligomer-**15b**.*

Table A 1 *Molecular weight distribution for oligomer-**15b** (Averaged over 3 repetitions).*

	Peak 1	**Peak 2**
M_n	1167.67 ± 62.22	3988.33 ± 212.7
M_w	1199.33 ± 63.82	4094.67 ± 218.37
M_z	1232.67 ± 146.99	4199.00 ± 500.72
$M_{(avg)}$	985.97 ± 3.45	3341.33 ± 11.88
PDI: M_w/M_n	1.03 ± 0.08	1.03 ± 0.08
PDI: M_z/M_n	1.06 ± 0.13	1.05 ± 0.13

Table A 2 *Average number of monomer units in the oligomer-**15b** (Mw of monomer: 359.29).*

No. of Monomer unit	**Peak 1**	**Peak 2**
M_n	3.25 ± 0.17	11.10 ± 0.59
M_w	3.34 ± 0.18	11.40 ± 0.61
M_z	3.43 ± 0.41	11.69 ± 1.39
$M_{(avg)}$	2.74 ± 0.01	9.30 ± 0.03

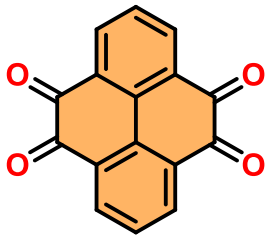

17

*Synthesis of compound **17**:* 2.2g (1.0 eq., 10 mmol) pyrene was dissolved in a mixture of 40 mL DCM and 40 mL acetonitrile in a 250 mL round bottom flask. Then 50 mL distilled water, 18.9 g (8.2 eq., 82 mmol) KIO_4, and 0.025g (1.2%, 0.12 mmol) $RuCl_3 \cdot xH_2O$ were added at 0 °C. The round bottom flask was kept at 50 °C after 3 mins stirring in an ice bath. The reaction was monitored by TLC every hour. Then 0.025 g $RuCl_3 \cdot xH_2O$ was added after 4 h. After 8 hours, 4.3 g $NaIO_4$ was added and stirred for 3.5 hours. The reaction mixture was poured into 200 mL of H_2O, and the solid filter-cake was removed by filtration. After the filter-cake was washed with excess of H_2O, the solid thus obtained was separated. The aqueous phase was extracted with DCM (3 × 50 mL) and the solvent was evaporated. The solid, thus obtained, was combined with the filter cake and column chromatography (DCM:Ethyl Acetate = 96:4) was performed to give pure product as bright orange crystals (Yield: 29%). ^1H NMR (600 MHz, $CDCl_3$, δ): 8.53 (d, 4H), 7.75 (t, 2H).

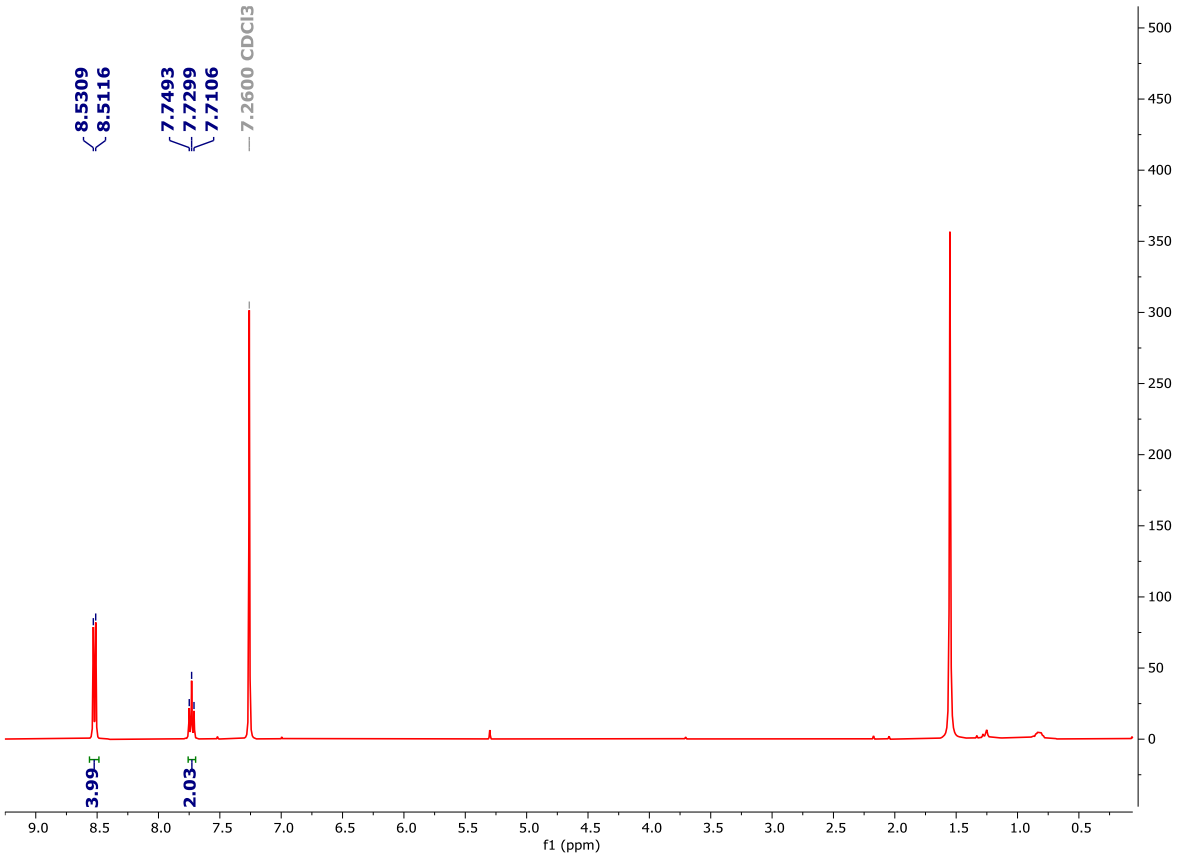

Figure A 11 *^{1}H NMR spectrum of compound* ***17*** *($CDCl_3$, 600 MHz).*

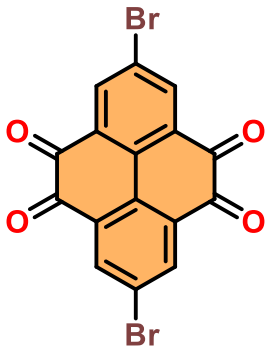

18

Synthesis of compound ***18****:* In an RB flask, compound **17** (101.79 mg, 0.572 mmol) and concentrated sulphuric acid (3 ml) was stirred for 5 minutes in an ice bath. To the mixture, NBS (145.1 mg, 1.2 mmol) was added and was stirred again for 5 minutes. The mixture was then heated to 50 °C for 2 hours. Upon completion the mixture was dumped into ice cold water, and the resultant precipitate was then collected by filtration, and the filter cake was washed several times with DI water. The filter cake was then collected by dispersing in methanol and the solvent was then evaporated using rotary evaporator. The di-bromo derivative was isolated using column chromatography (DCM:ethyl acetate = 99:1) as a pale-yellow solid (yield: 42%). ^{1}H NMR (600 MHz, $CDCl_3$, δ): 8.6 (s, 4H).

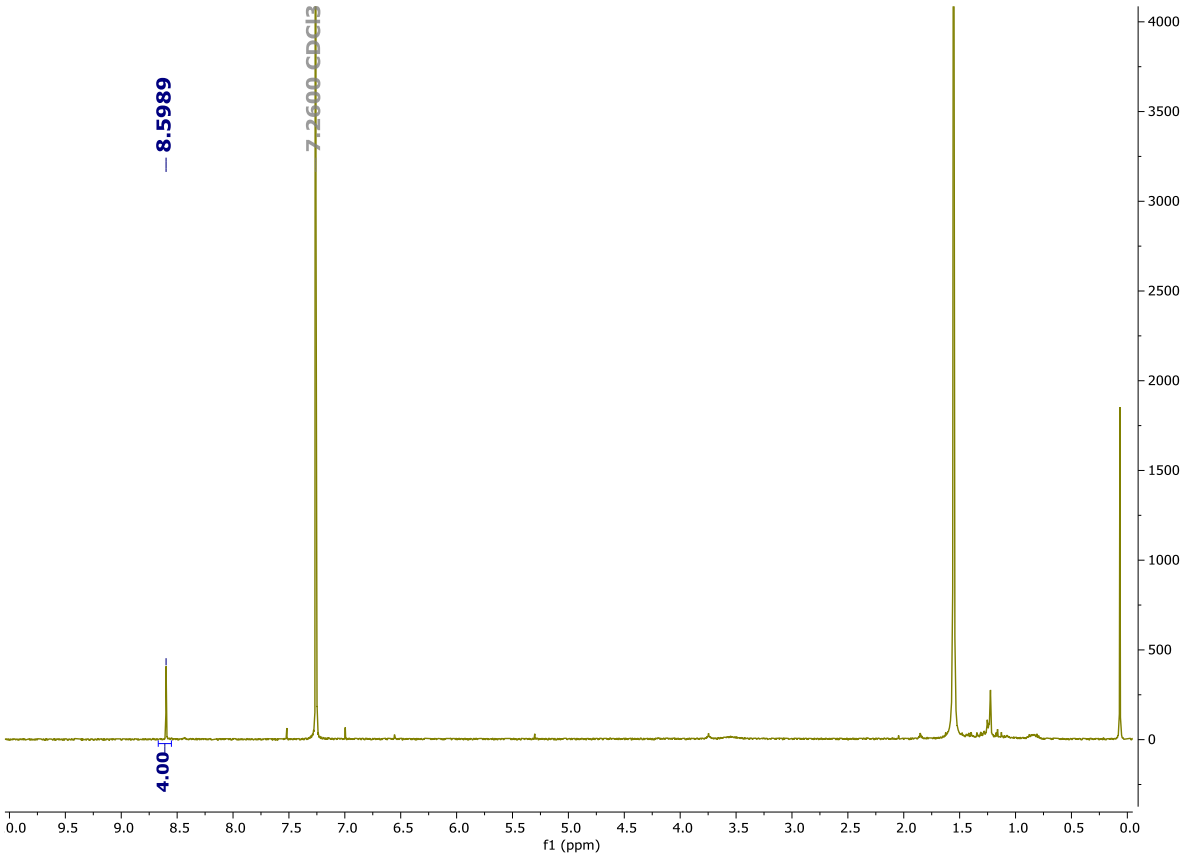

Figure A 12 *^{1}H NMR spectrum of compound* ***18*** *($CDCl_3$, 600 MHz).*

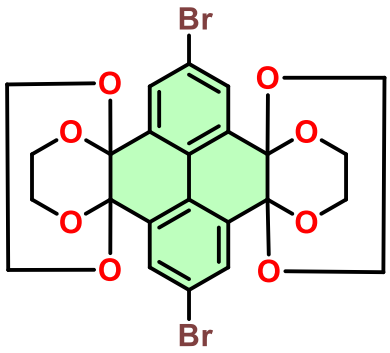

19

Synthesis of compound ***19****:* Compound **18** (63 mg, 0.15 mmol) and TsOH.H_2O (57 mg, 0.3 mmol) were added into a flask with a mixed solution of ethylene glycol (3 mL) and toluene (10 ml). The resulting mixture was refluxed at 110 °C under argon protection for 18 hrs. After the solution cooled down to room temperature, the solvent evaporated, and excess water was added to the mixture. Afterwards thus formed, was washed with excess of H_2O and with MeOH afterwards, dried to obtain off-white solid (56 mg, 63%).^{1}H NMR (600 MHz, $CDCl_3$, δ): 8.6 (s, 4H), 4.21 (br, 8H), 3.67 (br, 8H).

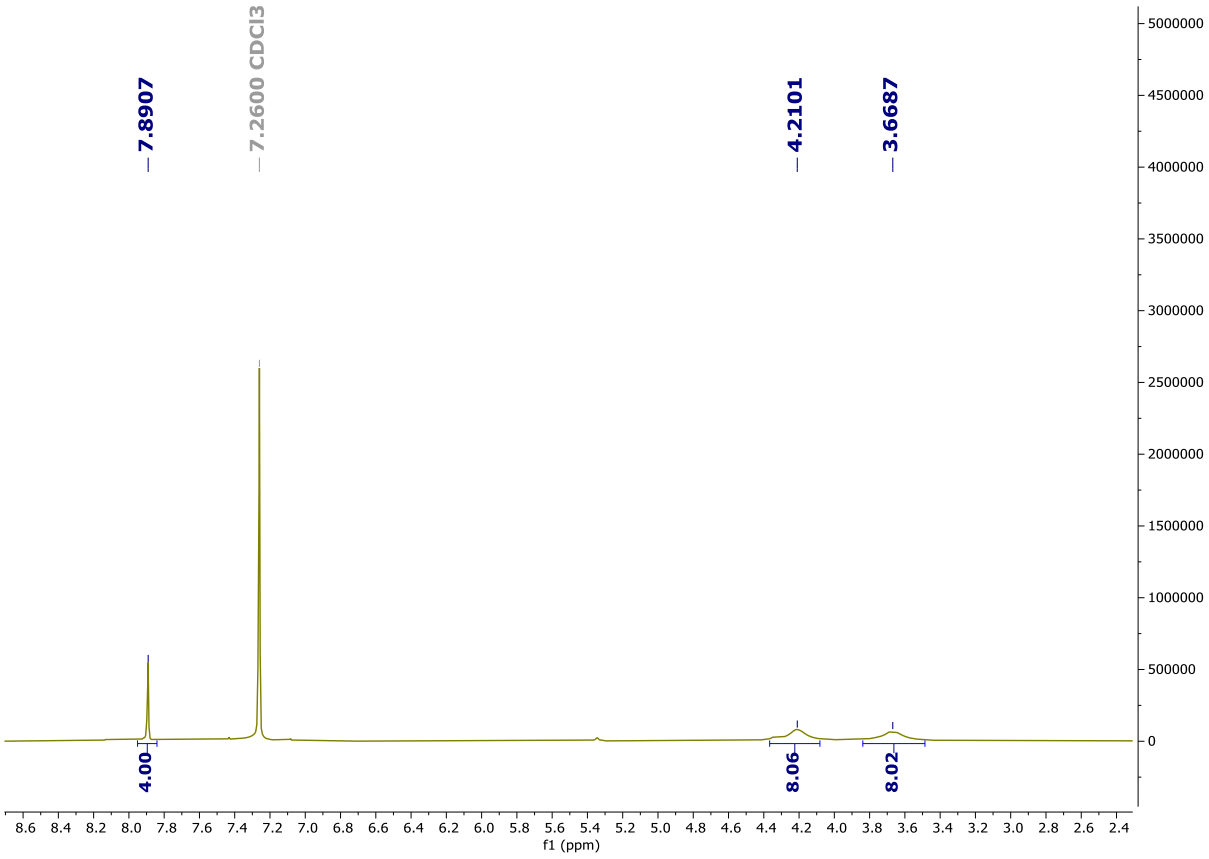

Figure A 13 *^{1}H NMR spectrum of compound **19** ($CDCl_3$, 600 MHz).*

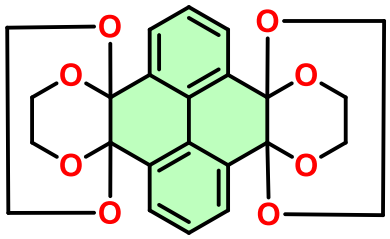

20

*Synthesis of compound **20**:* Compound **17** (3.12 g, 11.9 mmol, 1.00 eq) was suspended in toluene (400 mL) in a round-bottom flask equipped with a reflux condenser. Ethylene glycol (166 mL, 2.96 mol, 249 eq) and p-toluenesulphonic acid (2.04 g, 10.7 mmol, 0.90 eq) were then added, and the mixture was heated at reflux (125 °C) for 20 h. After cooling, toluene was removed in rota-vap, and water (400 mL) was added to the residue. The resulting crude solid was collected by filtration, washed with water, and purified by washing with methanol to afford compound **20** as a white solid. ^{1}H NMR (600 MHz, $CDCl_3$, δ): 7.77 (d, *J* = 7.7 Hz, 4H), 7.50 (t, *J* = 7.7 Hz, 2H), 4.20 (s, 8H), 3.68 (s, 8H).

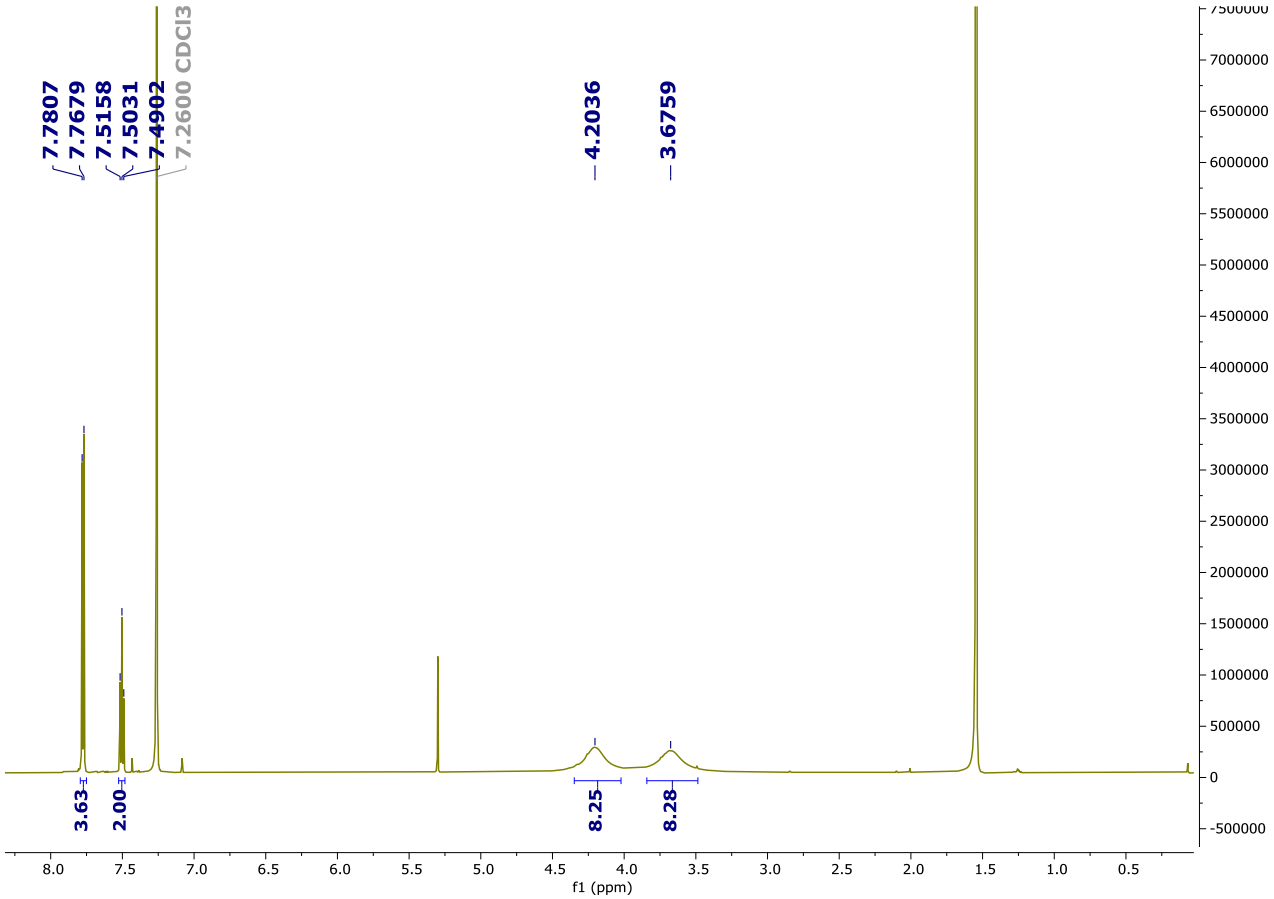

Figure A 14 *^{1}H NMR spectrum of compound* ***20*** *($CDCl_3$, 600 MHz).*

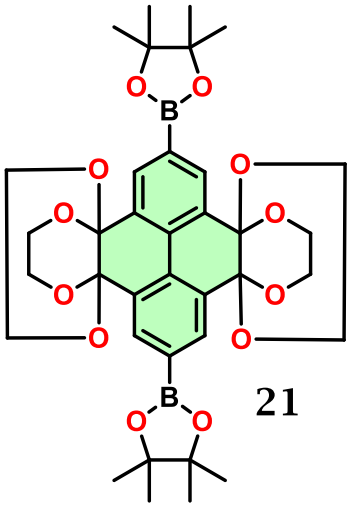

Synthesis of compound ***21****:* In a Young's tube, compound **20** (73.7 mg, 0.1682 mmol, 1 equiv.), 4,4'-di-tert-butyl-2,2'-dipyridine (dtbpy) (4.52 mg, 0.0168 mmol, 0.1 equiv.), B_2pin_2 (170.8 mg, 0.673 mmol, 4 equiv.), $[Ir(COD)(OMe)]_2$ (5.58 mg, 0.0084 mmol, 0.05 equiv.) was added sequentially inside a glovebox. 2ml of dry THF was added to the mixture and was stirred in room temperature until the colour of the solution becomes bright red. After that the mixture was kept in 70 °C for 19 hrs. When the reaction was over the solvent was evaporated and was replaced with dioxane and was kept in the refrigerator for a while until precipitate appeared. The precipitate was then filtered, and the filter cake was then collected by

dissolving everything in DCM. Total 53.35 mg (46%) of products were received. ^{1}H NMR (600 MHz, $CDCl_3$, δ): 8.21 (s, 4H), 4.22 (s, 8H), 3.70 (s, 8H), 1.32 (s, 24H).

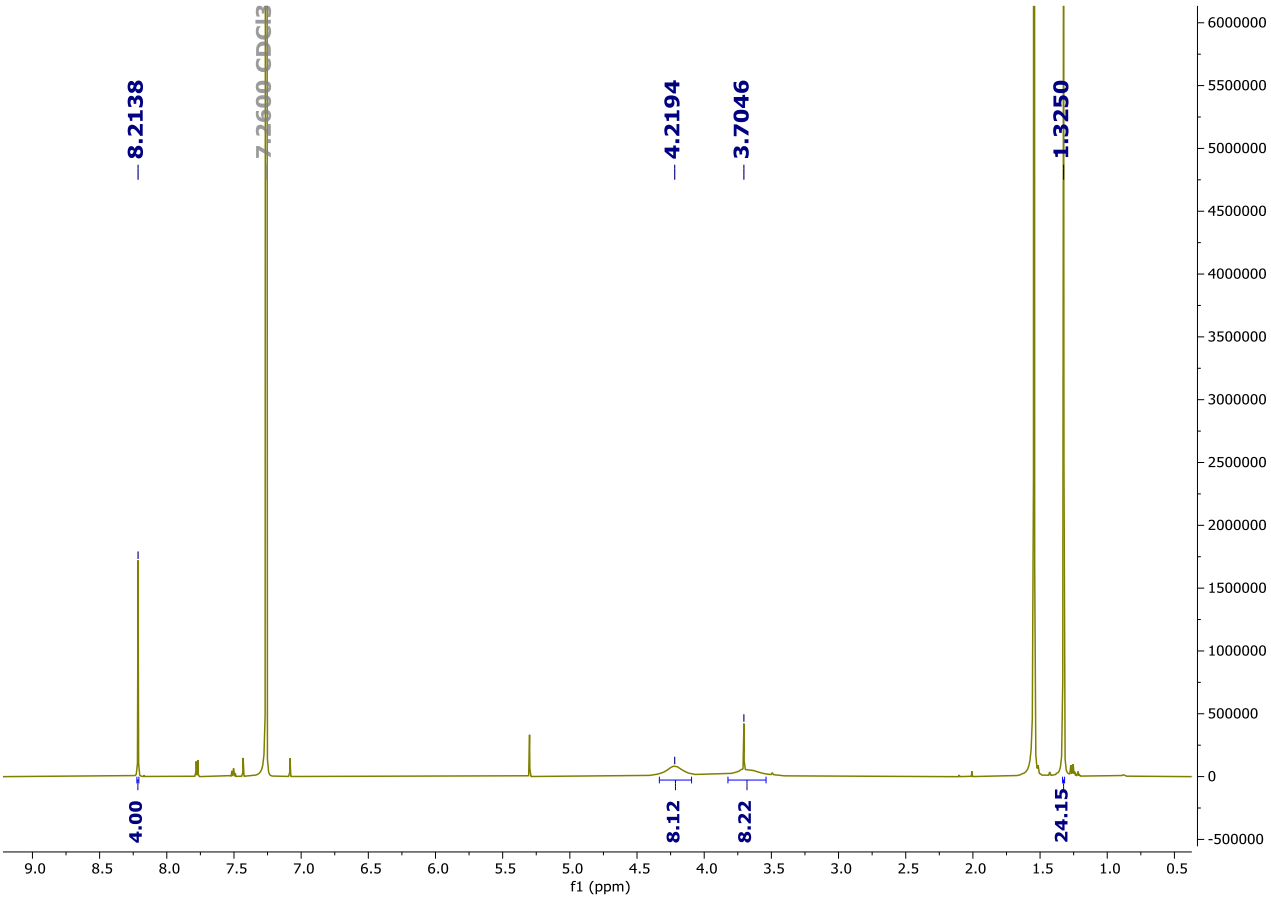

Figure A 15 *^{1}H NMR spectrum of compound **21** ($CDCl_3$, 600 MHz).*

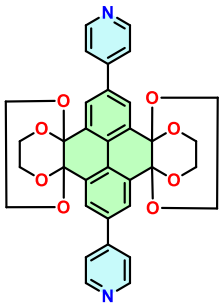

22

*Synthesis of compound **22** (Path A):* A sealed tube was charged with compound **19** (82 mg, 120 µmol) pyridinyl-4-boronic acid (76 mg, 350 µmol) was added as a solution in THF (2 mL), followed by aqueous 1M Cs_2CO_3 solution (2 mL) under N_2 atmosphere. While stirring Xphos-Pd-G2 (3 mg, 3.6 µmol) was added. The mixture was stirred vigorously at 85 °C for 17 h. The reaction mixture was cooled down to room temperature and was extracted with ethyl acetate (4×5 mL). The combined organic phases were dried over Na_2SO_4, and the solvents were removed under reduced pressure. The crude product was purified by preparative TLC (PE:DCM:MeOH = 10:9:1) to obtain the product as a white solid. ^{1}H NMR of **21** (600 MHz, CD_3CN, δ): 8.72 (d, 4H), 8.1 (s, 4H), 7.64 (d, 4H), 4.27 (br, 8H), 3.72 (br, 8H). ^{13}C NMR of **21** (151 MHz, CD_3CN, δ): 150.6, 147.3, 139.7, 134.4, 129.5, 125.8, 121.7, 92.6.

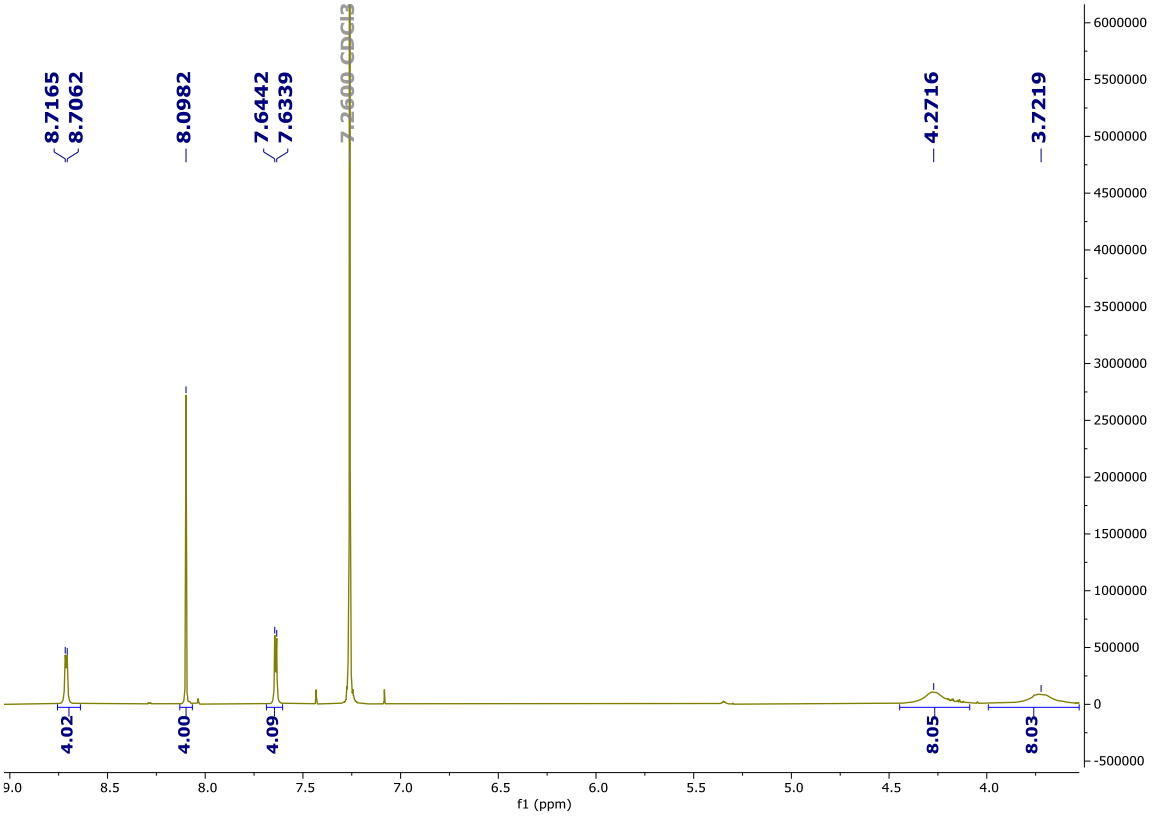

Figure A 16 *^{1}H NMR spectrum of compound* ***22*** *($CDCl_3$, 600 MHz).*

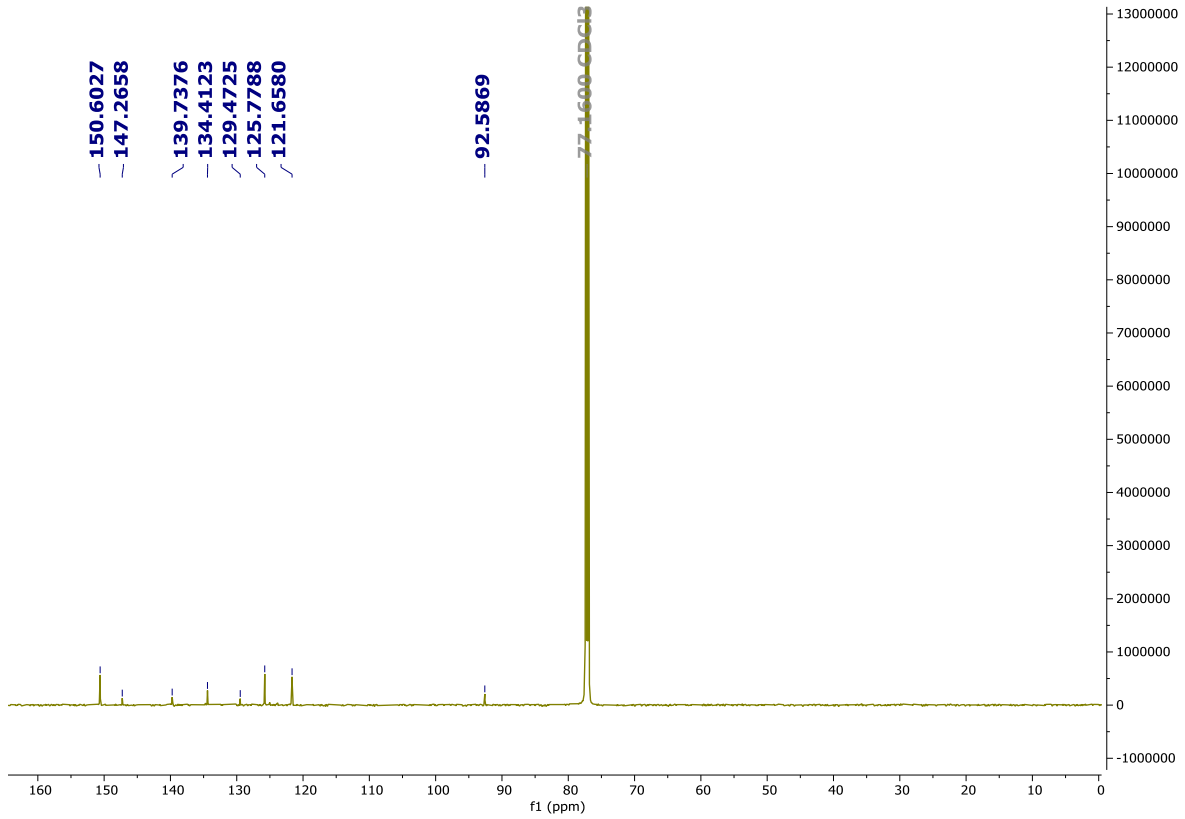

Figure A 17 *^{13}C NMR spectrum of compound **22** ($CDCl_3$, 151 MHz).*

*Synthesis of compound **22** (Path B):* A sealed tube was filled with **21** (24.57 mg, 0.036 mmol, 1.00 equiv), 4-bromopyridine.HCl salt (17.6 mg, 0.09 mmol, 2.5 equiv) and Xphos-Pd-G2 (5 mg, excess-calculated according to Pyr-Br) and the tube was evacuated and flushed with nitrogen. To it, 1M Cs_2CO_3 (2ml, degassed) and 2 mL of THF (anhydrous) was added. The reaction mixture was stirred at 70 °C for 18 h. The reaction was then stopped and the THF was evaporated using rotary evaporator. The remaining water and solid was extracted using DCM and brine until no blue colour could be seen for the DCM layer under UV. The organic layer was all collected as one fraction and was washed with $MgSO_4$ (anhyd.) to get rid of remining water. DCM was evaporated and the crude solid was obtained. TLC was performed to check conversion. Most of the reactant stayed unreacted most likely due to bulky groups around the -BPin groups in compound **21**. ^{1}H NMR (600 MHz, $CDCl_3$, δ): 8.72 (s, 4H), 8.11 (s, 4H), 7.67 (s, 4H), 4.43 – 4.13 (s, 8H), 3.90 – 3.57 (s, 8H).

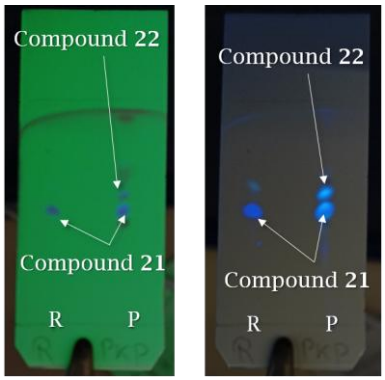

5% MeOH in DCM

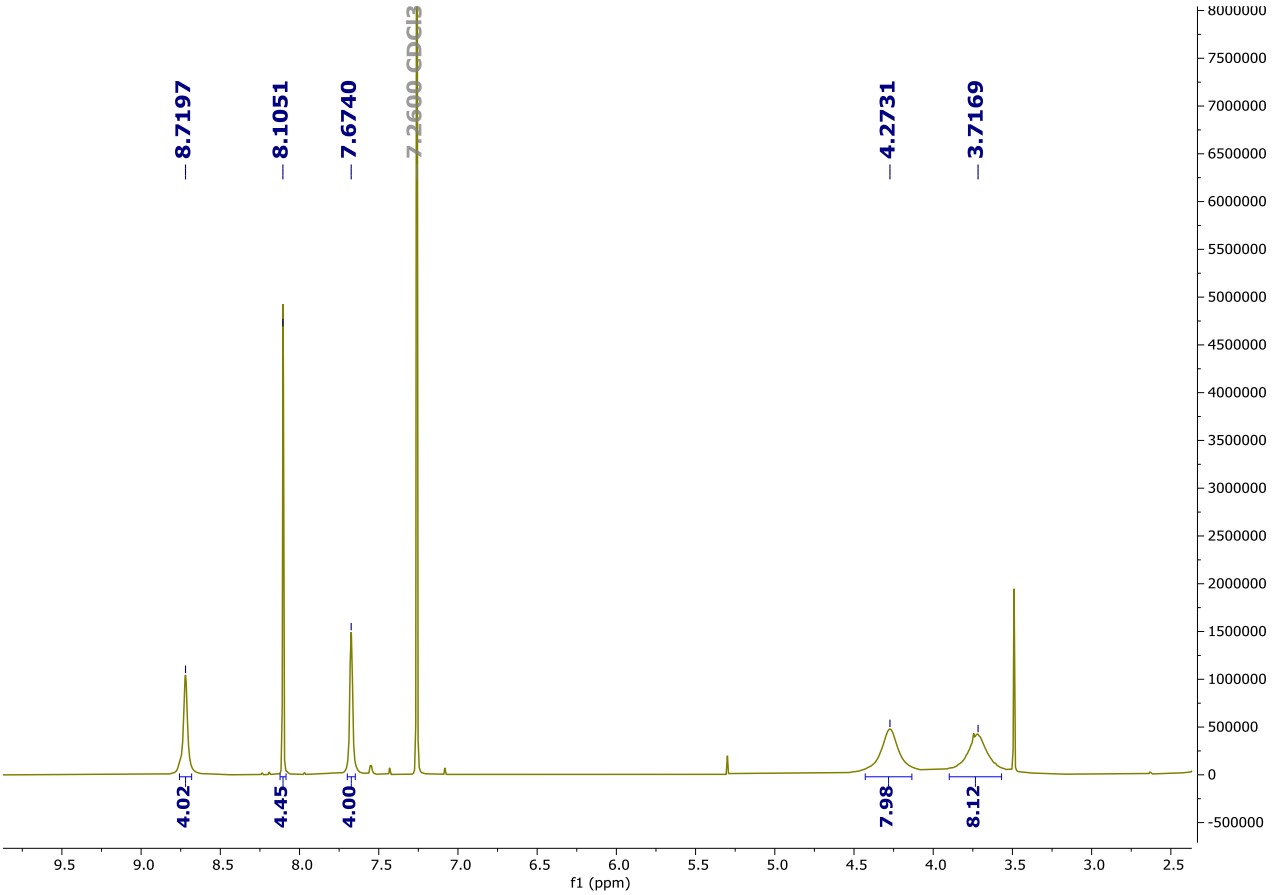

Figure A 18 *^{1}H NMR spectrum of compound **23** ($CDCl_3$, 600 MHz).*

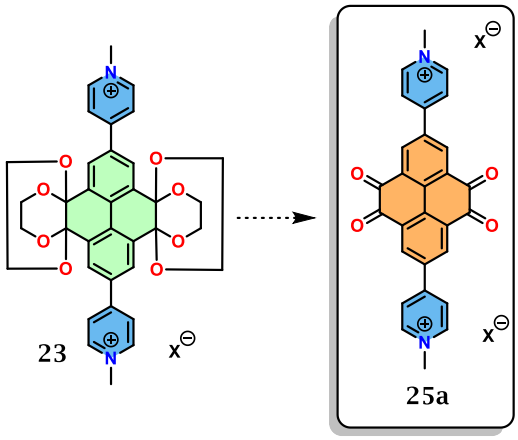

*Synthesis of compound **25a** (Path C):* A sealed tube was charged with compound **22** (19 mg, 32 µmol) methyl iodide (0.3 ml) was added in 4 ml of dioxane. The mixture was stirred vigorously at 80 °C overnight. The reaction mixture was cooled down to room temperature, and the solvent was evaporated under rota-vap. The solid thus obtained (**23**) was dispersed in 0.2 ml water and to it 1.8 ml of TFA was added (TFA:water = 9:1). The mixture was then sealed and stirred at 72 °C. The mixture was dumped into ice-water to obtain the product as an orange solid. ^{1}H NMR of **23** (400 MHz, DMSO, δ): 9.05 (d, *J* = 6.5 Hz, 4H), 8.67 (d, *J* = 7.0 Hz, 4H), 8.31 (s, 4H), 4.39 (s, 6H), 4.21 (s, 8H), 3.66 (s, 8H). ^{1}H NMR of **25a–TFA$_2$** (400 MHz, CD_3OD, δ): 9.00 (d, 4H), 8.87 (s, 4H), 8.69 (d, 4H), 4.75 (s, 6H). ^{13}C NMR **25a–TFA$_2$** (101 MHz, CD_3OD, δ): 158.18, 146.86, 136.67, 133.66, 128.31, 126.82, 118.49, 117.25,

66.40, 30.67, 24.21. ^{19}F NMR of **25a-TFA$_2$** (376 MHz, CD_3OD, δ): −77.3. The final product **25a**, however, has some extra unexplainable peaks and ^{13}C is very weak. Further work needs to be done.

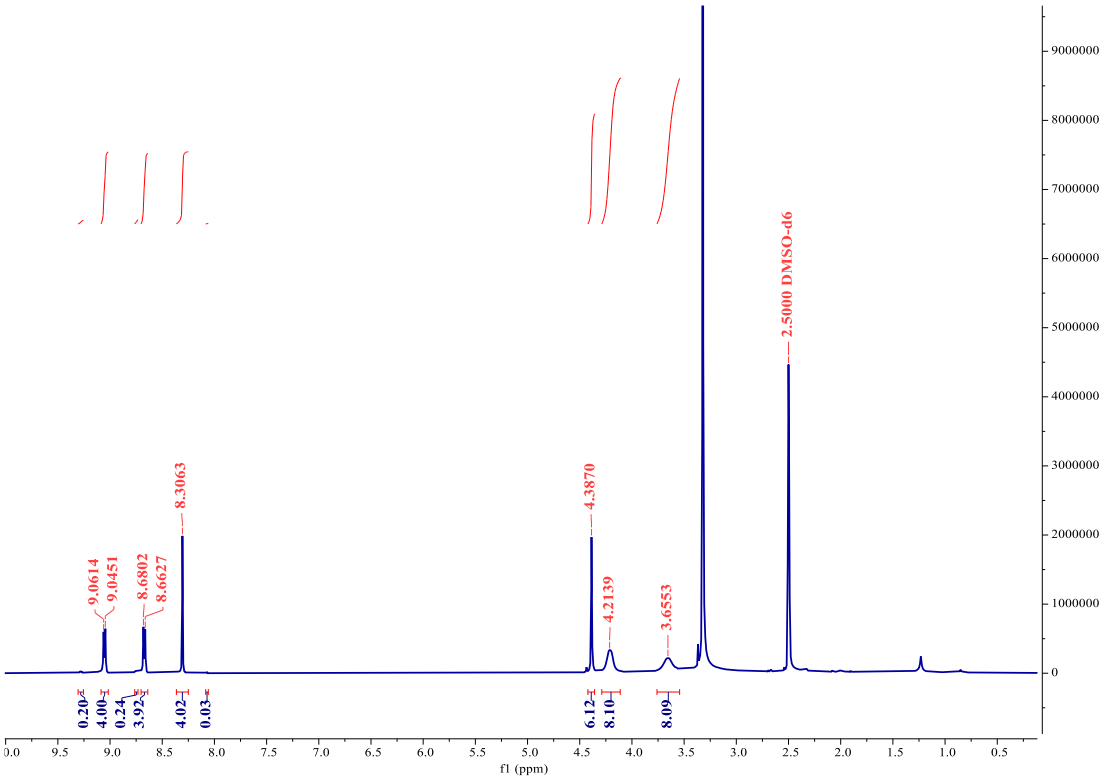

Figure A 19 *^{1}H NMR spectrum of compound **23** (CD_3OD, 400 MHz).*

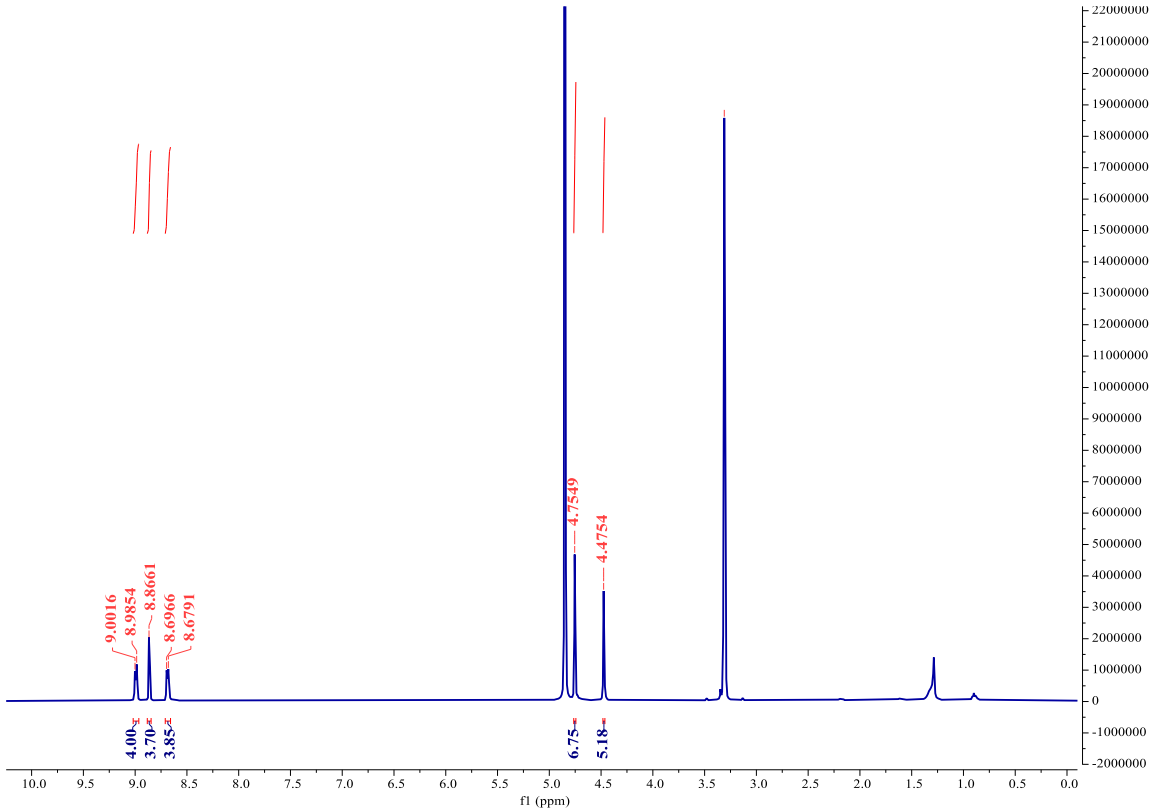

Figure A 20 *^{1}H NMR spectrum of compound* ***25a*** *(CD_3OD, 400 MHz). One peak between 4.4 – 4.8 ppm is unexplainable; hence, the structure cannot be confirmed.*

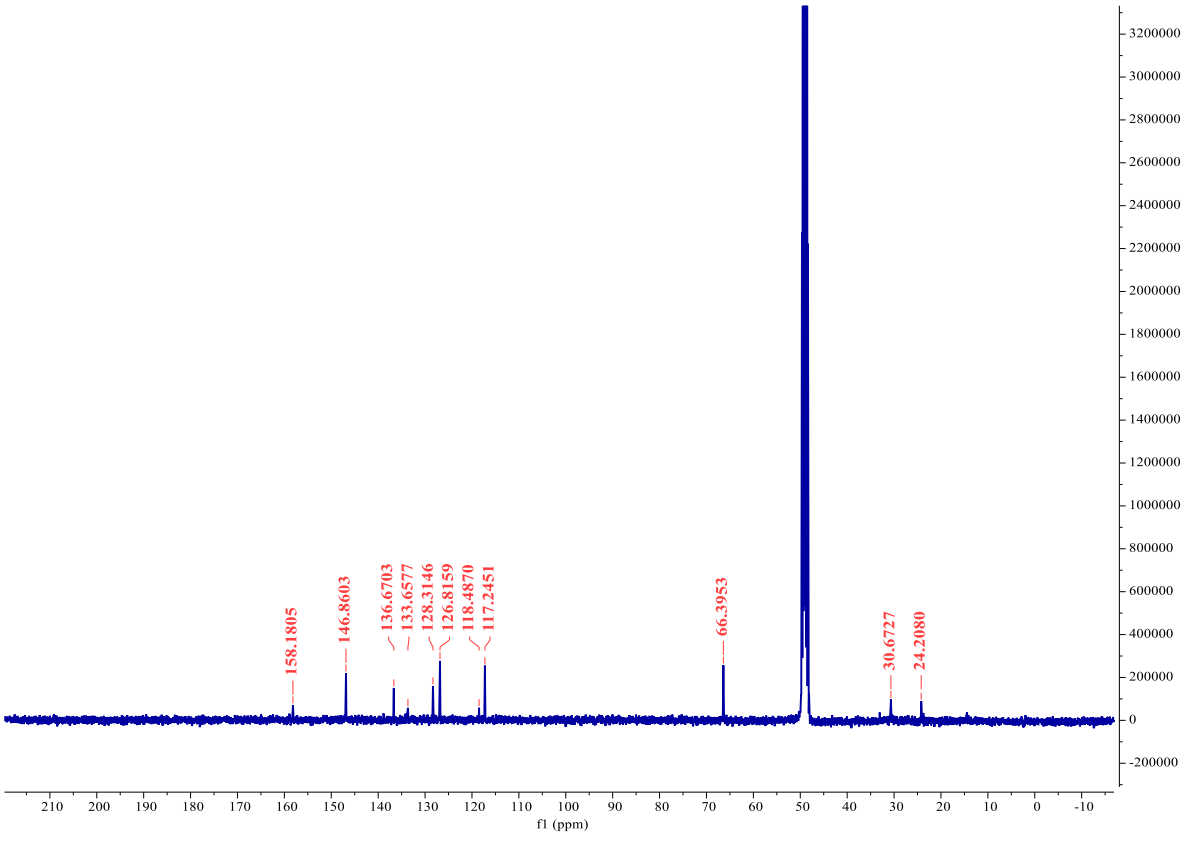

Figure A 21 *^{13}C NMR spectrum of compound* ***25a*** *(CD_3OD, 101 MHz).*

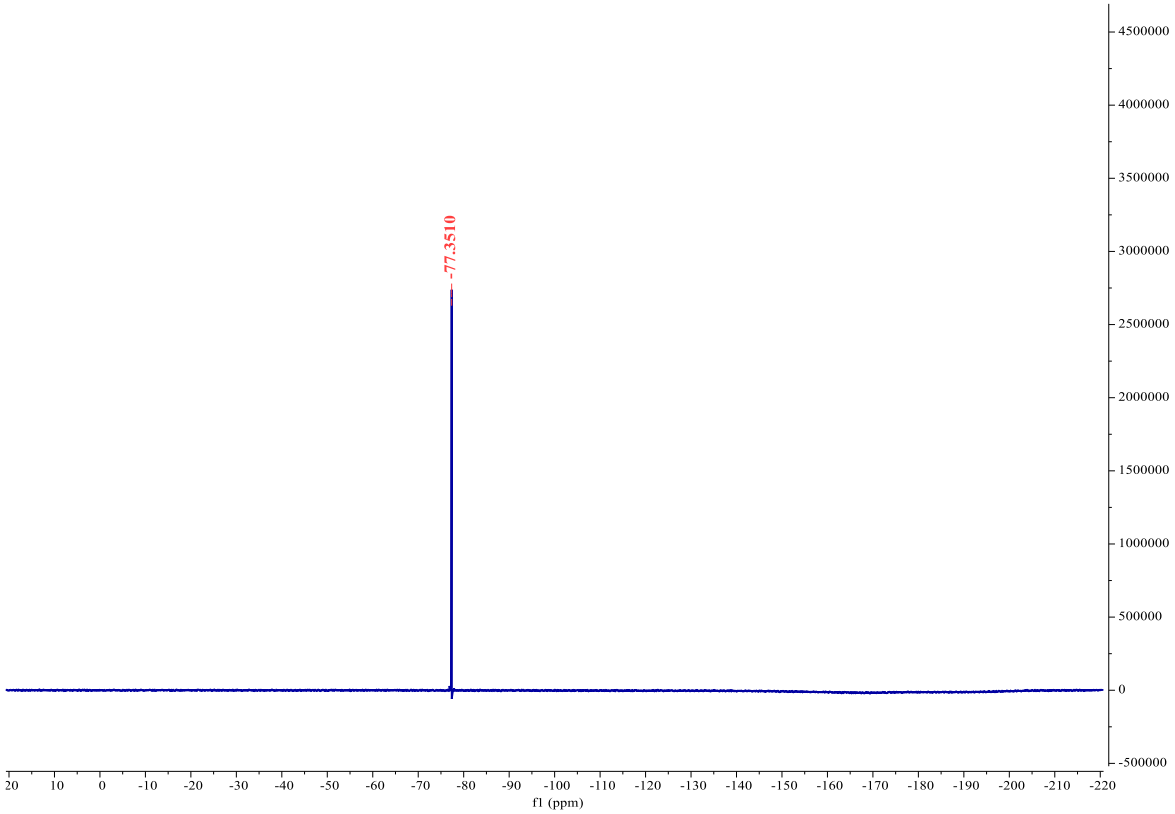

Figure A 22 *^{19}F NMR spectrum of compound* ***25a*** *(CD_3OD, 376 MHz).*

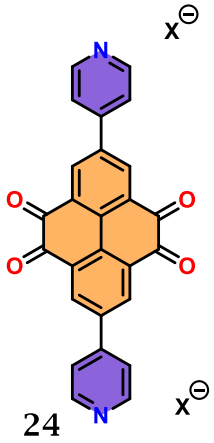

24

Synthesis of compound ***24*** *(Path C): Compound* **22** (10 mg) was dispersed in 0.2 ml water and to it 1.8 ml of TFA was added (TFA:water = 9:1). The mixture was then sealed and stirred at 72 °C. The mixture was dumped into ice-water, and the precipitate was collected as a red solid. However, the amount of the product was very small and very close detection limit for the NMR. Further work needs to be done.

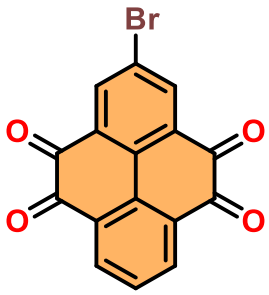

26

Synthesis of compound ***26***: Around 2 mL of concentrated sulfuric acid (98%) was added to a 25 mL round bottom flask. Then, 60 mg (0.23 mmol) of compound **17** and mg of N-bromosuccinimide (44.79 mmol, 1.1 eqv) were added to the reaction. The reaction mixture was stirred at room temperature for 1 h, after which the temperature was raised to 50 °C in an oil bath and allowed to react for an additional 2 hours. Subsequently, the mixture was poured into 20 mL of ice water. The crude product was then dried under vacuum and purified using column chromatography and reprecipitated from EA and pet-ether. ^{1}H NMR (400 MHz, $CDCl_3$, δ): 8.60 (s, 2H), 8.52 (d, *J* = 7.8 Hz, 2H), 7.75 (t, *J* = 7.8 Hz, 1H).

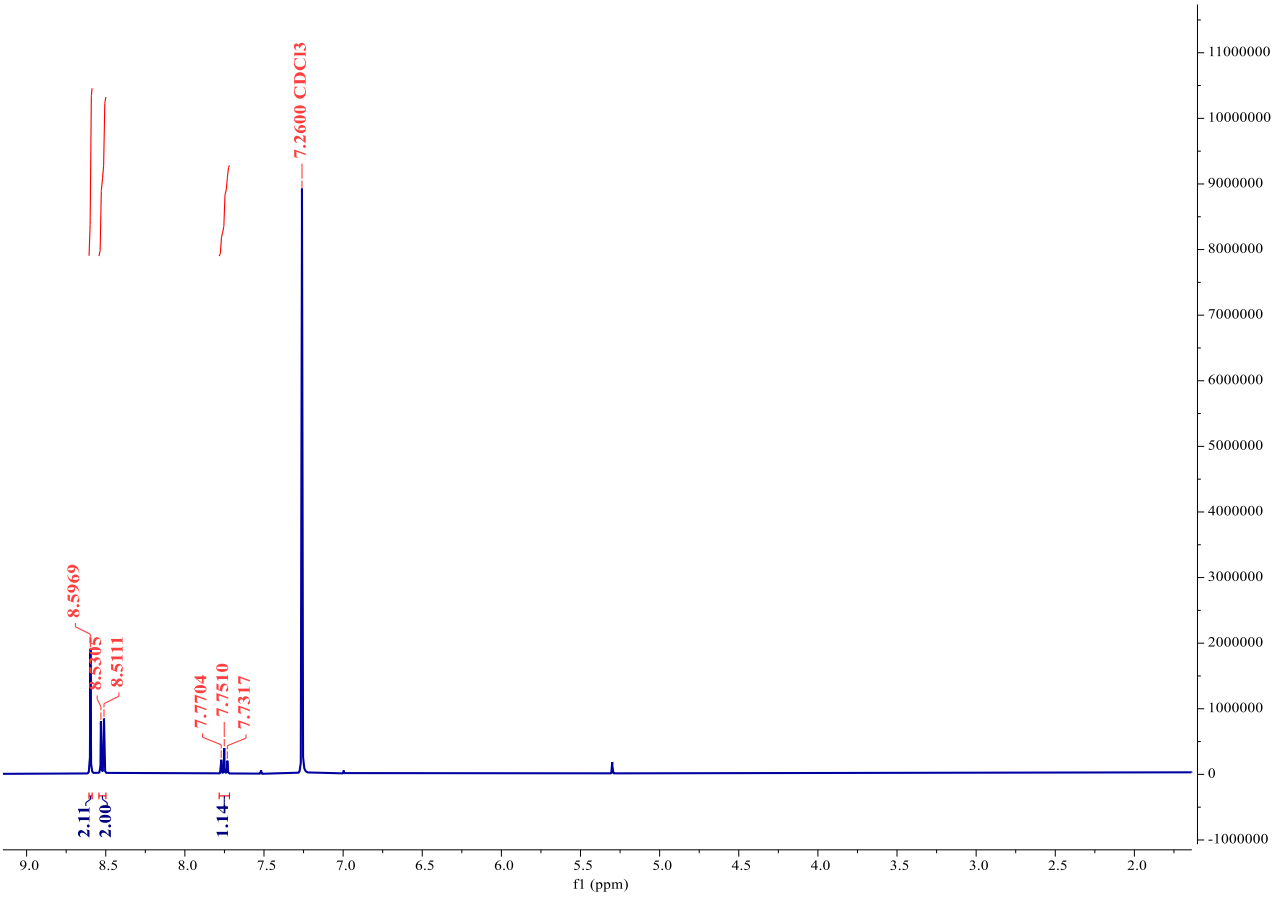

Figure A 23 *^{1}H NMR spectrum of compound* ***26*** *($CDCl_3$, 400 MHz).*

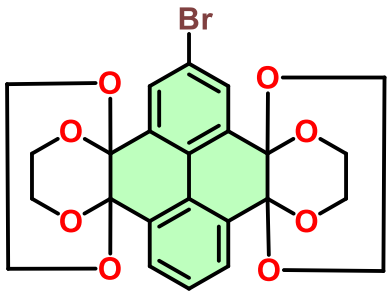

27

Synthesis of compound ***27***: In 15 mL of toluene, compound **26** (25 mg) was added. Then, 15 mg of p-toluenesulphonic acid and 0.5 ml of ethylene glycol were added to the reaction. The reaction mixture was refluxed in an oil bath and allowed to react overnight. Subsequently, the solvent was evaporated and to the remaining liquid, excess water was added. The precipitate was washed with methanol, and the solid was then dried under vacuum overnight. ^{1}H NMR (400 MHz, $CDCl_3$, δ): 7.90 (s, 2H), 7.77 (d, *J* = 7.7 Hz, 2H), 7.52 (t, *J* = 7.7 Hz, 1H), 4.21 (s, 8H), 3.67 (s, 8H).

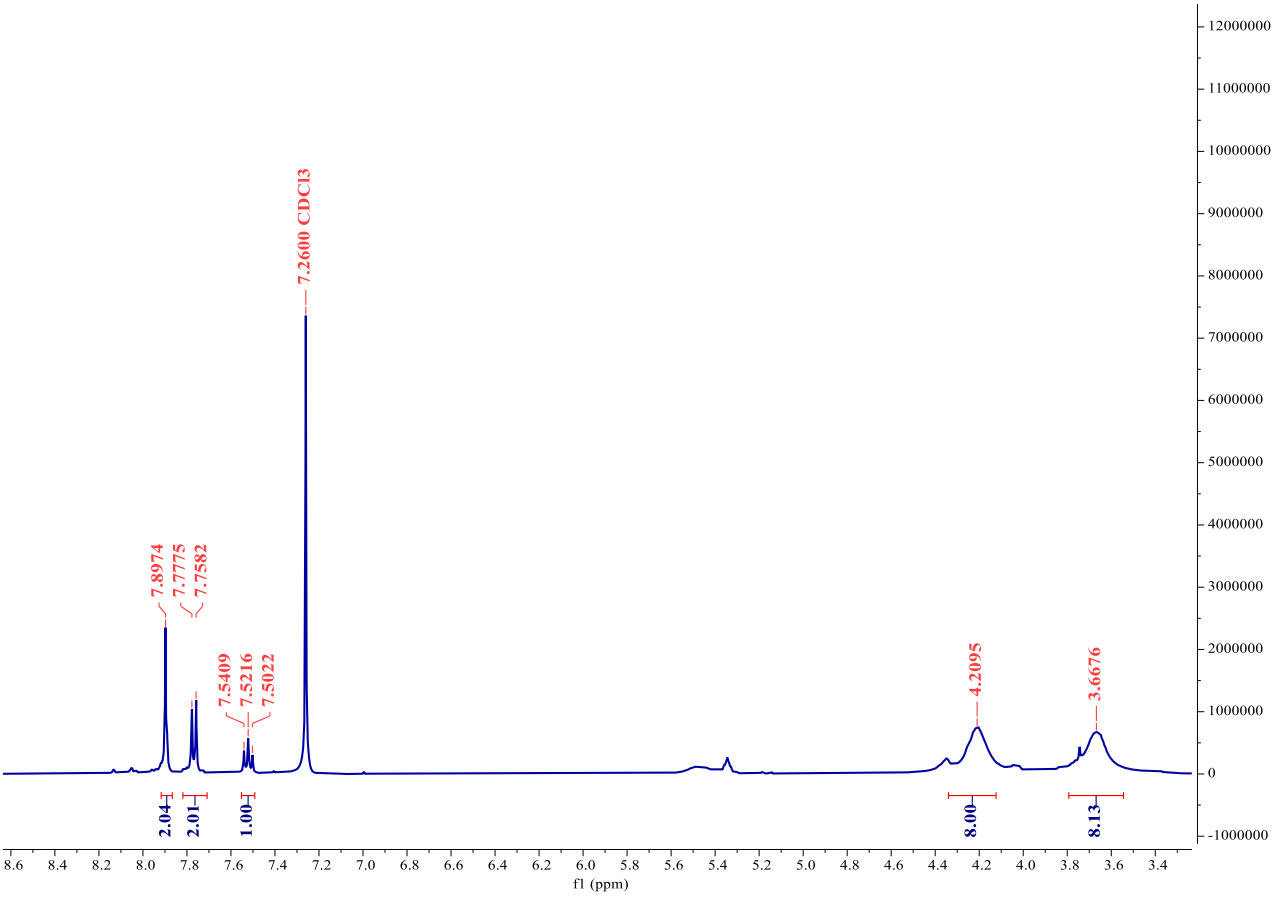

Figure A 24 *^{1}H NMR spectrum of compound* ***27*** *($CDCl_3$, 400 MHz).*

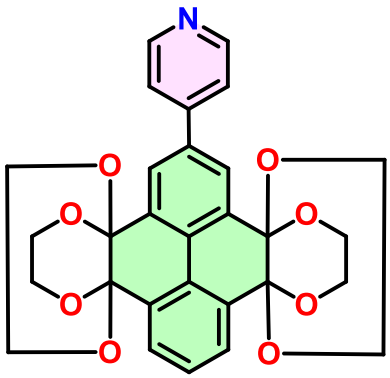

28

*Synthesis of compound **28***: A sealed tube was charged with ketal-protected compound **27** (82 mg, 120 µmol) pyridinyl-4-boronic acid (76 mg, 350 µmol) was added as a solution in THF (2 mL), followed by aqueous saturated Cs_2CO_3 solution (2 mL) under N_2 atmosphere. While stirring Xphos-Pd-G2 (3 mg, 3.6 µmol) was added followed by 0.5 ml DMF. The mixture was stirred vigorously at 85 °C for 17 h. The reaction mixture was cooled down to room temperature and was extracted with ethyl acetate (4×5 mL). The combined organic phases were dried over Na_2SO_4, and the solvents were removed under reduced pressure. PTLC was performed to isolate a suspected fluorescent band, but the NMR didn't match expected peaks. Further work needs to be done.

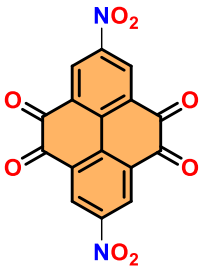

29

*Synthesis of compound **29**:* 300 mg of Pyt was dissolved in concentrated H_2SO_4 (8 ml) and to it fuming HNO_3 (2 ml) was added dropwise. The mixture was heated at 80 °C for 3 hours. The solution was then dumped into ice, and the yellow precipitate was collected by filtration, and the solid was washed with excess of water. The solid then was recollected by dispersing in MeOH and followed by evaporation of the solvent. ^{1}H NMR (600 MHz, DMSO, δ): 8.89 (s, 1H). ^{13}C NMR (151 MHz, DMSO, δ): 174.28, 148.75, 135.90, 134.11, 126.03.

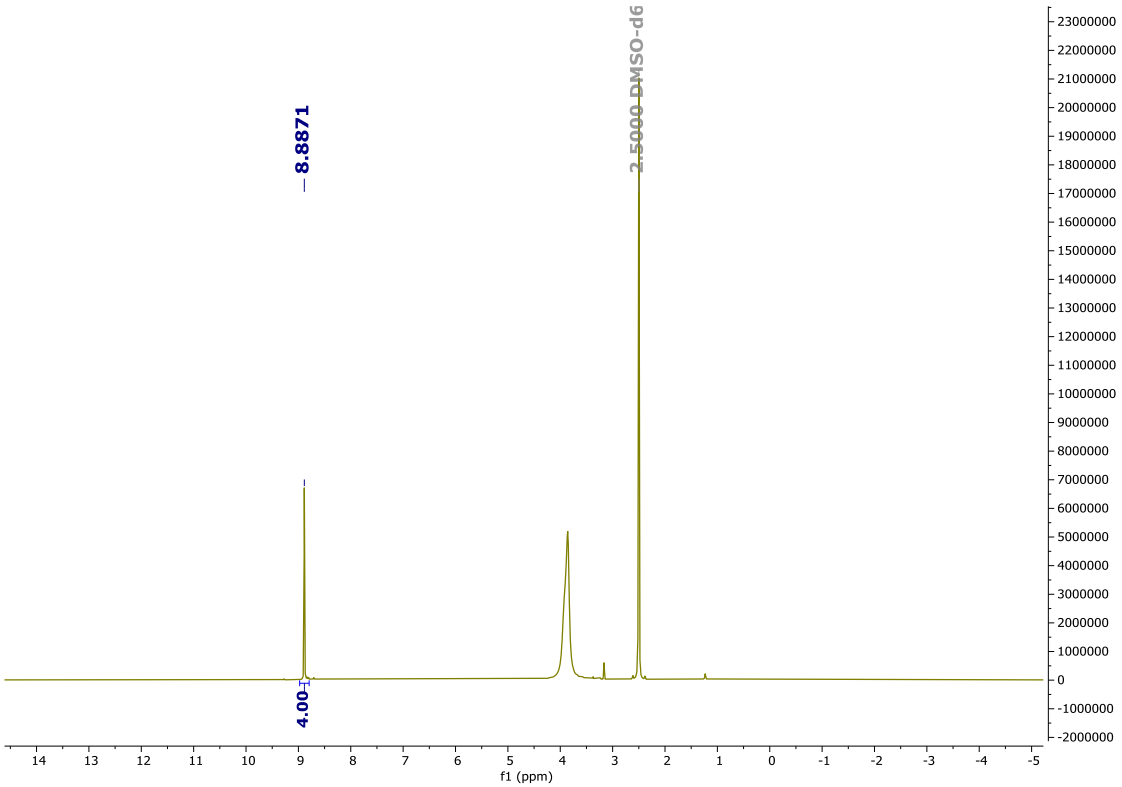

Figure A 25 *^{1}H NMR spectrum of compound **29** ($CDCl_3$, 600 MHz).*

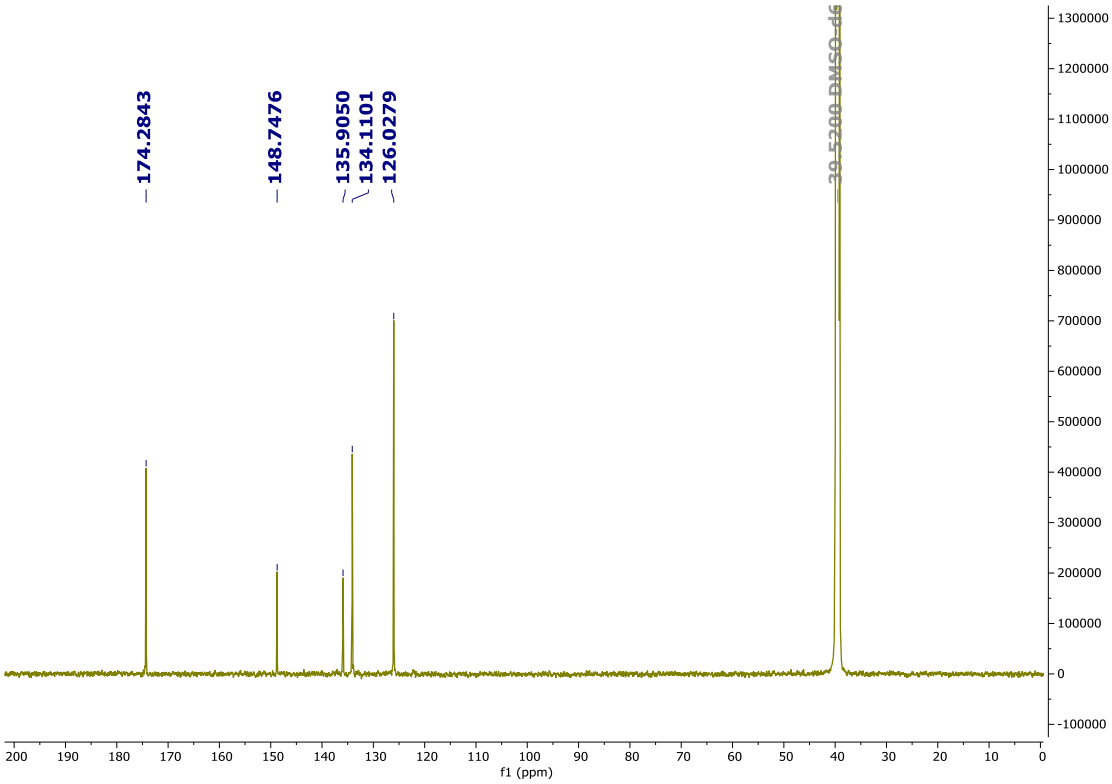

Figure A 26 *^{13}C NMR spectrum of compound **29** ($CDCl_3$, 151MHz).*

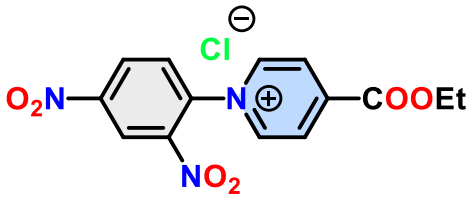

31

*Synthesis of compound **31**:* In a round bottom flask, compound **4**, 1.0 g, 4.9 mmol) and compound **30**, 746.3 mg, 4.9 mmol) were dissolved in ethanol (30 mL). The reaction mixture was refluxed for 24 hours then cooled down and solvent was evaporated under vacuum. The residual solid was recrystallized from ethanol. The solid was washed several times with diethyl ether then dried under vacuum to afford compound **3** as off white to brownish crystalline solid (780.0 mg, yield 44.8%). ^{1}H NMR (400 MHz, CD_3OD, δ): 9.54 – 9.51 (m, 2H), 9.30 (d, J = 2.5 Hz, 1H), 8.95 (dd, J = 8.6, 2.5 Hz, 1H), 8.83 – 8.79 (m, 2H), 8.34 (d, J = 8.8 Hz, 1H), 4.60 (q, J = 7.1 Hz, 2H), 1.50 (t, J = 7.1 Hz, 3H).

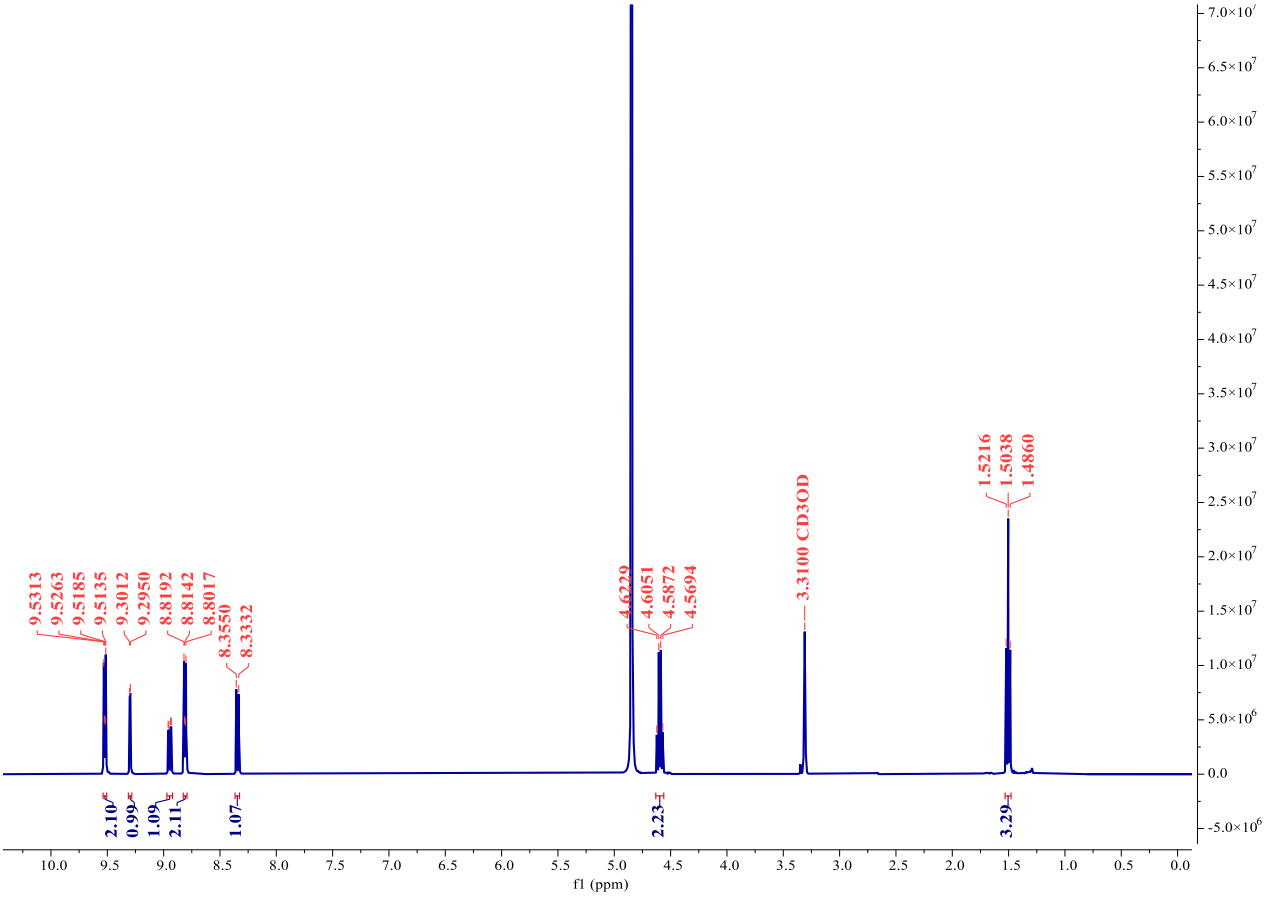

***Figure A 27** ^{1}H NMR spectrum of compound **31** (CD_3OD, 400 MHz).*

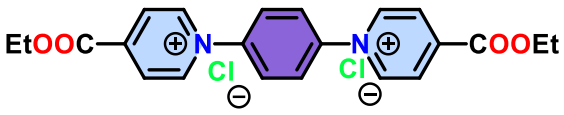

32

*Synthesis of compound **32**:* In a round bottom flask, compound **31** (503.0 mg, 1.42 mmol) and p-phenylenediamine (Compound **6**, 76.9 mg, 0.7 mmol) were dissolved in absolute ethanol (15 mL). The mixture was refluxed for 72 hours then cooled down and the solvent was evaporated under vacuum. The residual solid was recrystallized from an ethanol/acetone mixture, collected by filtration, washed several times with acetone and dried under vacuum to afford compound **5** as brownish yellow crystalline solid (350.0 mg, yield 27.5%). ^{1}H NMR (400 MHz, CD_3OD, δ): 9.59 (d, *J* = 6.9 Hz, 4H), 8.78 (d, *J* = 6.9 Hz, 4H), 8.33 (s, 4H), 4.59 (q, *J* = 7.1 Hz, 4H), 1.50 (t, *J* = 7.1 Hz, 6H); ^{13}C NMR (101 MHz, CD_3OD, δ): 162.97, 147.96, 147.79, 146.21, 128.86, 128.37, 64.84, 14.35.

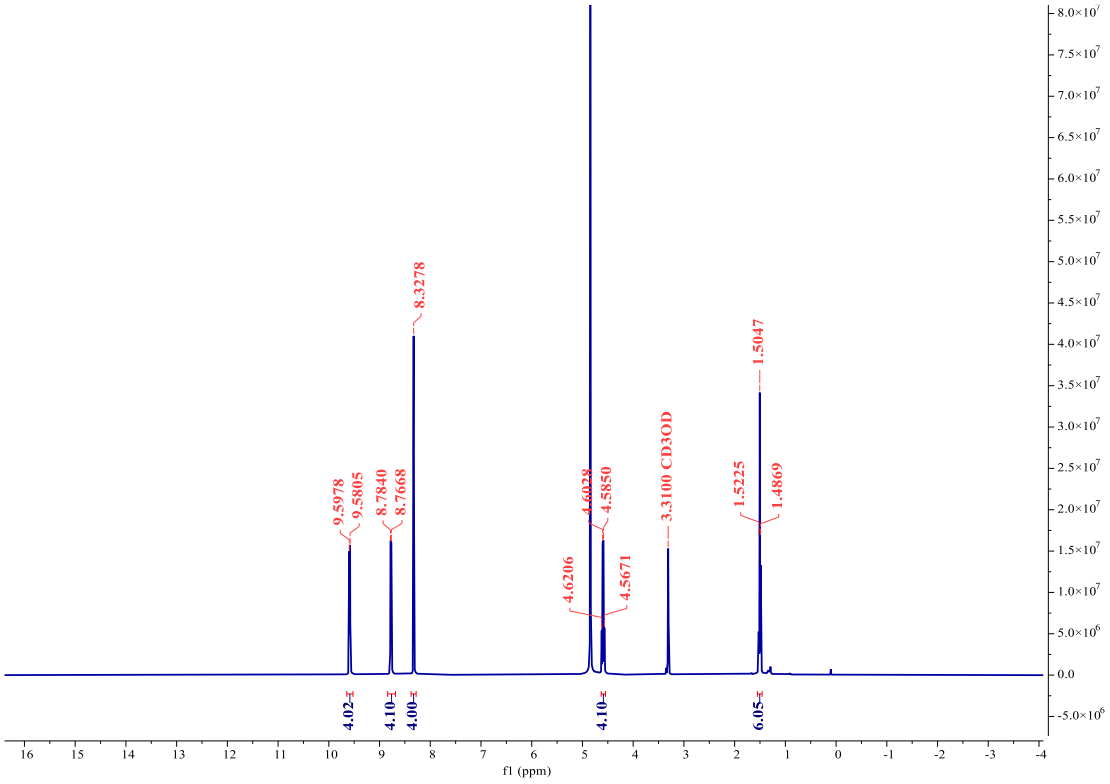

Figure A 28 *^{1}H NMR spectrum of compound **32** (CD_3OD, 400 MHz).*

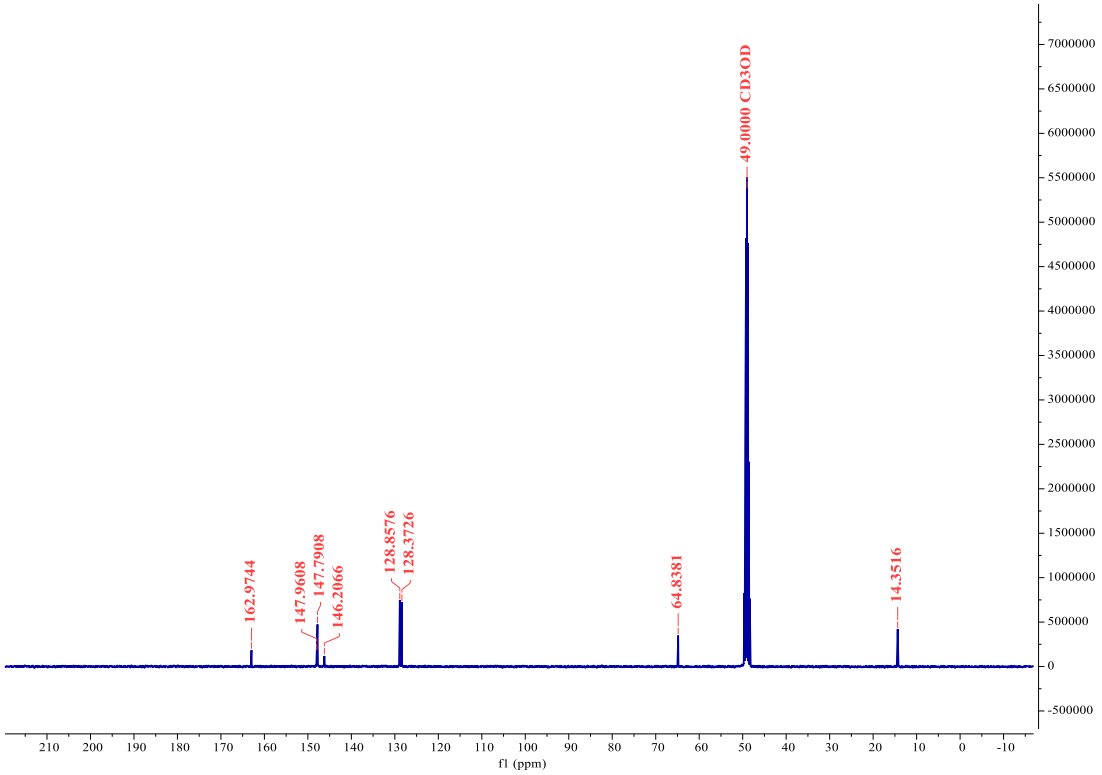

Figure A 29 *^{13}C NMR spectrum of compound **32** (CD_3OD, 101 MHz).*

*Synthesis of compound **33** and **34**:* The hydrolysis of compound **32** was performed in two ways. To yield crystals of compound 33, the hydrolysis was performed by dissolving **32** in TFA-water (1:4 volume ratio, 2.5 ml) mixture and heating the mixture for 15 hrs at 80 °C. For compound **34**, the hydrolysis was performed by dissolving **32** in HCl-water (1:4 volume ratio, 2.5 ml) mixture and heating the mixture for 15 hrs at 80 °C. The crystal structure performed by our collaborators showed the zwitter-ionic structure with interstitial water molecules for the compound **33** and the di-cationic structure with carboxylic acid groups and chloride counterions for the compound **34**.

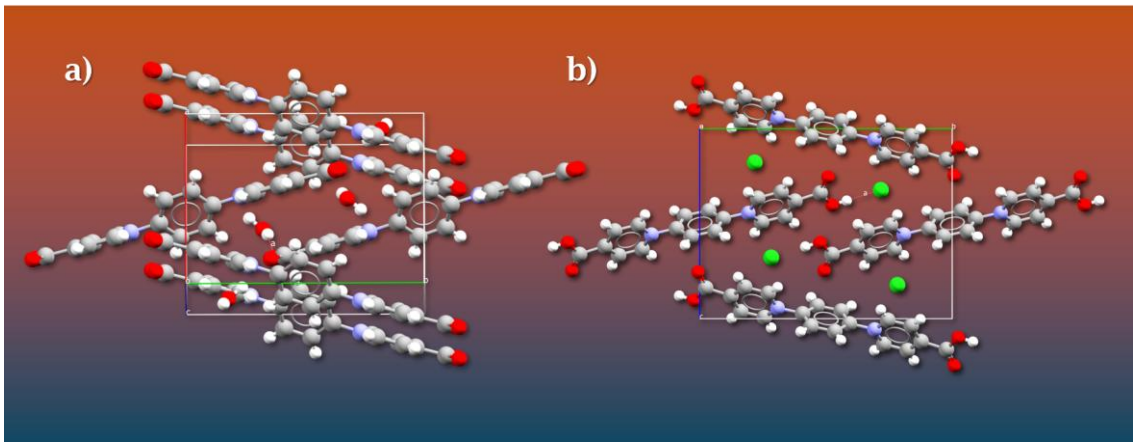

Figure A 30 *Crystal structures showing (a) zwitter-ionic form of compound **33** and (b) di-cationic compound **34** with carboxylic acid and chloride counterions.*